AD-787 466

MAGAZINE HEADWALL RESPONSE TO EXPLOSIVE BLAST

Prepared for

DEPARTMENT OF DEFENSE EXPLOSIVES SAFETY BOARD

Washington, D.C. 20314

Hsueh-Sheng Ts'ao
Damoder P. Reddy
Ross W. Dowdy

Final Report

January 1974

AGBABIAN ASSOCIATES
250 North Nash Street
El Segundo, California 90245

R-7336-3284

MAGAZINE HEADWALL RESPONSE TO EXPLOSIVE BLAST

Prepared for

DEPARTMENT OF DEFENSE EXPLOSIVES SAFETY BOARD

Washington, D.C. 20314

Hsueh-Sheng Ts'ao

Damoder P. Reddy

Ross W. Dowdy

Final Report

January 1974

AGBABIAN ASSOCIATES

250 North Nash Street

El Segundo, California 90245

R-7336-3284

MAGAZINE HEADWALL RESPONSE TO EXPLOSIVE BLAST

Final Report

Hseuh-Sheng Ts'ao
Damoder P. Reddy
Ross W. Dowdy

January 1974

Contract No. DAAB09-73-C-0019

Prepared for

DEPARTMENT OF DEFENSE EXPLOSIVES SAFETY BOARD
Washington, D. C. 20314

AGBABIAN ASSOCIATES
El Segundo, California

SUMMARY

This report presents the results of a study for predicting analytically the dynamic response of magazine headwalls subjected to blast pressure loadings resulting from the explosion of the contents of an adjacent magazine. The primary objective of the study is to simulate the headwalls in the Eskimo I test by a finite element model and to compare the results from the analytical study with the test data. A nonlinear finite element computer program, INSLAB Code, is used to compute the dynamic responses of the headwall. The behavior of the headwall material is described by a bilinear moment-curvature relationship and the supporting soil is simulated by a series of dampers. The calculations are performed for three different blast loadings. Each loading is selected on the basis of measured data and theoretical derivations. The result of the calculations are compared with available measurements. The predicted responses of the south igloo are found in good agreement with the measured data. Some disagreements between the test data and computed results are observed, especially in the north and east igloos. Recommendations are provided to improve the analytical procedure for better correlation of the results. The suggested improvements include (1) better evaluation of the material properties; (2) refinement of the finite element model; (3) alternate methods for modeling the soil; and (4) sensitivity studies of the response calculations to variations in the input parameters. It is also recommended that in future tests, pretest prediction analyses should be considered.

PREFACE

The work summarized in this report was performed for the Department of Defense Explosives Safety Board by Agbabian Associates under Contract No. DAAB09-73-C-0019 with the U. S. Army Electronics Command. The purpose of the study was to perform dynamic analyses of the response of three storage magazine headwall and door systems subjected to blast pressures resulting from the explosion of the contents of an adjacent magazine. This report covers the work performed under Task 1, definition of the blast loading; Task 2, the formulation of mathematical models, representing headwall and door structures; Task 3, modification of bilinear finite element code including the installation of damping elements; and Task 4, performing calculations of headwall and door response and comparing the computed response with measurements from the Eskimo I Magazine Separation Test.

R. W. Dowdy was the Project Manager and D. P. Reddy was the Project Engineer for the study. Major contributions to the study were made by J. W. Workman, K. P. Chuang, D. E. VanDillen, and D. G. Yates of the AA staff. The work reported was initiated on June 7, 1973 and the draft report was completed on January 31, 1974.

Acknowledgement is made to the Department of Defense Explosive Safety Board Staff, notably Mr. Beryl L. Knasel who was Contracting Officer's Representative and Mr. Russel G. Perkins, Alternate Contracting Officer's Representative, for their advice and assistance. Also Dr. T. A. Zaker, who served as technical monitor, made major technical contributions with his review and comments.

CONTENTS

CONTENTS (CONTINUED)

ILLUSTRATIONS

ILLUSTRATIONS (CONTINUED)

ILLUSTRATIONS (CONTINUED)

ILLUSTRATIONS (CONTINUED)

TABLES

SECTION 1

INTRODUCTION

This report covers a part of a general program sponsored by the Department of Defense Explosives Safety Board (DDESB) to determine safe intermagazine separation distances for various orientations of magazines storing chemical explosives. The main objective of the program is to recommend minimum intermagazine separation distances so that an explosion in one magazine (donor) will not cause an explosion in an adjacent magazine (acceptor). However, extensive damage to the acceptor magazine is considered acceptable.

Preliminary tests had indicated that specifications for minimum separation distances between magazines were excessively conservative for some orientations. Increasing land costs and siting problems made it desirable to justify reducing the front-to-rear separation distance. Earlier tests had indicated that earth-covered, steel-arch igloo magazines can be safely spaced side-to-side at a distance in feet of $1.25W^{1/3}$, in which W is the weight in pounds of the high explosives in storage. On the other hand, very little test data had been developed for determining the minimum safe distances for other magazine orientations.

In 1971, the DDESB sponsored a large-scale magazine explosion experiment called Eskimo I for the purpose of establishing minimum separation distances for face-on exposures of earth-covered, steel-arch magazines. Reference 1 includes a detailed description and the conclusions of the Eskimo I Test. Results of Eskimo I indicated that significant reduction of the formerly applicable face-to-rear and face-to-side intermagazine separation distances would be permissible.

1.1 BRIEF DESCRIPTION OF ESKIMO I TEST

Eskimo I was a large-scale magazine explosion experiment conducted on December 8, 1971, at the Randsburg Wash Test Range of the Naval Weapons Center, China Lake, California. Four earth-covered, steel-arch magazines

were exposed in the test to the explosion of the contents of a similar magazine. The donor magazine contained 200,000 pounds of high explosives. The four acceptor igloos faced the donor and were located at various distances ranging from 73 ft to 161 ft, as shown in Figure 1-1. The distances 73 ft and 161 ft correspond to $1.25\ W^{1/3}$ and $2.75\ W^{1/3}$, respectively, where W is the weight in pounds of the explosive in the donor magazine. Two concrete block structures simulating one particular type of Air Force aboveground magazine were also placed in the area at distances of 117 ft ($2\ W^{1/3}$) from the donor igloo as shown in Figure 1-1.

The four acceptor steel-arch igloos were built in accordance with the standard drawing shown in Figure 1-2. Each of the igloos was 25 ft wide by 14 ft high, with their length limited to 20 ft. Steel wing walls were used in the test in lieu of concrete. The igloos were covered by a 90 percent compacted earth surcharge to a depth of 2 ft at the top of the arch.

The damage to structures varied from minor headwall damage at the south igloo to complete destruction of the concrete block structures. The status of the acceptor charges after the test indicated a range from no explosion or burning in the south igloo to complete explosion or detonation of all charges in the east igloo.

Permanent deflections of the order of several inches, accompanied by yield-line formation, have been noted in some of the surviving headwalls. On the other hand, photographic evidence indicates that the steel plate doors in two igloos were driven in with considerable velocity before coming to rest, while remaining partially attached to frames. In the forward exposure, complete failure of the hinges occurred, and the doors were driven violently against the rear wall of that magazine (20 ft depth wall to wall).

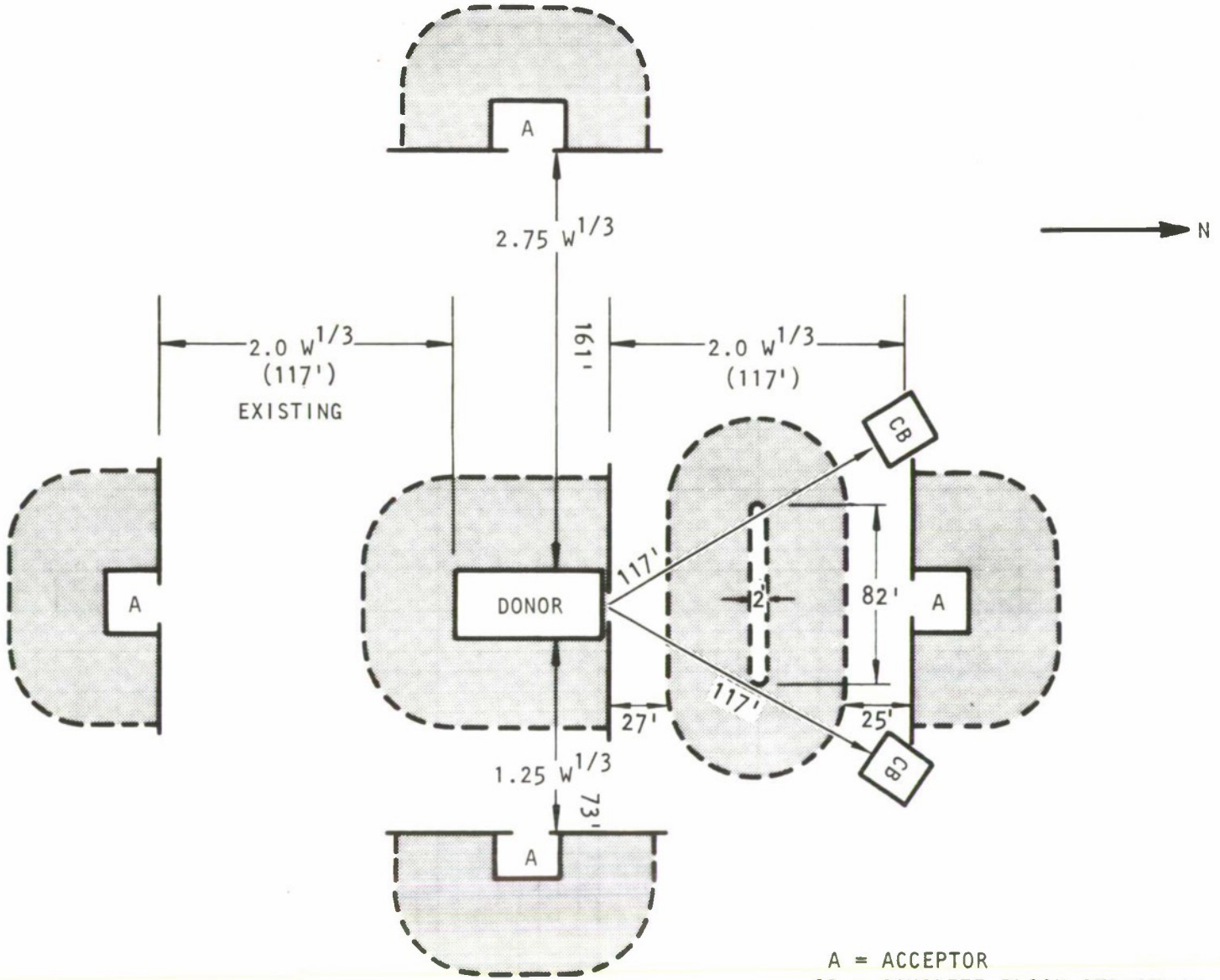

FIGURE 1-1. LAYOUT OF TEST STRUCTURES FOR ESKIMO I
DDESB IGLOO SEPARATION TEST

R-7336-3284

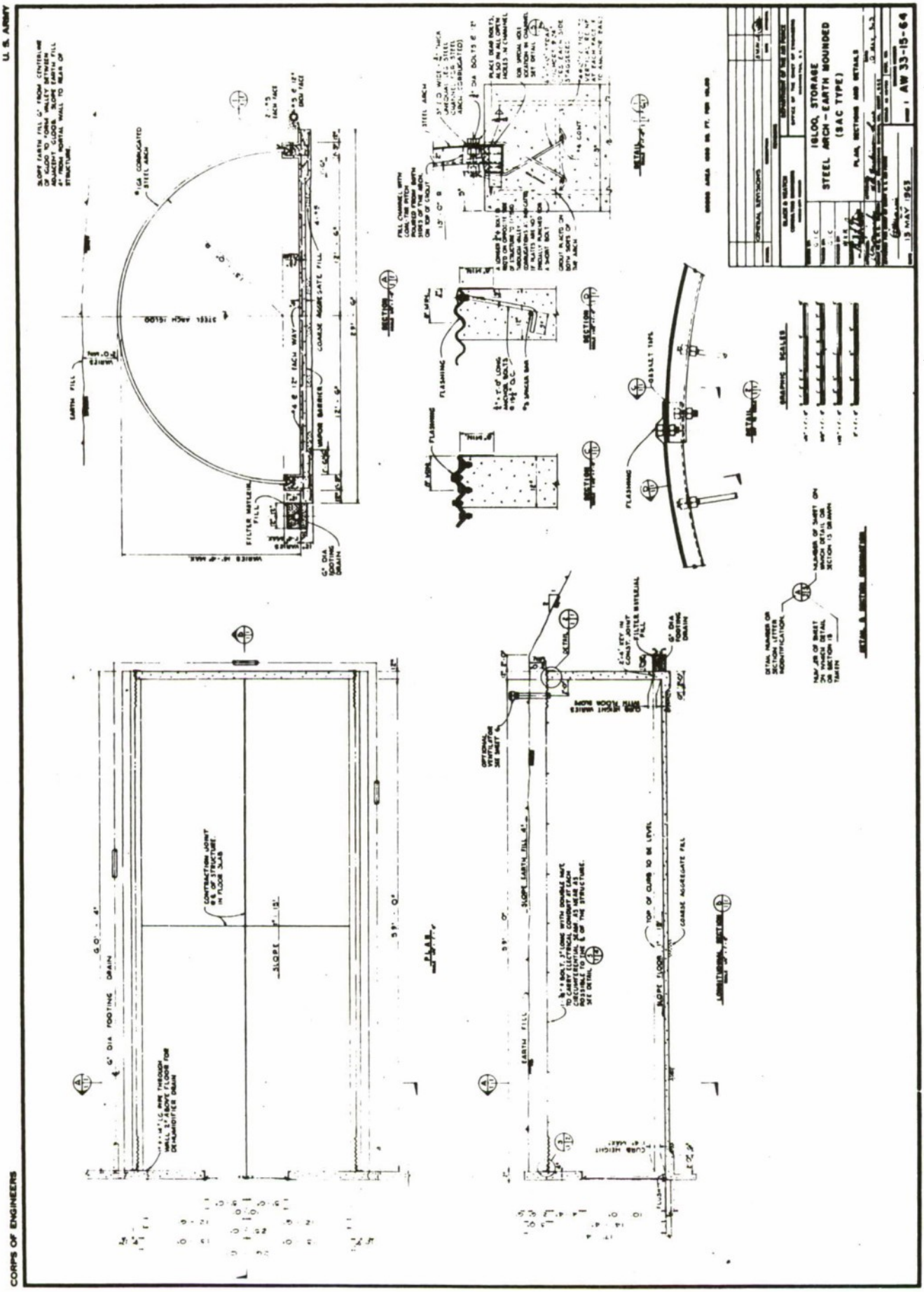

FIGURE 1-2(a). STEEL-ARCH, EARTH-MOUNDED IGLOO STORAGE MAGAZINE

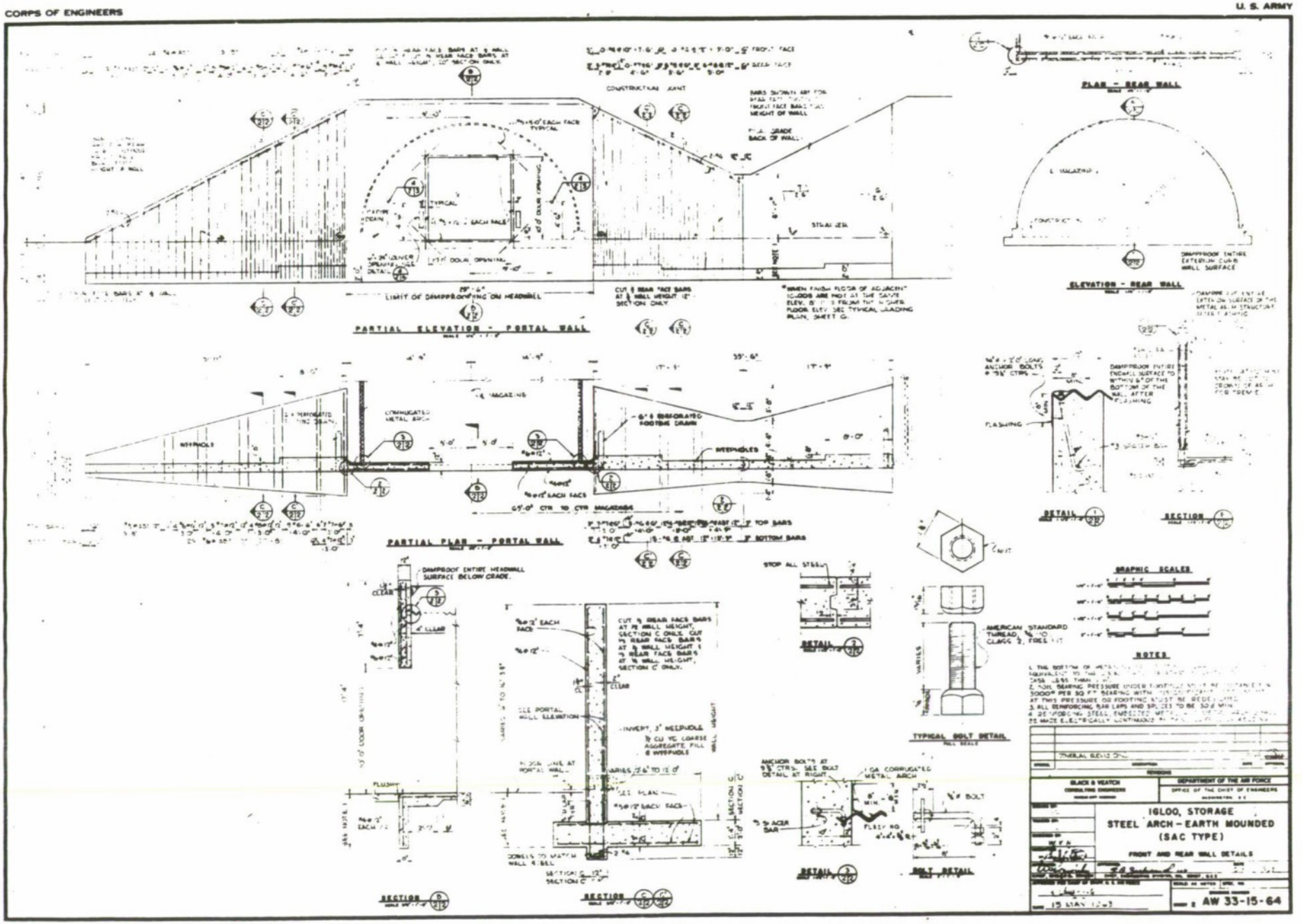
PARTIAL ELEVATION - PORTAL WALL
PARTIAL PLAN - PORTAL WALL
PLAN - REAR WALL
ELEVATION - REAR WALL
DETAIL
SECTION
TYPICAL BOLT DETAIL
BOLT DETAIL
GRAPHIC SCALES
NOTES
IGLOO, STORAGE
STEEL ARCH - EARTH MOUNDED
(SAC TYPE)
FRONT AND REAR WALL DETAILS
AW 33-15-64

FIGURE 1-2(b).

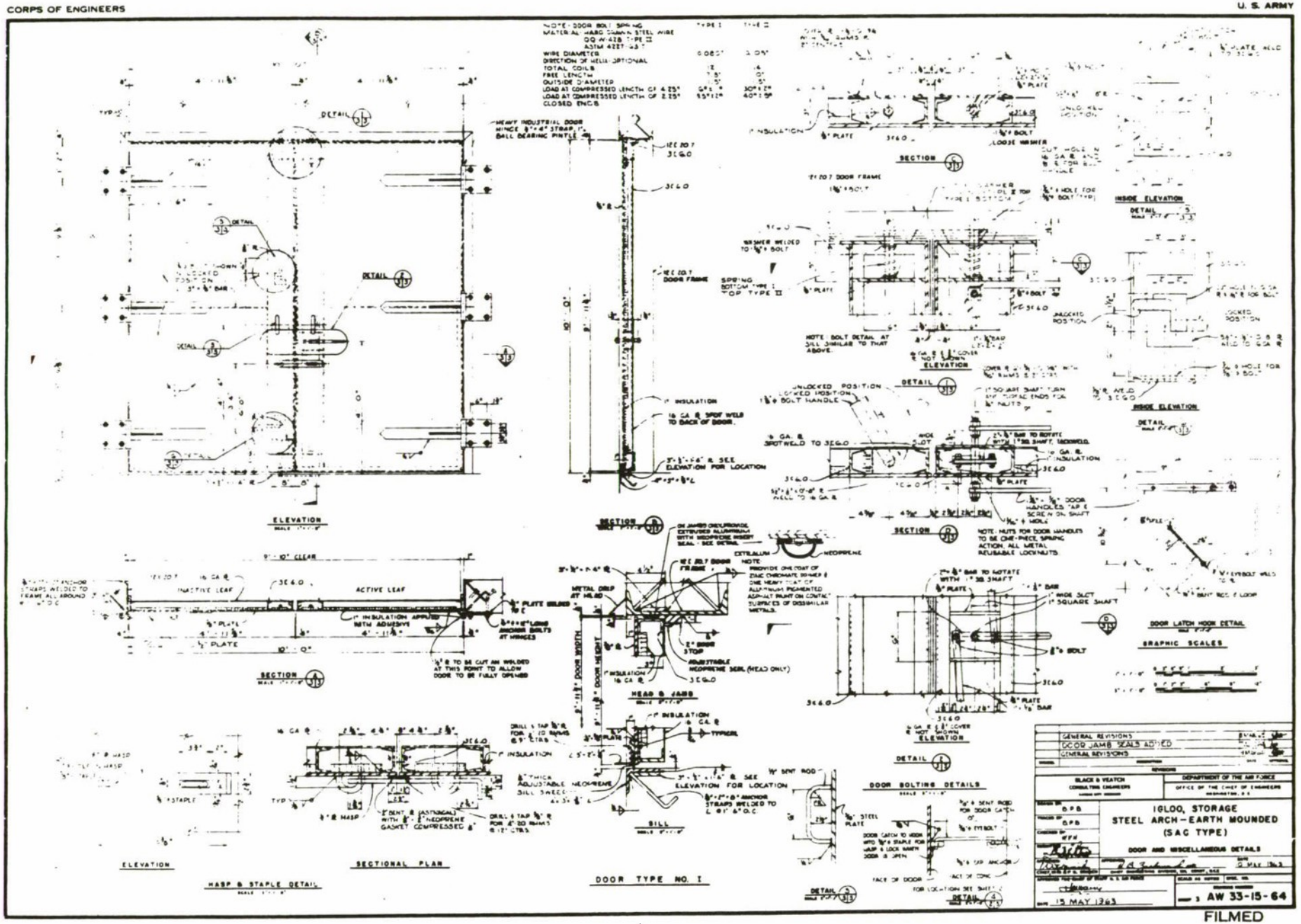
CORPS OF ENGINEERS
U. S. ARMY
DOOR TYPE NO. I
HASP & STAPLE DETAIL
SECTIONAL PLAN
ELEVATION
DOOR BOLTING DETAILS
GRAPHIC SCALES
IGLOO, STORAGE
STEEL ARCH-EARTH MOUNDED
(SAC TYPE)
DOOR AND MISCELLANEOUS DETAILS
AW 33-15-64
15 MAY 1963
FILMED

FIGURE 1-2(c).

1.2 OBJECTIVES AND SCOPE

The overall objectives of the present study were (1) to develop analytical techniques for predicting the dynamic response of concrete headwall and steel door structures to air-blast overpressures from explosion of the contents of an adjacent magazine, and (2) to compare the analytically predicted response with the experimental data available for the Eskimo I test. To achieve the objectives of the study, the following tasks are defined:

Task 1. Define blast loading on the headwalls of magazines for the mass detonation of the contents of an earth-covered donor magazine.

Task 2. Prepare a finite element model of the concrete headwall which includes a realistic representation of the steel door.

Task 3. Modify available structural analysis codes, or prepare original computer programs, to calculate dynamic response of headwall and door system to prescribed load-time histories.

Task 4. Perform calculations to obtain dynamic response of headwall and door for four full-scale exposures. Compare predicted headwall deflections and door velocities with measured responses in the Eskimo I Test.

It is noted here that no major modifications to the existing structural analysis programs were necessary for the study. Minor modifications to the SLAB and INSLAB Codes were effected for modeling the door hinges as described in Appendix C. Modifications to the INSLAB Code were also made to include viscous damping elements to model the soil behind the headwall as described in Appendix B.

BLANK

SECTION 2

BLAST PRESSURE LOADING ON MAGAZINE HEADWALLS AND DOORS

Air-blast overpressure data from the Esklmo I (Reference 1) and UK 71 Magazine Separation Tests (References 11-14) were reviewed to establish blast pressure loading historles for a series of magazine headwall and blast door response calculations. Because of the very brief presentation of Kistler gage blast pressure data from Eskimo I (Reference 1), conslderation was also given to theoretical and empirical estimates of peak blast overpressures, the influence of reflecting surfaces, and reflected overpressure pulse shapes (References 15 and 16).

Although details of the donor explosive charges used in the UK 71 test firings were quite different from those of the Eskimo I donor (cast TNT blocks versus steel artillery shells filled with TNT), blast pressure measurements from igloo headwall gages of the UK 71 tests provide a basis for establlshing pulse shapes and confirming the reflected peak pressures observed in Esklmo 1.

Since the pressure historles developed were to be used in computational simulations of the Eskimo I event, primary reliance for peak reflected pressure ampllitudes, durations, and lmpulse values was placed on the Eskimo I test data. Corrections were introduced, however, to account for differences between head-on pressures measured at the headwall and side-on reflected pressures measured 2 ft from the headwall. An abbreviated tabulation of the Klstler gage pressure data is given in Table 2-1. Data from the south igloo, whlch was lnstrumented with both head-on and side-on pressure gages, indicates an 18 percent to 25 percent difference. The recorded side-on reflected overpressures were lncreased by approximately 25 percent.

Although the observed reflection factors were consistently below those theoretlcally predicted for normally incident ideal shocks, the value recorded for the east igloo is inconsistent wlth the trend of data from the three other igloos. On the basis of data from the north igloo and from the UK 71 tests, a reflectlon factor of approximately 3 (lnstead of 1.67) should

TABLE 2-1. HEADWALL BLAST PRESSURES FOR ESKIMO I

Igloo	Measured Data				Model Pulse Data		
	$\Delta P_{incident}$ psi	$\Delta P_{reflected}$ psi	Duration msec	Impulse psi-msec	$\Delta P_{reflected}$ psi	Duration msec	Impulse[b] psi-msec
South (Rear)	33	61	26.7	545			
	33	61	28.0	693	75	29	690
		76[a]	29.7	705			530
		72[a]	27.1	641			435
West	38	68	31.5	585	75	29	690
	25	64	40.2				530
							435
North (Front)	75	238	12.5	768	300	13.5	975
							870
							635
East	150	250		1010	525	11.0	1010
							906
							708

(a) Head-on measurement on wing wall. All other values are side-on measurements from stations 2 ft in front of the headwall.

(b) The three impulse values shown are for the base-, mid-, and upper-zones of the headwall.

have been observed for an incident overpressure of 150 psi. The expected value of the side-on reflected pressure for the east igloo is 400 psi which, when increased by 25 percent, represents an expected head-on pressure of 500 psi.

The blast loading pressure histories adopted for use in the calculations are shown in Figures 2-1, 2-2, and 2-3. Since the experimentally measured blast loading conditions at the south and west igloos are nearly equal, a single model loading pulse has been adopted for these two cases. Three loading pressure histories are indicated in each figure. They represent loading histories for the three headwall zones indicated in Figure 2-4 and differ only during the unloading phase of the pressure history. The differences reflect the influence of unloading signals propagating downward from the top of the headwall. The use of just three zones was considered adequate for the finite element calculations since a relatively coarse mesh, capable of accurately describing the dynamic response over the frequency range of interest, will be used. All of the pressure histories incorporate 1-msec rise time ramp front for compatibility with the integration time step.

The blast loading pressure history developed for the south and west igloos is compared with scaled head-on blast pressure measurements from Firing 3 of the UK 71 test series (References 11-14) in Figure 2-5. The scaled data obtained from gages 2B (above the door) and 2C (beside the door) are shown in Figure 2-5(a). The exposure of Igloo 2 was similar to that of the Eskimo I west igloo, but the separation distance was somewhat smaller, i.e., $2.0\ W^{1/3}$ versus $2.75\ W^{1/3}$. As expected, the peak pressures recorded in UK 71 are higher than those in the Eskimo I test. The blast loading pulse to be used in calculations with the finite element model is compared with smoothed linearized versions of the UK 71 data in Figure 2-5(b). The general agreement in peak pressures, pulse shapes, and pulse durations is evident in both figures.

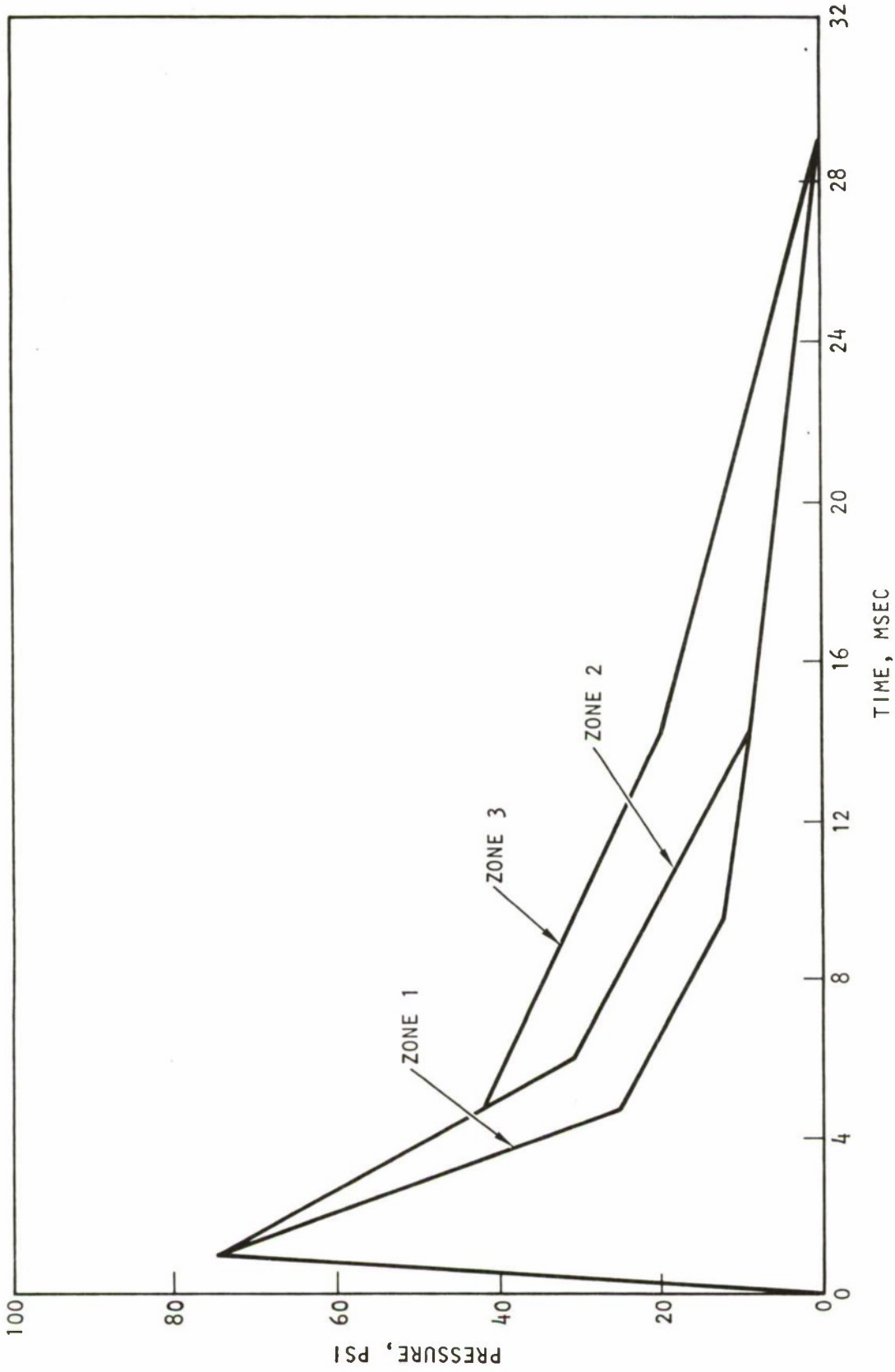

FIGURE 2-1. REFLECTED OVERPRESSURE, SOUTH AND WEST IGLOOS

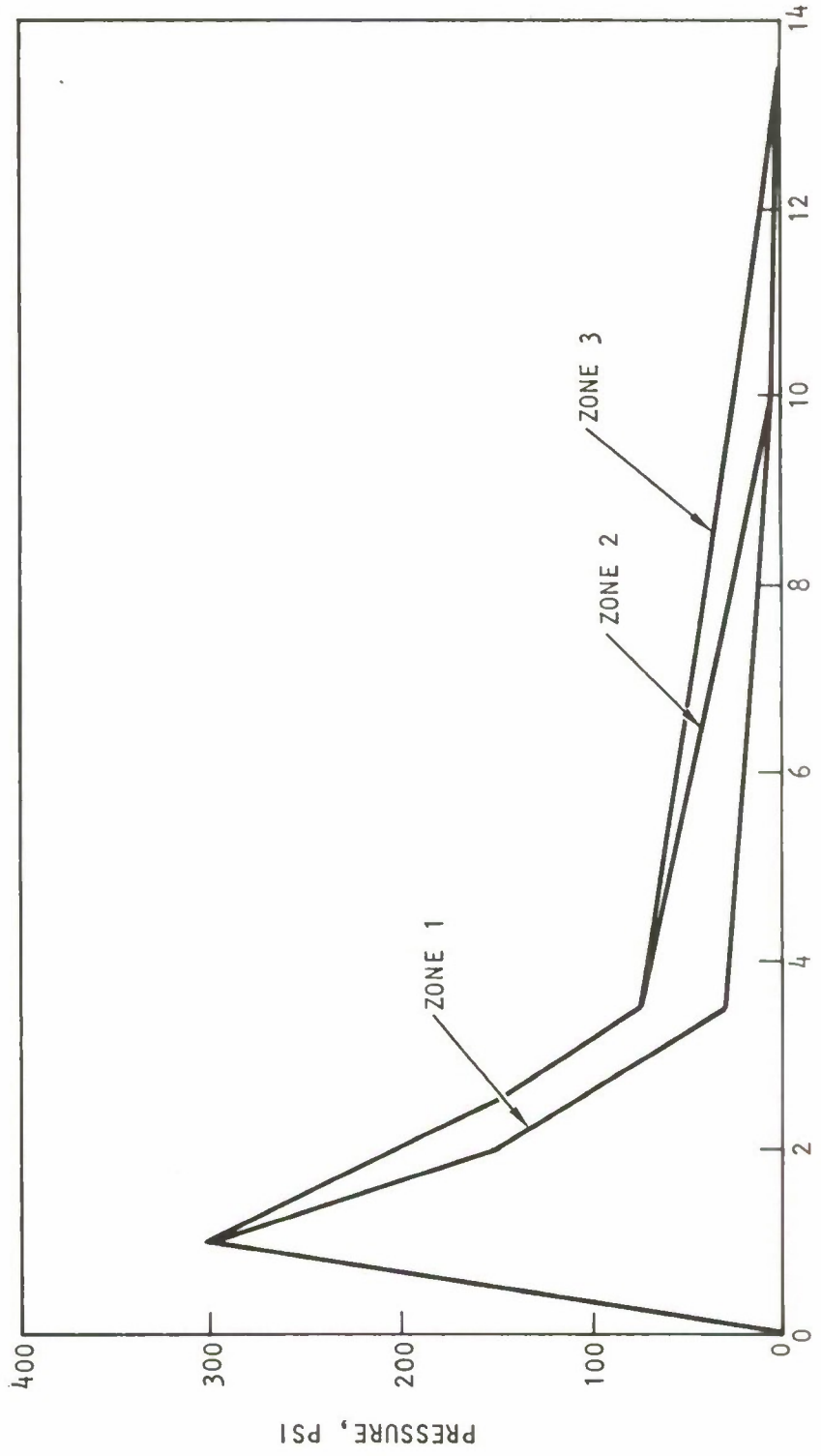

FIGURE 2-2. REFLECTED OVERPRESSURE, NORTH IGLOO

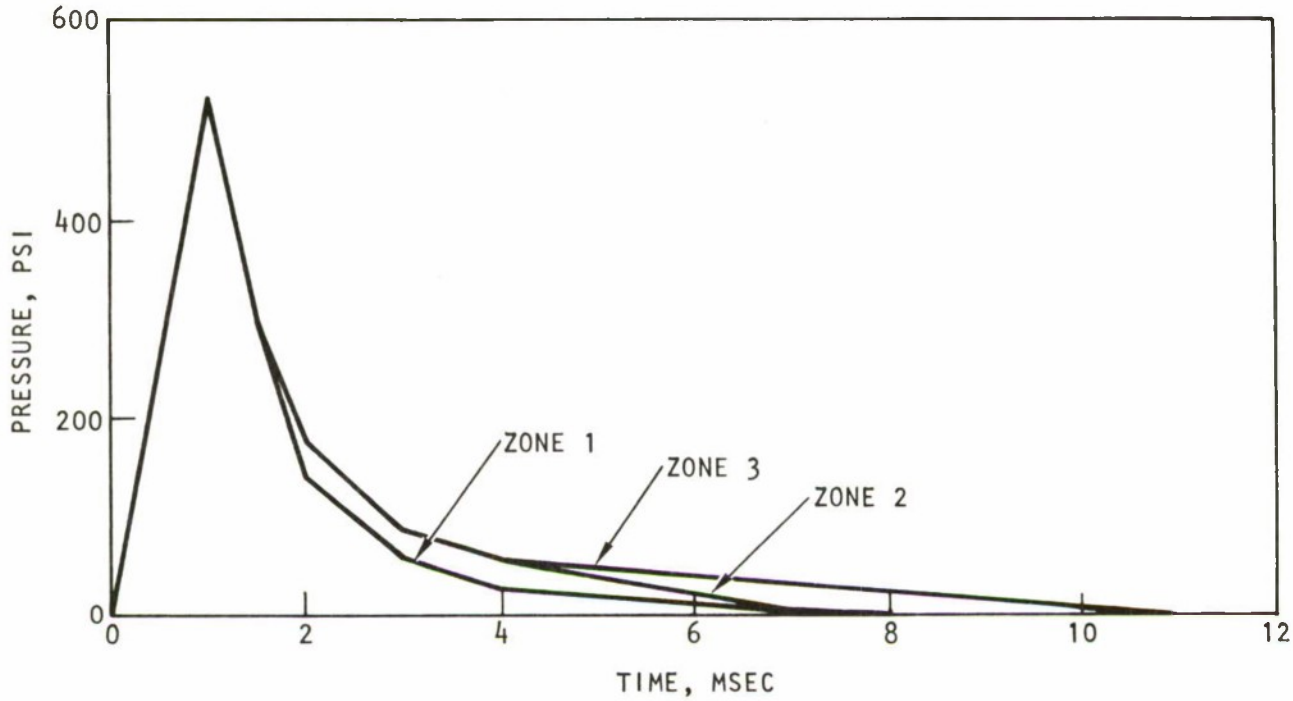

FIGURE 2-3. REFLECTED OVERPRESSURE, EAST IGLOO

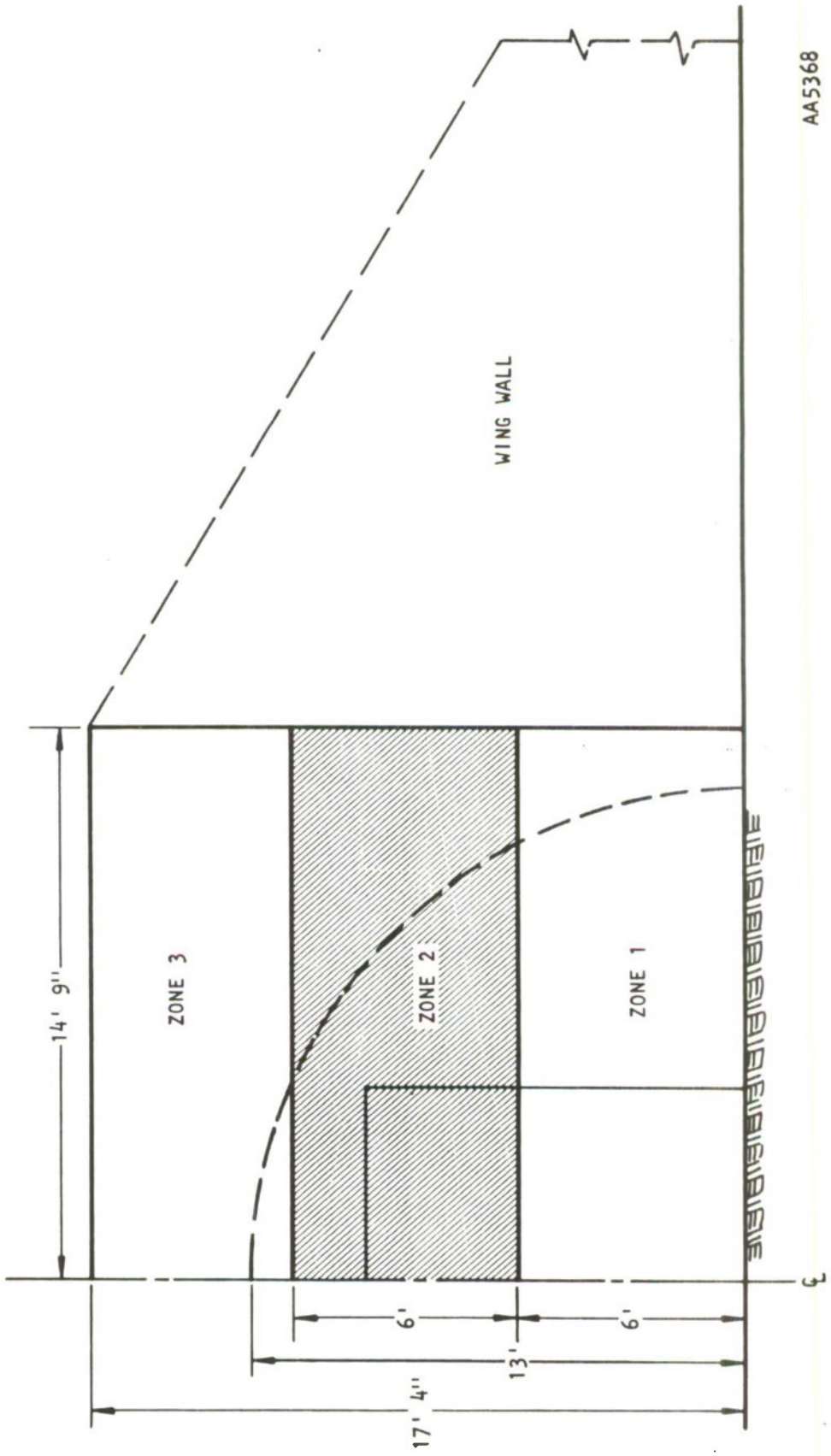

FIGURE 2-4. HEADWALL BLAST PRESSURE LOADING ZONES

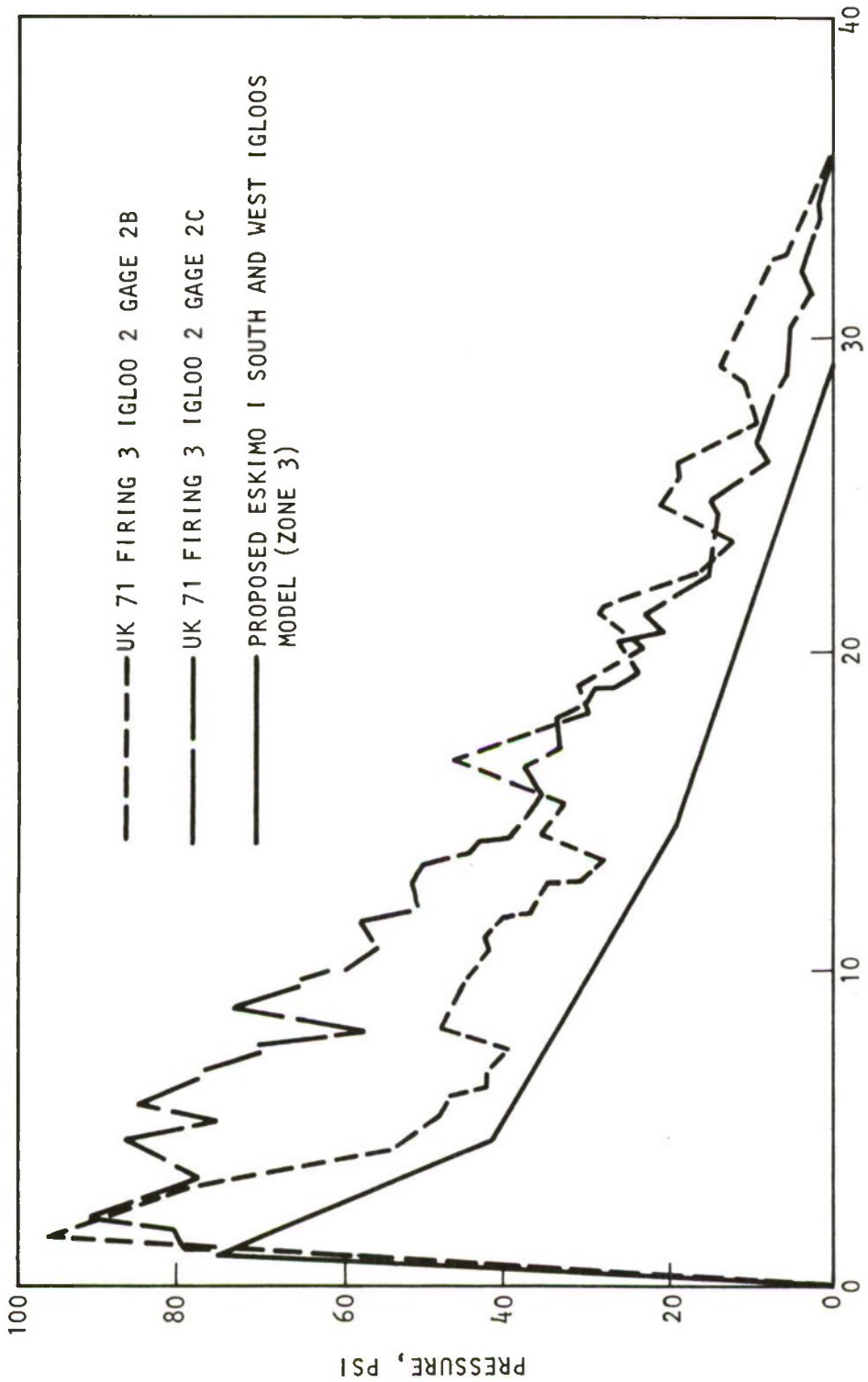

FIGURE 2-5(a). COMPARISON OF PROPOSED PRESSURE PULSE WITH UK 71 DATA

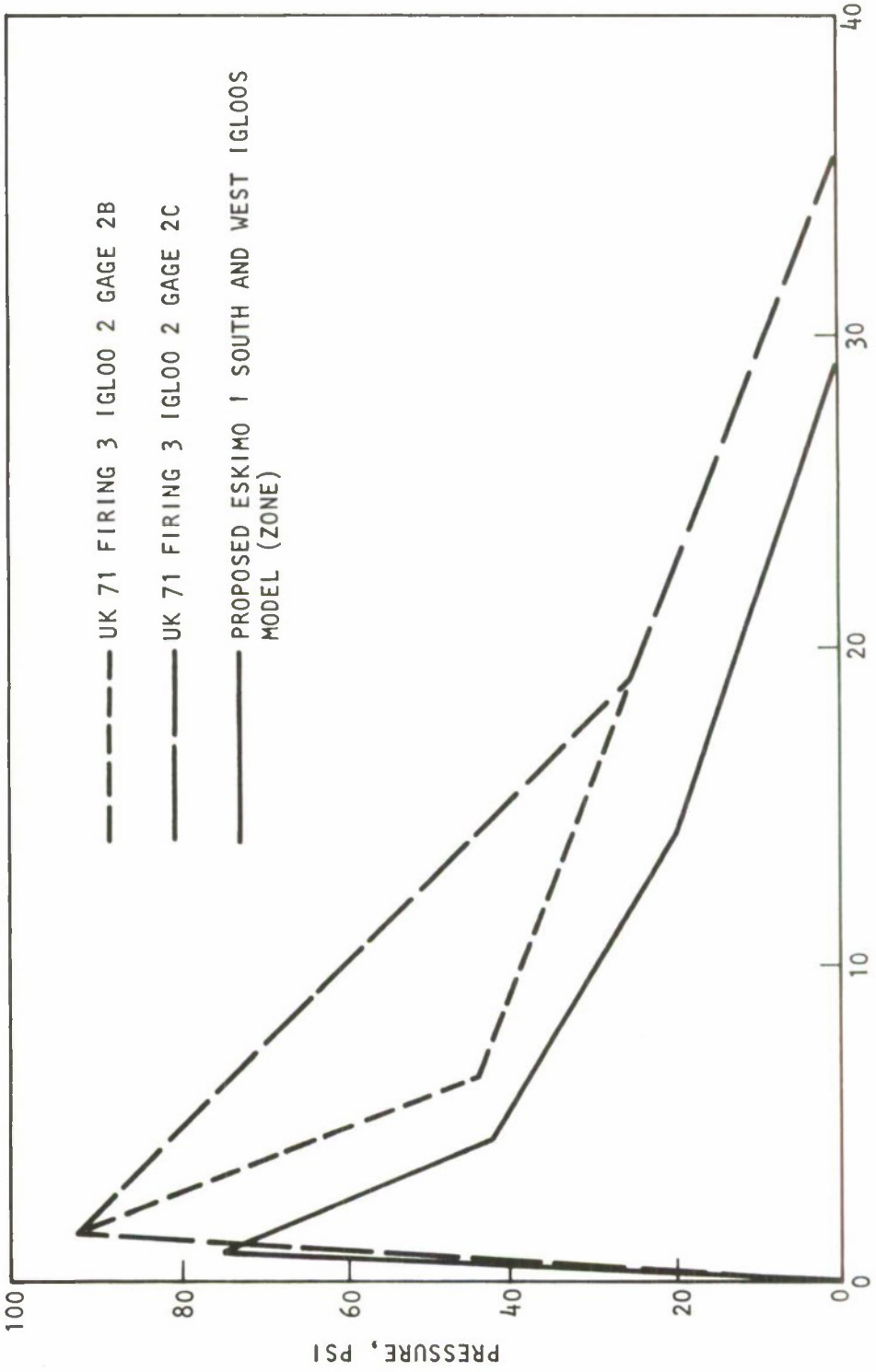

FIGURE 2-5(b). COMPARISON OF PROPOSED PRESSURE PULSE WITH SMOOTHED UK 71 DATA

BLANK

SECTION 3

STRUCTURAL MODEL

A nonlinear dynamic finite element model of the headwall and the door system is described in this section. Analysis is performed with INSLAB Code. In Section 3.1 the size of the model and the size of meshes are discussed. The material properties used in the headwall are derived in Section 3.2. The effects of soil and steel arch on the responses of the headwall and their finite element representation are discussed in Sections 3.3 and 3.4, respectively. Boundary conditions pertinent to the description of the physical conditions of the structure are presented in Section 3.5.

3.1 MODEL AND MESH SIZE DETERMINATION

3.1.1 MODEL SIZE DETERMINATION

Although the face of the magazine consists of a headwall and two wingwalls, the wingwalls are not considered in the response calculation. The effect is to neglect shear transfer from the wingwall to the headwall. The order of magnitude of the transverse shear can be approximately calculated by considering a strip of wingwall and headwall resting on the elastic foundation (represented by soil). Figure 3-1(a) shows the configuration of such a strip. The dimensions selected represent the typical sections at the mid-height of the wall. The stiffness of the soil is derived in Section 3.3.3, and a uniform pressure of 200 psi is used as an example. The resulting transverse shear is 12.1 kip/in. The effects of the shear can best be seen in Figure 3-1(b) and Figure 3-1(c). The former shows the deflection profile when the shear is not present; the latter shows the combined deflections due to transverse shear and uniform pressure.

Near the construction joint between the wingwall and headwall, the difference in deflections is significant (2.7 versus 2.0); however, a short distance away, say 2 ft, the difference is sharply reduced (1.9 versus 1.8).

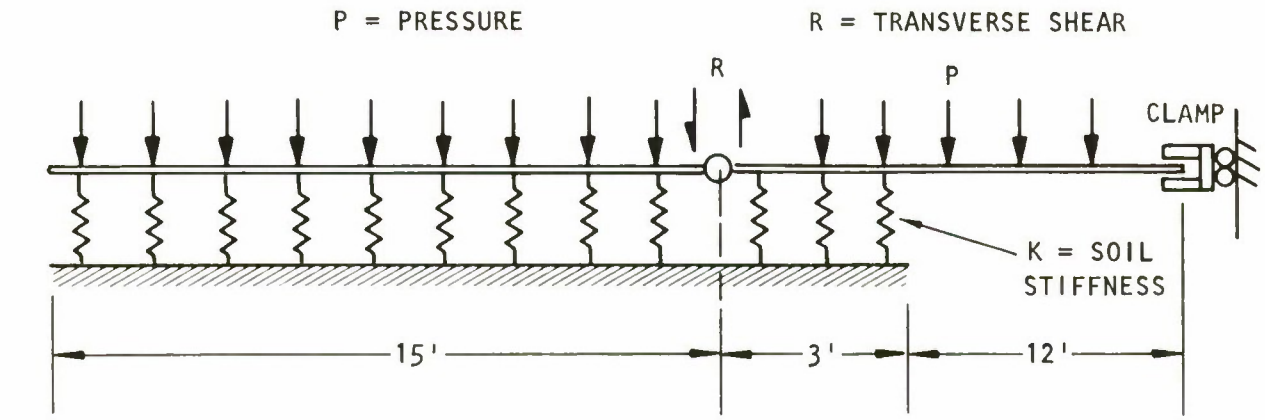

(a) A STRIP OF WINGWALL AND HEADWALL RESTING ON ELASTIC FOUNDATION

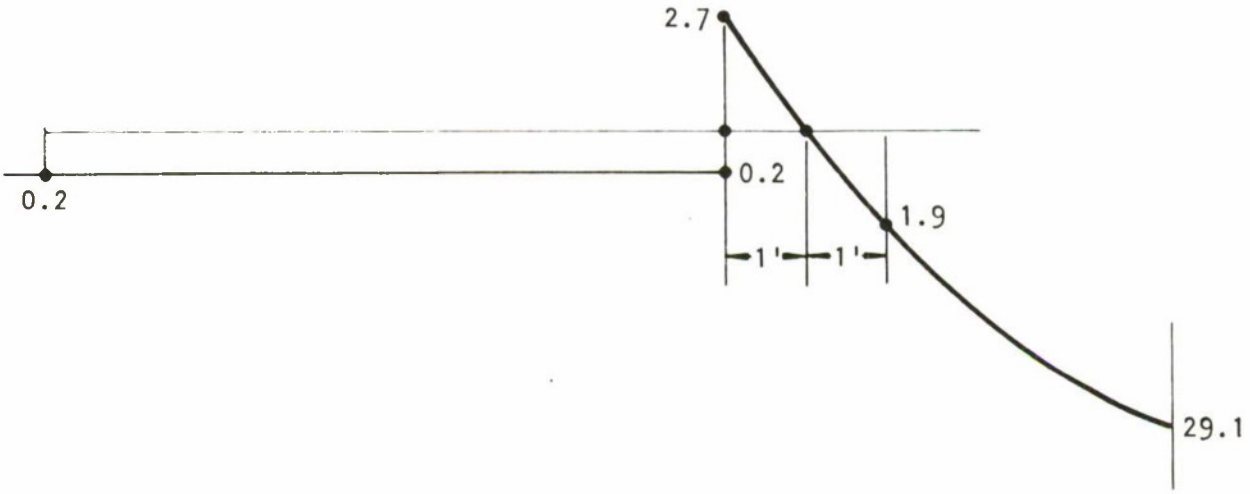

(b) DEFLECTION PROFILE WITHOUT TRANSVERSE SHEAR (IN INCHES)

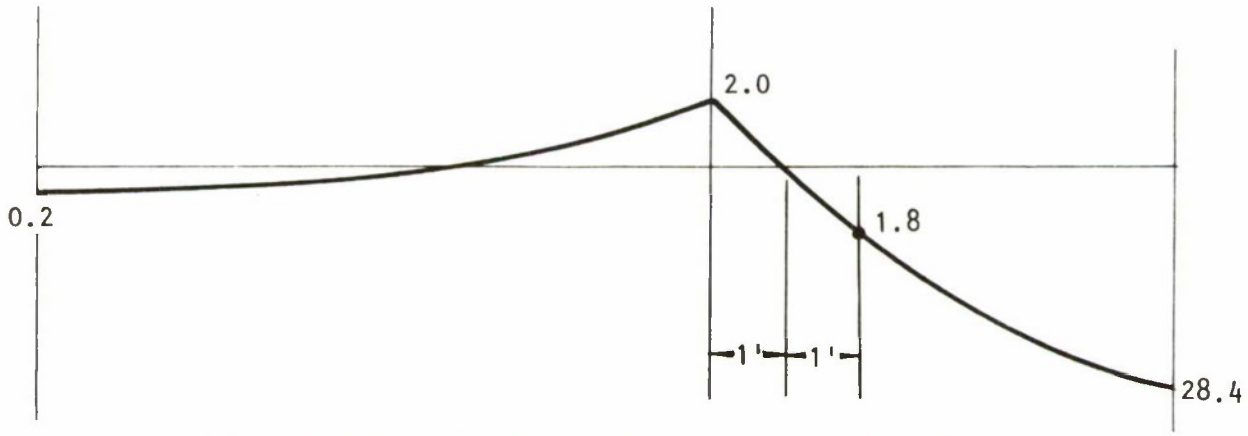

(c) DEFLECTION PROFILE WITH TRANSVERSE SHEAR (IN INCHES)

FIGURE 3-1. EFFECT OF WINGWALL ON HEADWALL DEFLECTIONS

From that point on to the center of the headwall, the effects of transverse shear become very small, and the overall headwall responses without the consideration of the wingwall are justified.

3.1.2 MESH SIZE DETERMINATION

Ideally, the mesh size (dimensions of individual element) is made as small as possible so that the resulting finite element model can properly represent the continuum of the headwall. In actual practice, the mesh size is made as large as the problem allows so that the computer-run time and the core storage can be efficiently used. The limitation of the mesh size is determined by the frequency range to be considered, which in turn is determined by the frequency content of the input. Inspection of the input loading histories described in Section 2 indicates that the histories contain higher frequencies only in the initial 3-msec duration. If the rise time of 1 msec is used as the estimate of the highest frequency that may have significant contribution to the headwall responses, the mesh size should be selected so that the individual elements exhibit frequencies up to 1000 Hz (equivalent to a period of 1 msec). Since the main portion of the headwall consists of plate elements, several sizes of plate elements are investigated, and their frequencies are estimated utilizing the tables prepared by Leissa (Reference 17). Two frequencies are calculated for each plate element based on two different boundary conditions: fixed, and simply supported conditions. The actual frequency of a typical mesh lies between these two calculated values. It is found that the maximum size of an individual finite plate element representing the headwall is about 3 ft by 3 ft. The corresponding frequencies are approximately 900 Hz for simply supported and 1660 Hz for fixed end conditions. The use of coarser mesh may still be within the desired frequency range but may not reveal enough detailed variation in responses of the headwall. The final mesh configuration is shown in Figure 3-2. The mesh consists of 66 nodes and 51 quadrilateral plate elements. An effort is made to avoid the use of any triangular plate elements as they are not, in general, as accurate as quadrilateral elements. The half bandwidth of the stiffness matrix associated with the final mesh is 33.

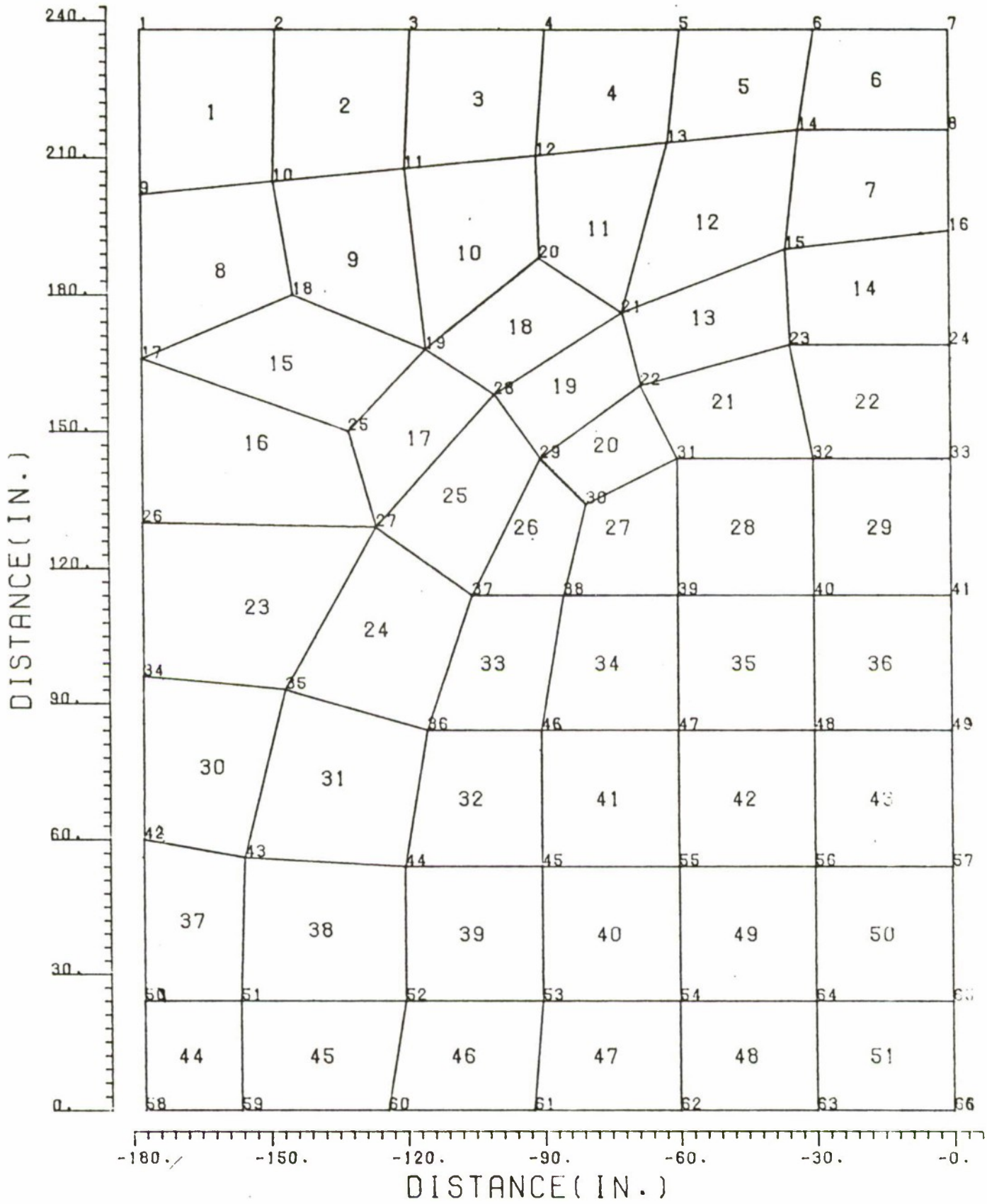

FIGURE 3-2. FINITE ELEMENT MODEL OF THE MAGAZINE HEADWALL

3.2 MATERIAL PROPERTIES

3.2.1 MATERIAL PROPERTIES OF THE DOOR

The material used in the door is steel. The main structural components consist of a 3/8-in. plate; 3-in. channels welded along the door edges; 3-in. x 3/8-in. plate stiffeners; and a No. 16-gage steel plate, spot-welded to the back of the door. Details of the door construction are shown in Figure 3-3.

The pertinent information regarding the material and geometrical properties of the door is listed below:

$E = 30 \times 10^6$ psi , Young's modulus of elasticity

$\nu = 0.25$, Poisson ratio

$I_x = 0.793$ in.^{4}/in. , Average moment of inertia about x-axis of a cross section normal to y-axis

$I_y = 0.682$ in.^{4}/in. , Average moment of inertia about y-axis of a cross section normal to x-axis

$W = 1210$ lb , Weight of the door

$$D_y = \frac{EI_y}{(1 - \nu^2)} = 21.8 \times 10^6 \text{ lb-in.,} \quad \text{Flexural rigidity}$$

$$D_x = \frac{EI_x}{(1 - \nu^2)} = 25.4 \times 10^6 \text{ lb-in.,} \quad \text{Flexural rigidity}$$

In the finite element representation, the door is modeled as a plate of uniform thickness possessing the major characteristics of the real door. These characteristics and their relation to the modified material and geometric properties are discussed below.

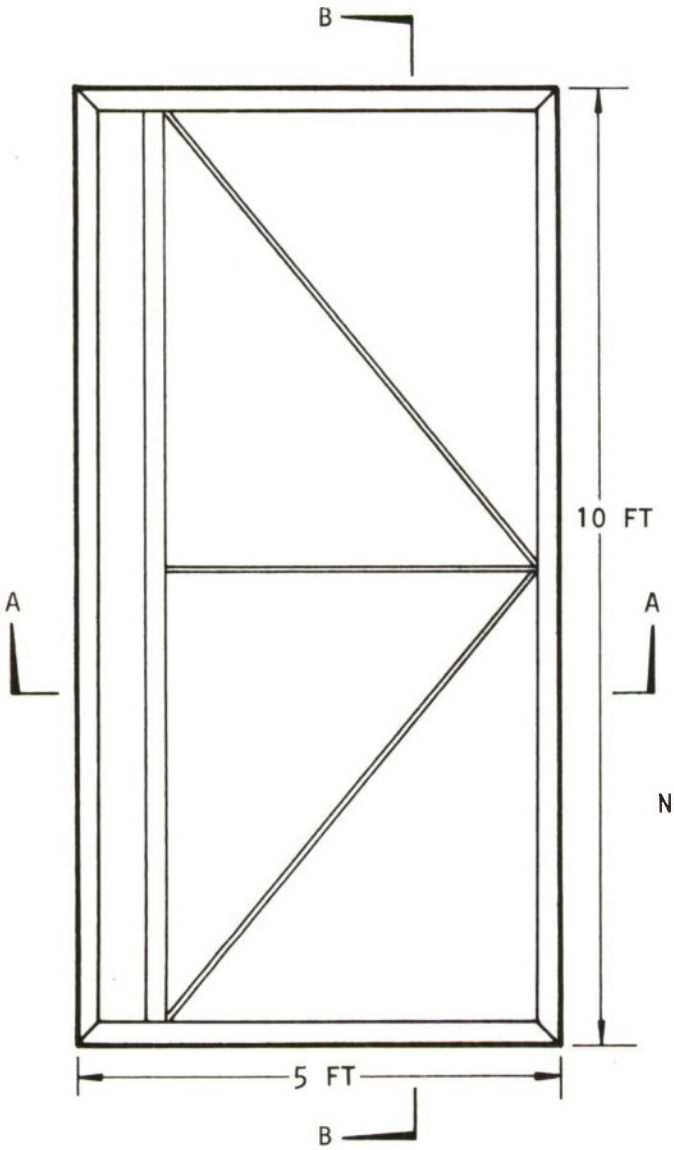

(a) ELEVATION OF THE DOOR

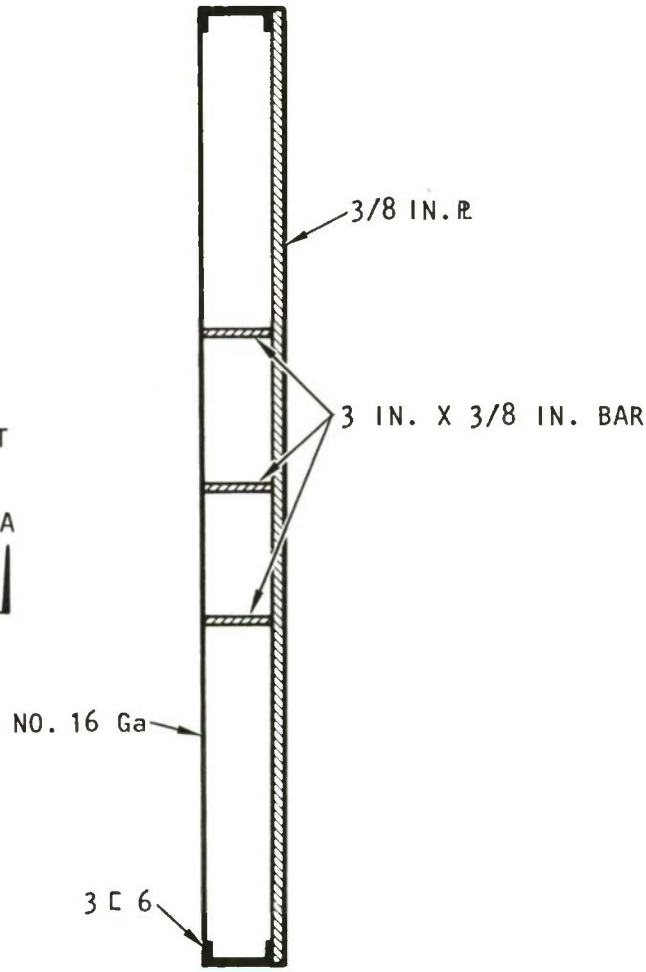

(c) CROSS SECTION B-B ALONG Y-AXIS

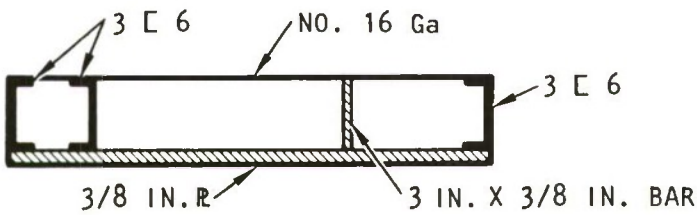

(b) CROSS SECTION A-A ALONG X-AXIS

FIGURE 3-3. STEEL DOOR CONFIGURATION

a. In order to have a plate of uniform thickness and to have moments of inertia as close as possible to I_x and I_y, the geometrical mean of the door thickness is used, i.e.,

$$\frac{h^3}{12} = \sqrt{I_x I_y} \quad \text{or} \quad h = 2.04 \text{ in.}$$

b. Since the flexural rigidity is directly proportional to the response displacements and moments, the moduli of elasticity E_x and E_y and the thickness h to be used in the model should be such that the calculated flexural rigidity is equal to the actual flexural rigidity, i.e.,

$$D_x = \frac{E_x h^3}{12(1 - \nu^2)}, \qquad E_x = 32.4 \times 10^6 \text{ psi} = 1.08 E$$

$$D_y = \frac{E_y h^3}{12(1 - \nu^2)}, \qquad E_y = 27.8 \times 10^6 \text{ psi} = 0.93 E$$

c. The thickness of the door model selected in *a* changes the total weight of the steel door. Therefore, the density is modified such that the total weights of the model and the physical door are equal.

$$\tau = \frac{W}{Ah} = 0.0812 \text{ lb/in.}^3$$

d. The moment required for the door material to reach yield point is calculated by the formula

$$M = \frac{f_y I}{C}$$

where f_y is the yield stress of steel. In the present study, the duration of the input loading is very short; therefore, a dynamic yield stress is more appropriate than the static yield stress value. According to Reference 18, the time for a structure to reach yield, due to blast loading, ranges from 0.1 to 0.01 sec. The average value of the dynamic yield stress for this range is 41.6 ksi against a value of 36 ksi for the static yield stress. The resulting yield moments based on the configurations of Figure 3-3 and the above-mentioned formula are:

$$M_{xx} = \pm 10.25 \text{ kip-in./in., based on } c=2.79 \text{ in. and } \bar{I}_y = .682 \text{ in.}^4/\text{in.}$$

$$M_{yy} = \pm 11.10 \text{ kip-in./in., based on } c=3.01 \text{ in. and } \bar{I}_x = .793 \text{ in.}^4/\text{in.}$$

where the sign conventions for the moments M_{xx} and M_{yy} are as given in Appendix A.

e. After yielding, the plastic modulus E_p takes the place of elastic modulus E_e, and a ratio of $E_p/E_e = 0.1$ is used in the study.

3.2.2 MATERIAL PROPERTIES OF THE REINFORCED CONCRETE

The concrete section of the magazine headwall is shown in Figure 3-4. The reinforcement is assumed to have Young's modulus, E, of 30×10^6 psi. Due to the rapid application of loading, the dynamic yield stress, f_y, for steel is taken as 52 ksi, as suggested in Reference 3.

The modulus of elasticity for concrete, E_c, is assumed to be 3×10^6 psi, and the yield stress, f'_c, is taken as 3900 psi, where the effect of rapid loading is assumed to be a 30-percent increase from static yield strength of 3000 psi.

Based on Figure 3-4 and the assumed material properties of reinforced concrete, the yield moments for both cross sections S_x and S_y are calculated. It is found that both cross sections are underreinforced; therefore, the yield moments are governed by the tensile strength of steel.

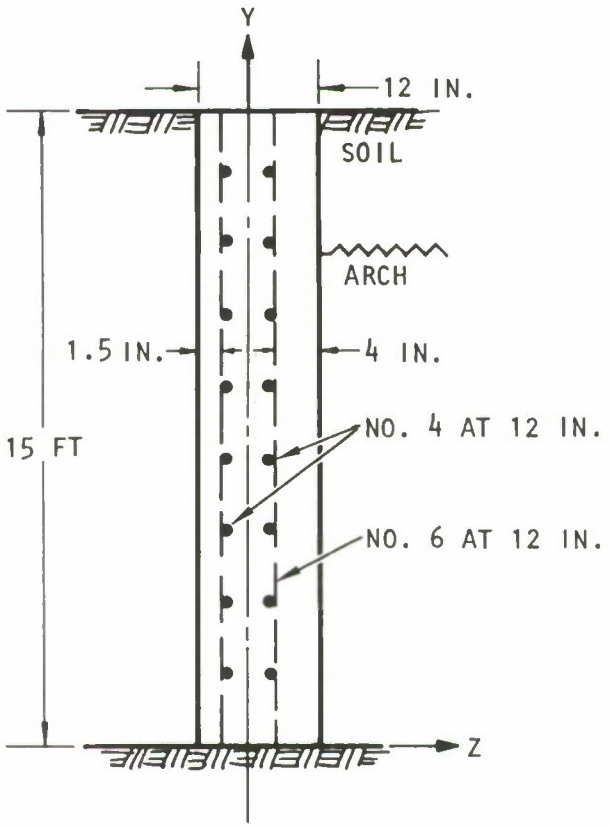

(a) REINFORCED CONCRETE SECTION

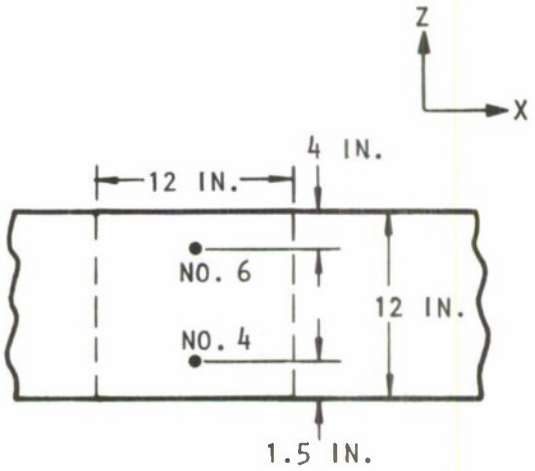

(b) CROSS SECTION S_Y PERPENDICULAR TO Y-AXIS

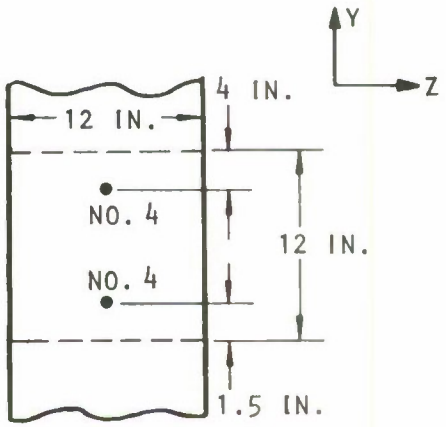

(c) CROSS SECTION S_X PERPENDICULAR TO X-AXIS

FIGURE 3-4. DETAILS OF HEADWALL CONSTRUCTION (NOT TO SCALE)

For Section S_x

M^+_{yy} = 77.5 kip-in./ft when the headwall concaves inward

M^-_{yy} = 101 kip-in./ft when the headwall concaves outward

For Section S_y

M^+_{xx} = 169 kip-in./ft when the headwall concaves inward

M^-_{xx} = 101 kip-in./ft when the headwall concaves outward

3.3 EFFECTS OF SOIL

The compacted soil covering the steel arch interacts with the headwall several ways. It provides resistance for the headwall under blast loading. Part of its mass tends to move with the headwall, thereby creating additional inertia forces to oppose the loading. In addition, the soil pressure imparts initial moments (and stresses) on the steel arch and the headwall. All these factors are discussed in this section.

3.3.1 INITIAL MOMENT ON THE HEADWALL

The resisting pressure of the soil on the headwall is expressed as a fraction of the hydrostatic pressure, i.e.,

$$p = c\tau h$$

where

τ is the weight density of the soil

h is the depth

c is a coefficient whose value depends on the type of soil and the percentage of compaction, etc. For compacted sandy soil used in this study

$$c = 0.8 \text{ (Reference 19)}$$

If the headwall is assumed to act like a cantilever plate, the bending moment at depth h is given by

$$M = \frac{c\tau h^3}{6}$$

At midheight of the headwall, h = 7.5 ft. This gives M = 6.96 kip-in./ft.

At the lower portion of the headwall, the cantilever assumption is not valid because the constraints from the steel arch and the construction joint connected to the wingwall at the two sides of the headwall make it act more like a plate fixed at three sides. If a plate fixed at three edges (Figure 3-5(b)) is assumed to replace the actual plate configuration (Figure 3-5(a)), the maximum bending moment subjected to the soil pressure is found at Point A.

$$M_A = -0.0775\ \tau h^3 = 4.04 \text{ kip-in./ft}$$

The yield moment calculated in the previous section (Section 3.2) shows that the initial moments on the headwall are less than 10 percent of the yield moment; therefore, ignoring the initial moments on the headwall will not significantly change the outcome of this study.

3.3.2 INITIAL MOMENT ON THE STEEL ARCH

As a crude estimate of the moments created by the presence of soil on the steel arch, the steel arch is treated as a thin cylindrical shell subjected to uniform pressure normal to the shell surface. Theoretical solutions for this type of problem can be found in Reference 20. The maximum bending moment is located at the connection between the arch and the headwall, which is assumed fixed.

$$M = -1/2\ \frac{pRt}{\sqrt{1 - \nu^2}}$$

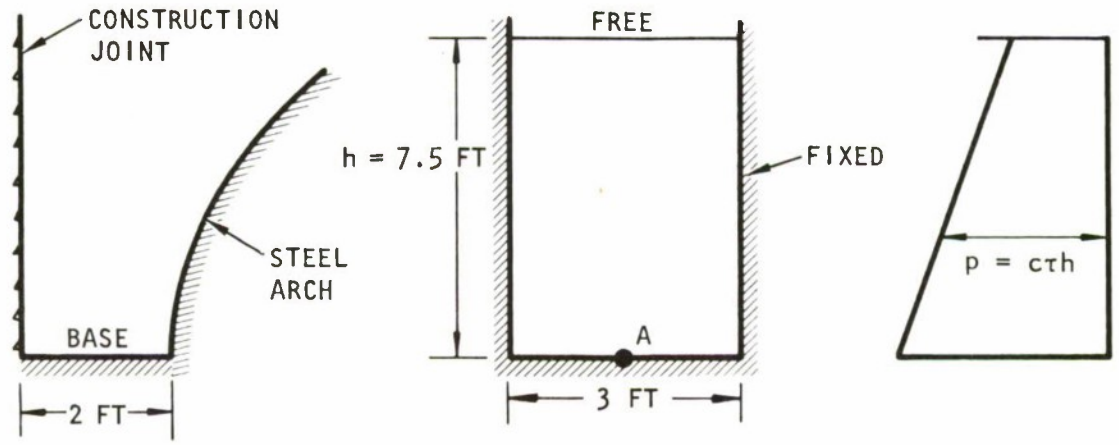

(a) ACTUAL PLATE CONFIGURATION

(b) IDEALIZED PLATE CONFIGURATION

(c) SOIL PRESSURE

FIGURE 3-5. INITIAL MOMENT ON THE HEADWALL (NOT TO SCALE)

where

p = $c_T h$, as defined before for the soil pressure

R = Radius of the arch

t = Thickness of the arch

ν = Poisson ratio

If the total depth (15 ft) of the soil layer is used to compute the moment, it becomes

$$M = 5.7 \text{ kip-in./ft}$$

Although more detailed computation can be made that would take into consideration the actual distribution of the soil pressure and the corrugation of the steel arch, the resulting moment is not likely to be substantially higher than that calculated above. The initial moment is seen to be small and hence can be ignored in calculating the dynamic response of the headwall.

3.3.3 STIFFNESS OF THE SOIL

Actual test data regarding the strength of the compacted soil over the north igloo of the Eskimo I test array are available (Reference 21). In the test, two opposing rams were driven horizontally against the earth fill by a hydraulic jack through circular openings cut in the right and left sides of the corrugated steel arch. Load deflection curves are plotted for the soil over the igloo at the initial stage of the loading and the final stage (five minutes after the application of loads). The spring constants of the soil based on these curves are shown in Table 3-1. It is noted that in the testing, the soil was allowed to settle for the one minute before additional loading was applied. For the quantities of explosives normally stored in magazines, blast pulse durations at distances of interest are of the order of tens of milliseconds. As a consequence, the corresponding stiffness is very high. To arrive at a reasonable dynamic stiffness of the soil, a column of soil subjected to step loading of magnitude P is investigated. The deflection δ at time t is

$$\delta = \frac{PL}{AE}$$

The stiffness is defined as

$$K = \frac{P}{\delta} = \frac{AE}{L}$$

where

A = The cross-sectional area of the soil column

$E = \rho C^2$

L = Ct

C = Wave velocity in the soil medium, 4000 ft/sec is used

ρ = Mass density of the soil, 0.00018 lb-sec^2/in.^{4}

TABLE 3-1. SOIL STIFFNESS FROM TEST IN NORTH IGLOO

Stage	Location	K, lb/in.^{3}		
		P = 0-60 psi	P = 60-270 psi	P > 270 psi
Initial	Right	700	350	230
	Left	666	245	133
Final	Right	600	330	190
	Left	580	235	133

Because of the reflections of the pressure wave at the ends of the soil column, different expressions for the deflections are derived and are illustrated in Figure 3-6(a) to (c). The resulting stiffness with respect to time is shown in Figure 3-6(d).

The dynamic stiffness calculations are based on a one-dimensional wave propagation model. No consideration of soil friction or wave dispersion is made; therefore, the results should be a little higher than test results. In addition, there is ample time during the test for soil to settle; whereas in the dynamic stiffness calculation, there is very little time for soil to settle. The modulus of elasticlty for soil under high pressure conditions is much smaller than that under low pressure conditions, as can be seen in Table 3-1, which shows lower statlc stiffnesses at high pressure levels. It is doubtful that the effect of loading magnitude is important, especially when the peak pressure occurs only within 3 msec duration.

The lowest dynamic stiffness that occurs at 10 msec, 30 msec, 50 msec, etc., is 864 lb/in.^{3} (Figure 3-6(d)), which is slightly higher than static stiffness shown in Table 3-1 (700 and 666 lb/in.^{3} for right and left locations, respectively) in the initial stage. Since the major explosive loadings used in this study were applied to the headwall within the first few milliseconds, the stiffness is subject to rapid change during this period. A value of 1300 lb/in.^{3} is used later in Section 4 to perform linear calculations.

3.3.4 PARTICIPATION OF SOIL MASS

In the linear analysis of the headwall by the SLAB Code the soil stiffness was represented by sprlngs; and the soil mass that was estimated to participate in the dynamic response was lumped together with the mass of the headwall. To estlmate the equivalent soil mass participating in the dynamic response, a model consisting of a unit area of the headwall resting on a column of soil as shown in Figure 3-7(a) was considered. The fundamental

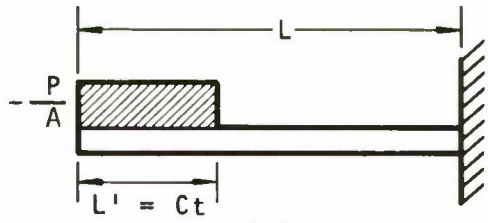

(a)

$$t < \frac{L}{C}$$

$$\delta = \frac{PL'}{AE} = \frac{PCt}{AE}$$

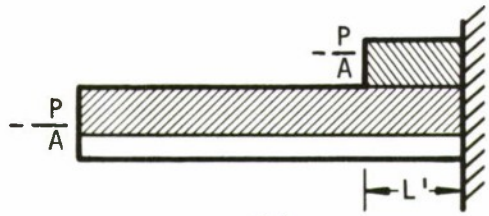

(b)

$$L/C < t < 2L/C$$

$$\delta = \frac{PL}{AE} + \frac{PL'}{AE}$$

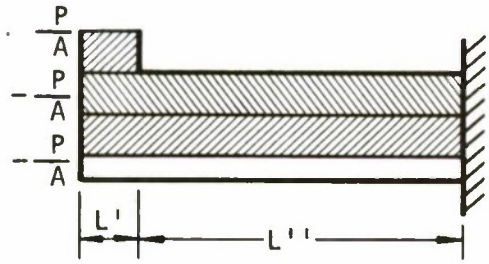

(c)

$$2L/C < t < 3L/C$$

$$\delta = \frac{PL}{AE} + \frac{PL}{AE} - \frac{PL'}{AE}$$

$$= \frac{P(L + L'')}{AE}$$

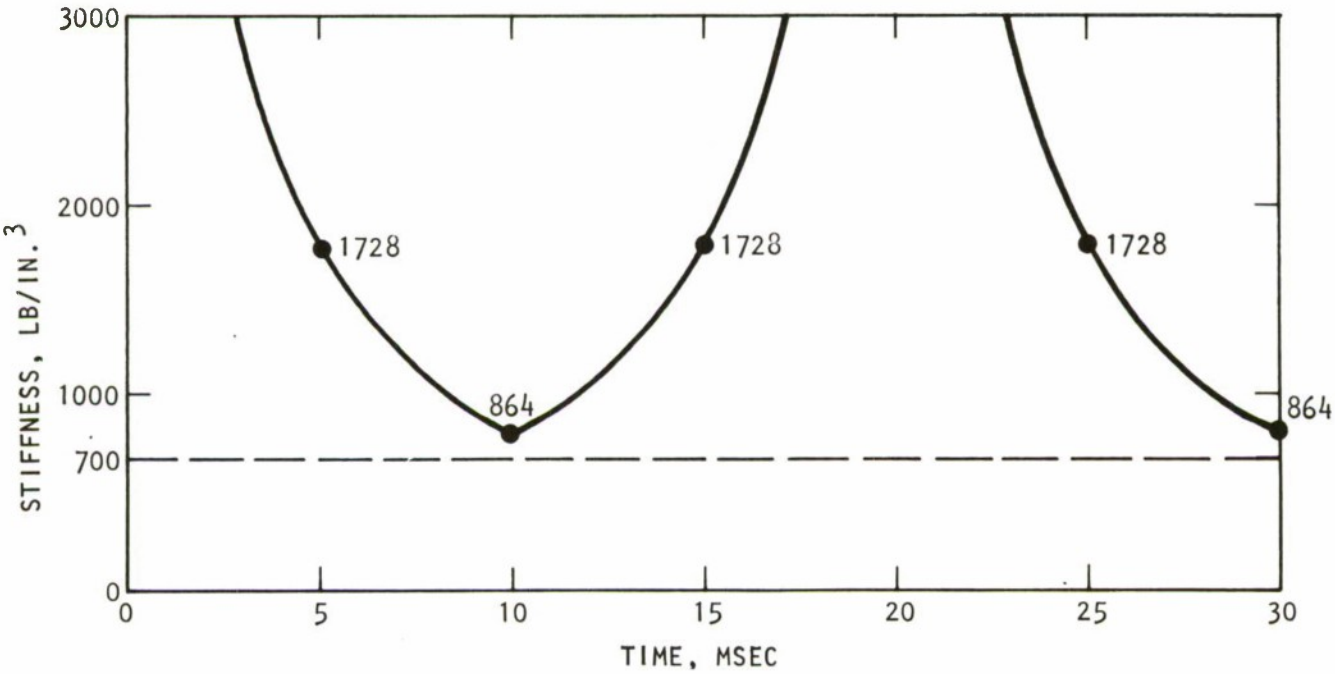

(d)

FIGURE 3-6. DYNAMIC STIFFNESS OF SOIL

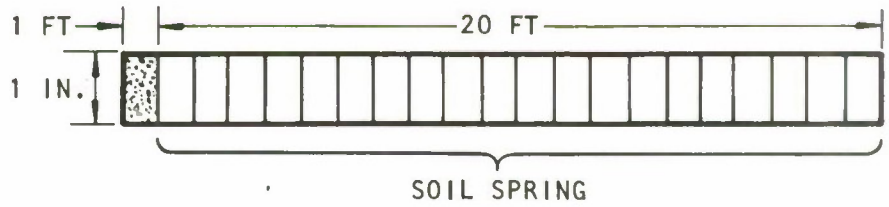

(a) SOIL MODEL FOR CALCULATING PARTICIPATION MASS

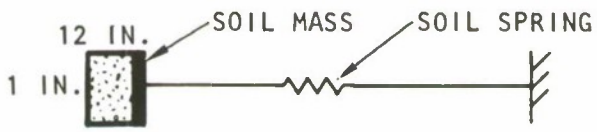

(b) FINITE ELEMENT MODEL FOR THE SOIL

FIGURE 3-7. EFFECTS OF SOIL ON FINITE ELEMENT MODEL

frequency of the concrete-soil, f, was computed to be 54 cps. This value was then used in the frequency model (Figure 3-7(b)).

$$f = \frac{1}{2\pi}\sqrt{\frac{K}{M}}$$

where K is the spring stiffness of the soil.

M is the mass of concrete (m_c) and participating soil (m_s), i.e., $m_c + m_s$. Substituting for

$f = 54$ cps

$K = 1300$ lb/in.

$m_c = 0.269 \times 10^{-2}$ lb-sec^2/in.

a resulting soil mass, m_s, of 0.856×10^{-2} lb-sec^2/in. is obtained, which is about 20 percent of the total soil column. The equivalent mass density of the headwall to include the contribution from the soil is then computed as

$$\rho = 0.938 \times 10^{-3} \text{ lb-sec}^2/\text{in.}^4$$

3.3.5 REPRESENTATION OF THE SOIL BY DAMPERS

While the spring-mass system has been widely used in representing soil properties, the oscillatory nature of the springs sometimes does not provide an adequate description of soil behavior. The soil medium considered in this study is compacted behind the headwall and around and over the top of the steel arch. There will be little rebound of the soil when the headwall is subjected to impact type loading. For this reason viscous damping elements (dashpots) may better represent the soil medium. Massless dashpots with damping coefficient equal to ρC per unit area of headwall are selected on the basis of one-dimensional wave propagation theory, where ρ is the mass density and C is the wave velocity of the soil medium. The damping coefficient is the change in resisting pressure per unit change in headwall velocity.

The simple test cases depicted in Figure 3-8 were used to assess the suitability of representing the earth fill either with the spring-mass systems or dampers. A section of the headwall is sliced along the vertical plane. The base of the headwall is embedded in the ground. The rear of the wall, from the top of the steel arch to the tip of the headwall, is supported by earth fill. In Case A (Figure 3-8(a)), the earth fill is represented by a series of springs and some soil masses attached to the wall. The material properties used are the same as those described in Section 3.2. In Case B (Figure 3-8(b)), the earth fill is represented by a series of dampers with the coefficients equal to ρC. Both models are subjected to the same blast pressure experienced in south igloo. The response time histories at selected locations are shown in Figures 3-9 and 3-10. While in Case A the system oscillates at high frequencies and the motion eventually attenuates to zero, the headwall in Case B (Figure 3-10) does not exhibit any oscillations initially and then stabilizes at a certain nonzero displacement level. According to engineering experience and judgment, the latter system seems to better represent the behavior of earth fill.

The test cases discussed above utilized a general finite element computer program, GENSAP Code, in which both spring and dashpot elements are available. Because it was recognized that the dampers better model the earth fill behind the headwall, the INSLAB Code was modified to accept discrete damping elements. A detailed description of the procedure to include dampers in the program is presented in Appendix B.

3.4 EFFECTS OF THE STEEL ARCH

The material used in the arch is No. 1-gage corrugated steel. Its contribution to the headwall stiffness can be obtained by the procedures described in Section 3.3. Although the corrugation tends to reduce the longitudinal stiffness of the steel arch, the interlocking soil element provides additional strength to the steel arch and the combined effects cannot be evaluated without a more detailed study of this type of structural configuration. However, the net area of the steel arch is so small that its overall effects on the stiffness of the headwall are considered to be negligible.

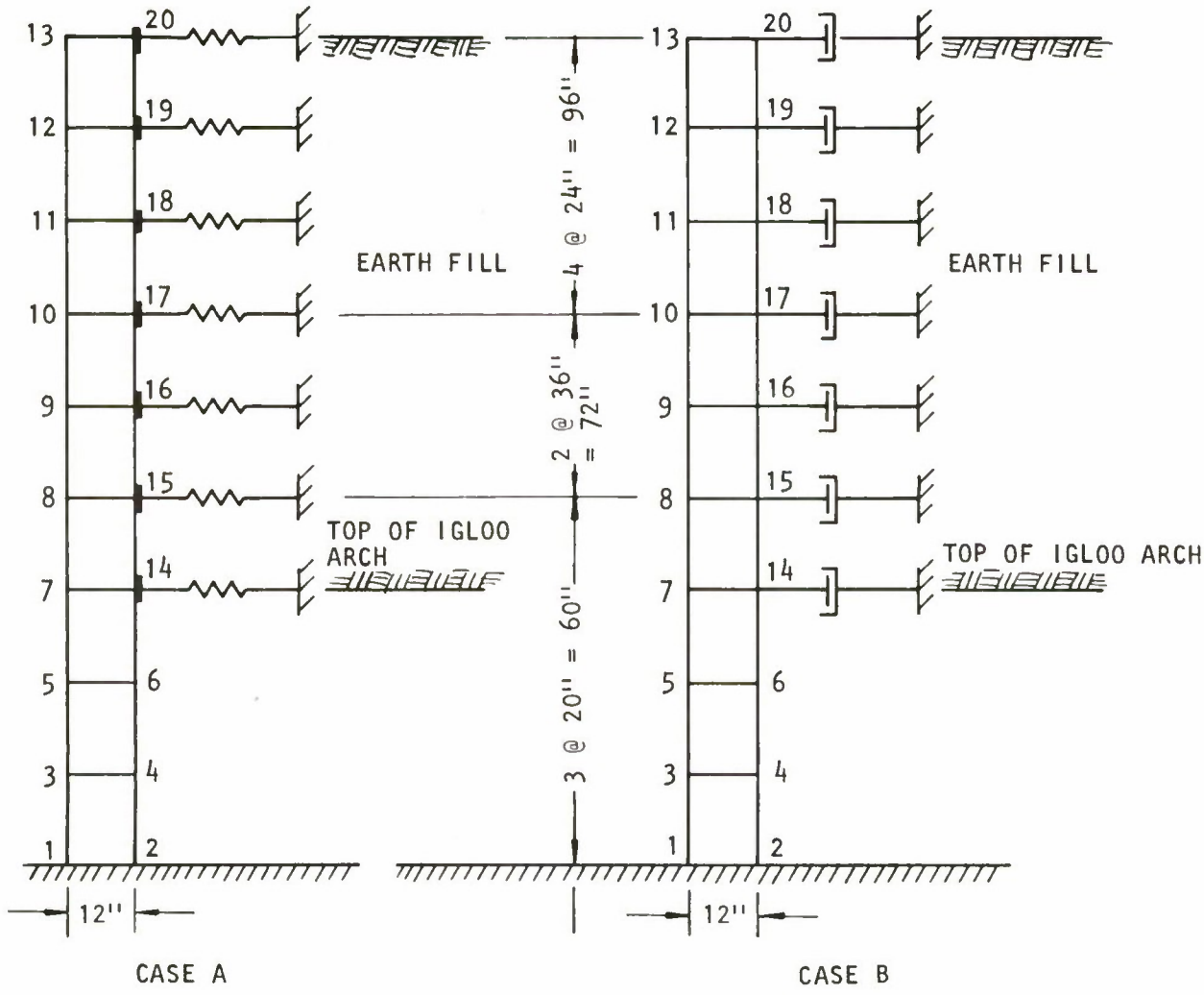

FIGURE 3-8. TEST PROBLEMS WITH SPRING-MASS SYSTEMS AND DAMPERS TO REPRESENT SOIL SUPPORT

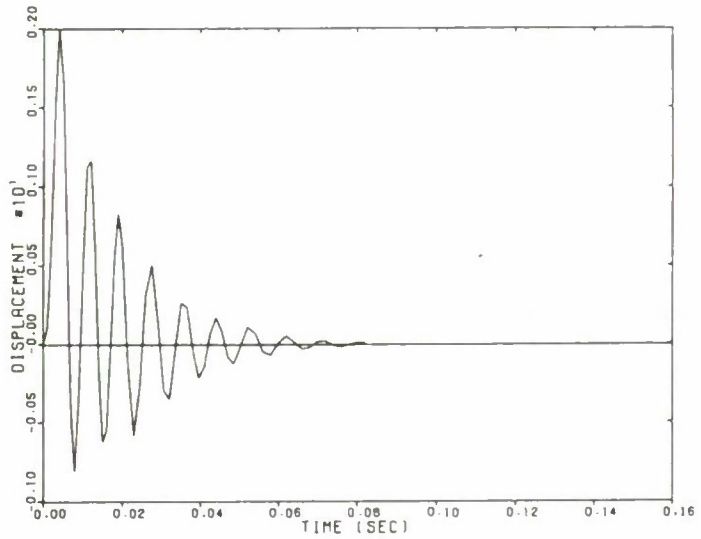

(a) NODE 8

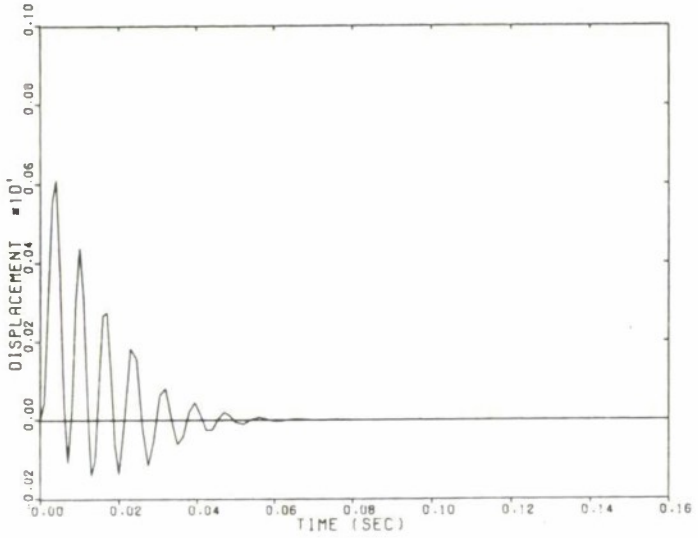

(b) NODE 14

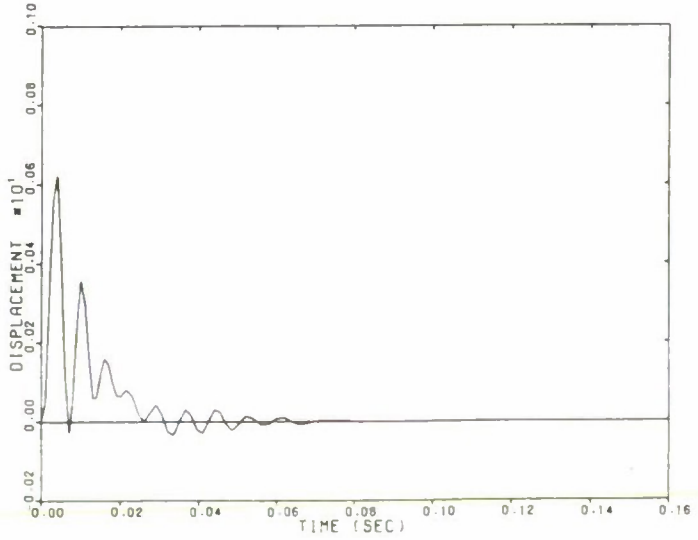

(c) NODE 20

FIGURE 3-9. DISPLACEMENT TIME HISTORIES OF THE HEADWALL USING SPRING-MASS SYSTEM AS SOIL SUPPORT (DISPLACEMENTS ARE IN INCH UNITS)

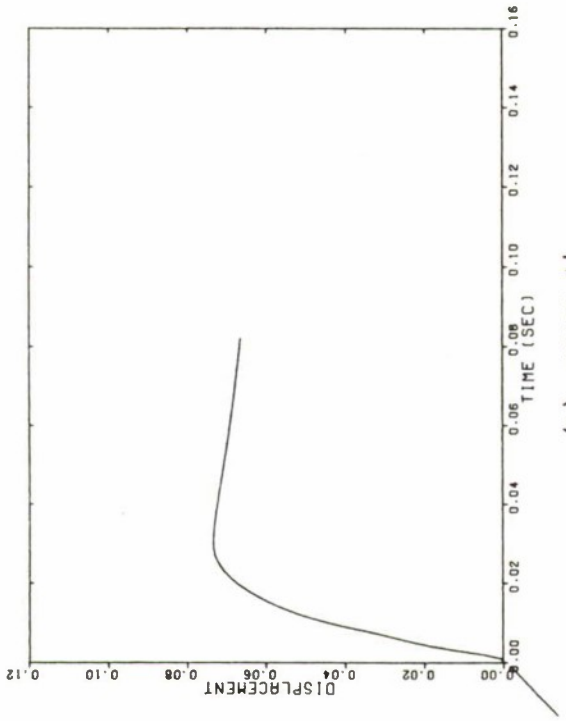

(b) NODE 14

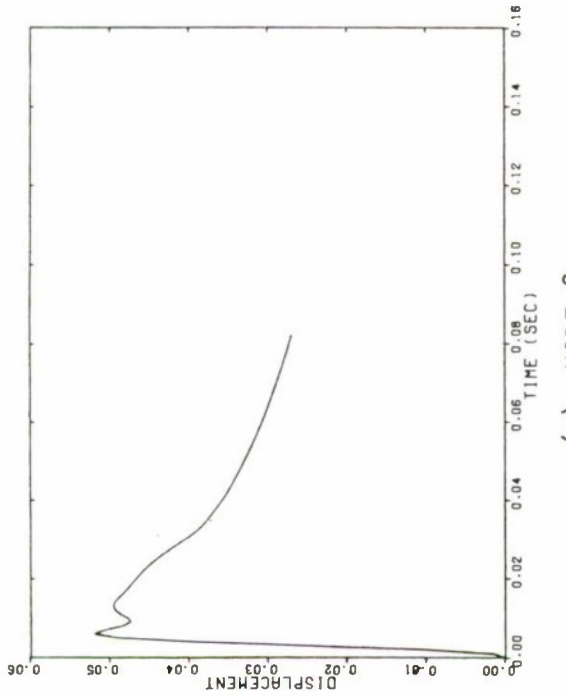

(a) NODE 8

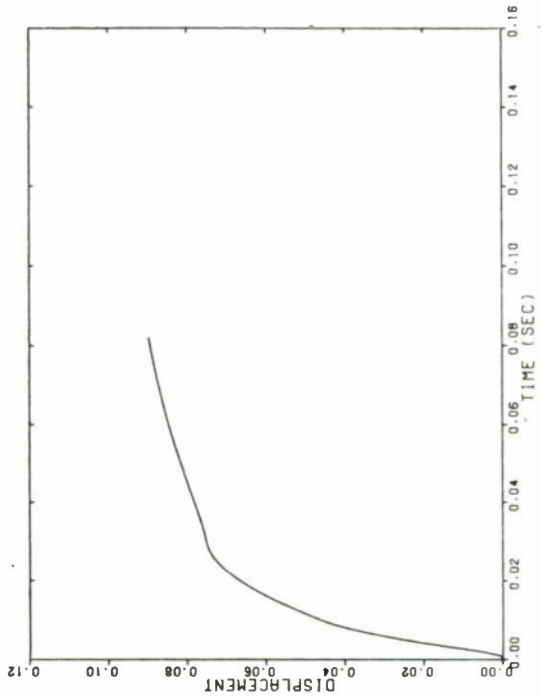

(c) NODE 20

FIGURE 3-10. DISPLACEMENT TIME HISTORIES OF THE HEADWALL USING DAMPERS AS SOIL SUPPORT (DISPLACEMENTS ARE IN INCH UNITS)

As a support to the statement mentioned above, the stiffness of the arch, according to the procedures of Section 3.3, is

$$K = 21,300 \text{ lb/in.}$$

This value is 16.4 times that of soil, whereas the headwall area supported by soil is more than 900 times that supported by the arch. Thus, it is sufficiently accurate in the headwall response study to neglect the stiffness contribution of the steel arch.

The finite element model shown in Figure 3-2 did not provide special elements that were supported by steel arch; therefore, results obtained from the study reflect the average responses of the headwall. The localized effects of the steel arch probably can not be observed.

3.5 BOUNDARY CONDITIONS

In Figure 3-2 several nodal points are assigned with proper boundary conditions to represent the actual physical conditions of the headwall. These boundary conditions are listed below:

a. Soil supports represented by springs and dampers and participating mass attached to the concrete

b. The effect of the steel arch on the headwall is neglected. The arch resistance was found negligible in the preceding section.

c. Door edges connected to the sides of the headwall represented by simply supported hinges, which transfer shears but not moments

d. Intersection of the headwall with the floor, assumed to be fixed

e. Door key, located at the center of the headwall on the floor, represented by a hinge

f. Center line of the headwall except the door, no rotation because of symmetry

The INSLAB and SLAB Codes in their original form did not have the capability to introduce hinges as required under Item *c* above to simulate the connection between the door and headwall. The details of the actual door and headwall connections in the Eskimo I Test are shown in Figures 3-11 and 3-12. These connections permit the transfer of transverse shear forces but no bending moment between the door and headwall. Thus, special procedures were incorporated to allow the edges of adjacent slab and door elements to rotate independently while having compatible transverse displacements. This was accomplished by static condensation (Appendix C) of the element stiffness matrices of door elements. The basic element stiffness matrices for those elements that do not transfer moments are modified by condensing statically the degrees of freedom associated with the zero moment conditions as discussed in Appendix C.

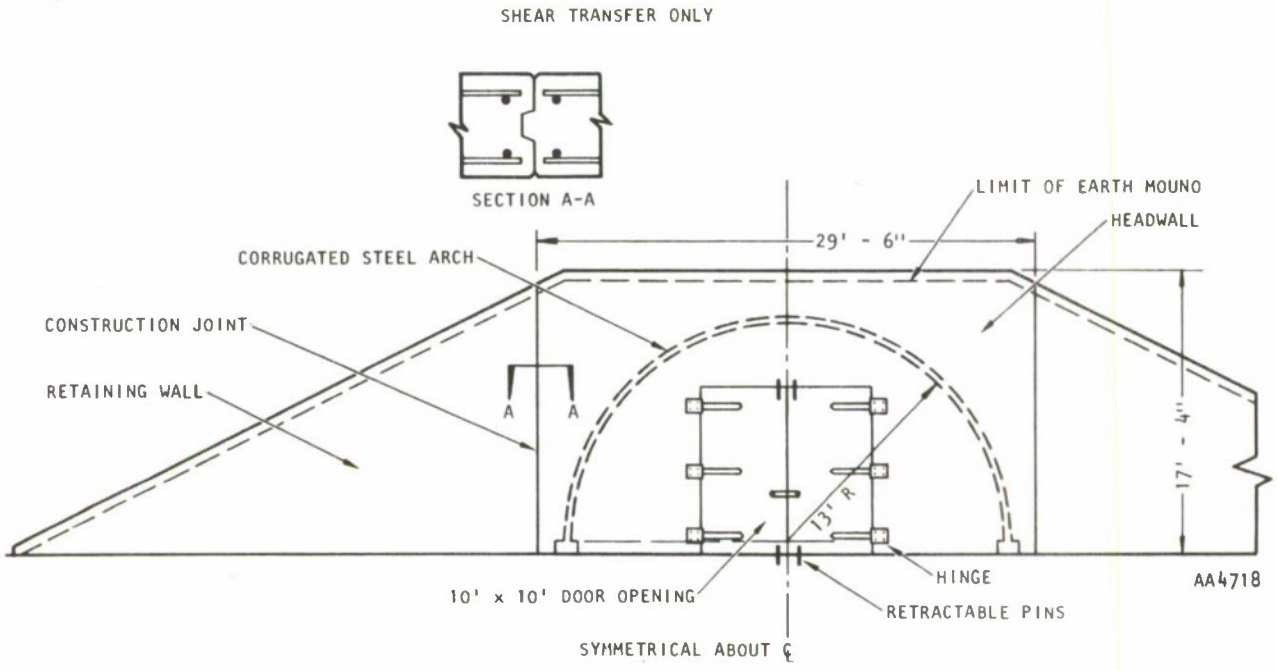

FIGURE 3-11. HEADWALL, DOOR AND RETAINING WALLS

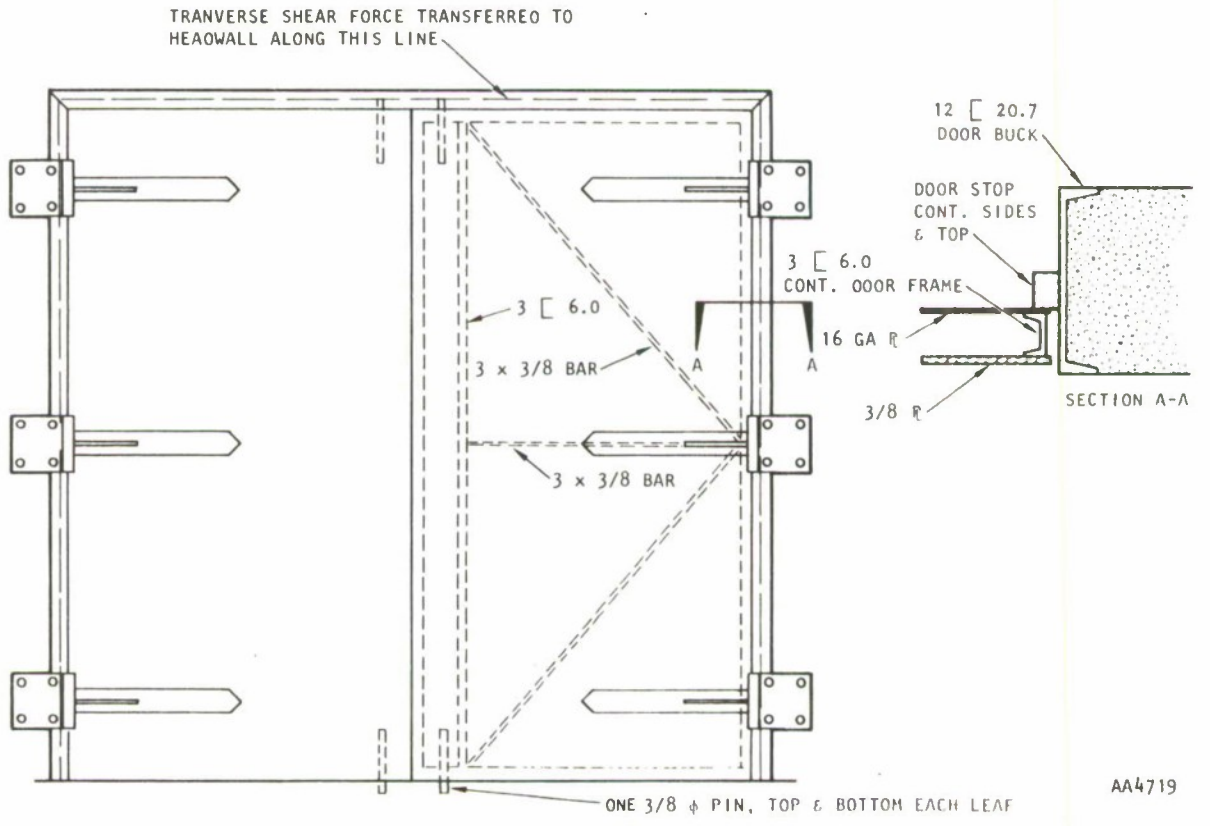

FIGURE 3-12. DETAIL OF DOOR

SECTION 4

LINEAR DYNAMIC RESPONSE OF THE HEADWALL

4.1 INTRODUCTION

The purpose of this section is to describe the results of the dynamic response of the headwall by the SLAB Code, a computer program to solve linear elastic dynamic problems associated with slab configurations. Although the headwall considered in this study experiences stress levels beyond the yield limit, the linear analysis provides valuable information that can be used in the subsequent nonlinear analyses. The frequencies and mode shapes, for example, are useful tools in determining the size of integration time steps and the total duration of the response calculation. The response time histories from the linear and nonlinear calculations are expected to differ significantly both in amplitudes and frequency contents. For a strain-softening system, displacement amplitudes will be greater and the equivalent fundamental frequency* will be lower. These observations can serve as a guide to evaluate the validity of the nonlinear calculations, especially when the system is very complex and no analytical solutions are available for comparison purposes.

Although the same basic finite element mesh is used in the linear and nonlinear calculations, different models are used to represent the soil behind the wall. In nonlinear calculations, the soil is represented by a set of discrete damping elements. Since the SLAB Code is not capable of including the damping elements, the soil is replaced by a set of spring-mass systems.

---

*In a nonlinear system, the fundamental frequency is amplitude dependent. However, response time histories can always be analyzed for their frequency content. The predominant frequencies obtained in this manner are called here "equivalent frequencies."

4.2 RESULTS

As stated above, the SLAB Code is used to obtain the linear dynamic response of the headwall. The program computes response by first extracting a sufficient number of fundamental frequencies and mode shapes of the headwall model presented in Section 3 (Figure 3-2). A modal superposition technique is then used to compute the response time histories at selected points.

A total of 15 modes are extracted and shown in Table 4-1. The first fourteen of these were included in the response calculation. The force time histories used in the calculation are those shown in Figure 2-1 and are applicable for the south and west igloos. The response time histories are calculated at 0.5 msec intervals for 80 steps, with a total duration of 40 msec. No modal damping is considered in the analysis. Some representative time histories of motions and moments are shown in Figures 4-1 through 4-3. Preliminary computations showed that the peak moments at node 47 (Figure 4-3) were considerably higher than the yield moment values.

4.3 DETERMINATION OF INTEGRATION TIME STEPS

This section documents the total number of time steps and the length of each step to be used in the nonlinear dynamic response calculations. Two considerations govern the selection of time steps:

a. The length of each step should be small enough to account for the proper variation of input excitations and to include the responses of all frequencies of interest.

b. The duration used in the response calculations should be long enough to cover the time when absolute maximum response occurs.

After reviewing the input time histories provided in Section 2 and the fundamental frequency of the headwall (Table 4-1), a schedule of time steps to be used in nonlinear analyses of different igloos is prepared as shown in Table 4-2.

TABLE 4-1. NATURAL FREQUENCIES AND PERIODS OF THE HEADWALL

Mode Number	Frequencies (Hz)	Period (Sec)
1	30.8	0.0397
2	39.8	0.0252
3	40.6	0.0246
4	42.5	0.0236
5	45.1	0.0222
6	47.2	0.0212
7	48.2	0.0208
8	52.4	0.0191
9	53.0	0.0189
10	57.4	0.0174
11	62.5	0.0160
12	67.2	0.0149
13	69.4	0.0144
14	74.0	0.0135
15	81.7	0.0122

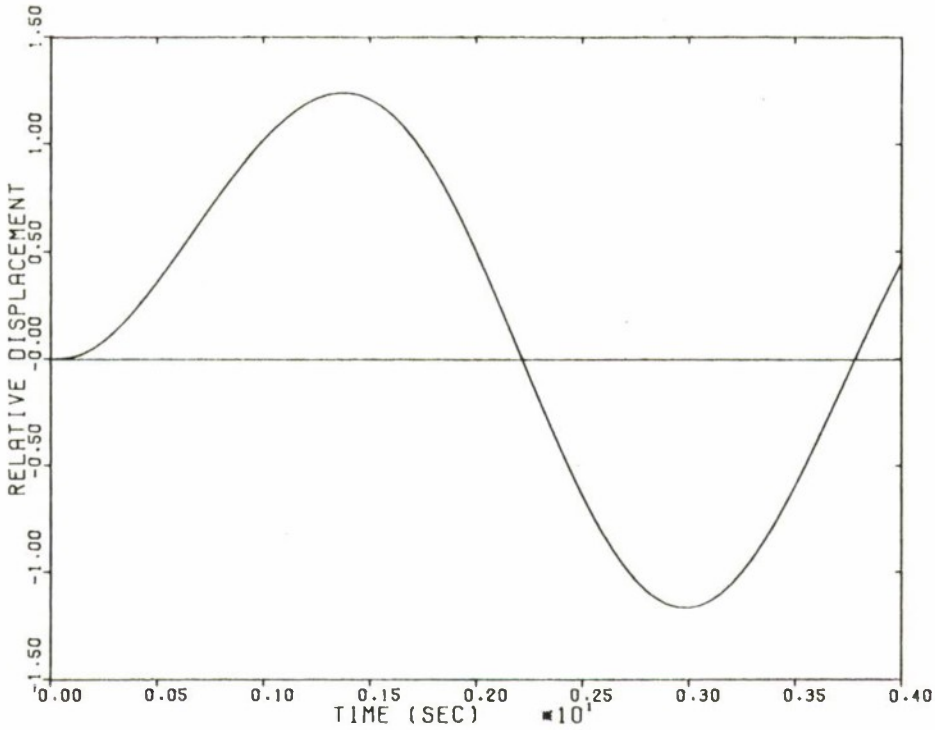

(a) NODE 33

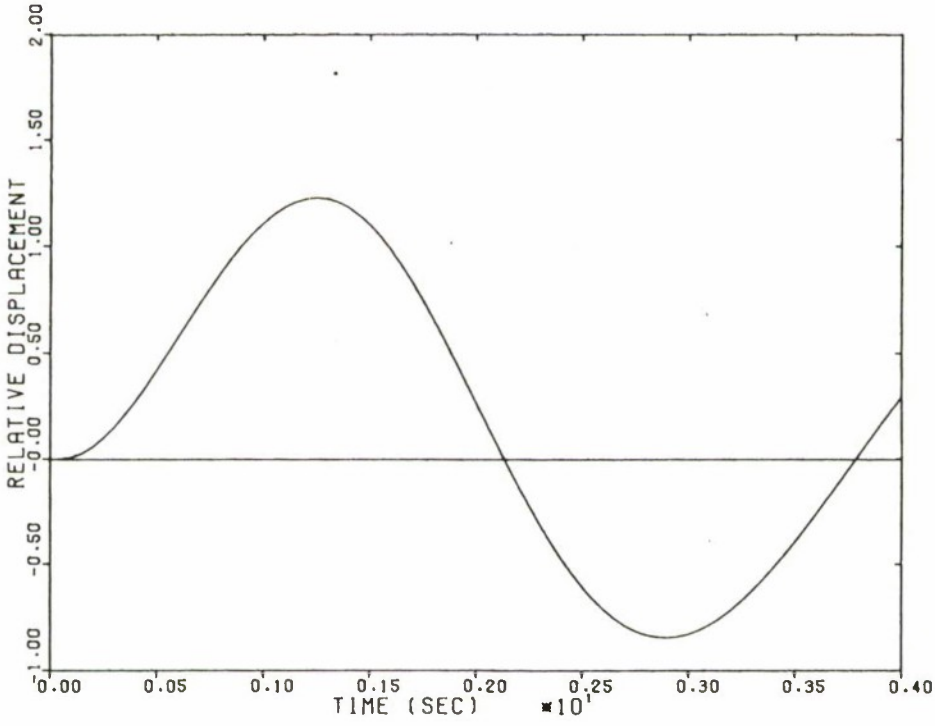

(b) NODE 47

FIGURE 4-1. RELATIVE DISPLACEMENT (IN) TIME HISTORIES

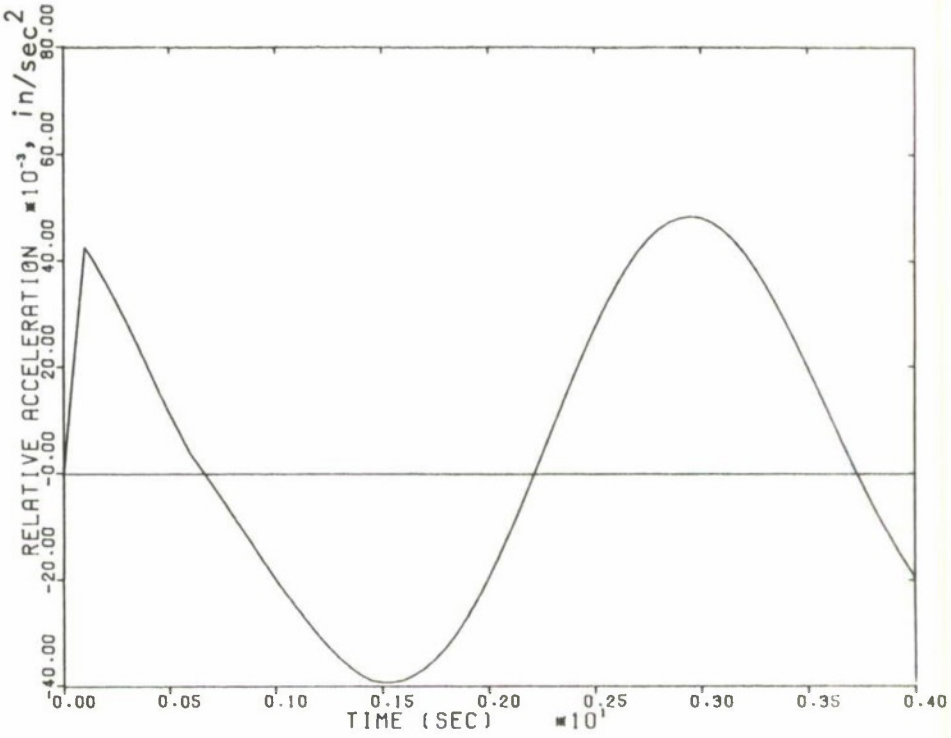

(a) NODE 33

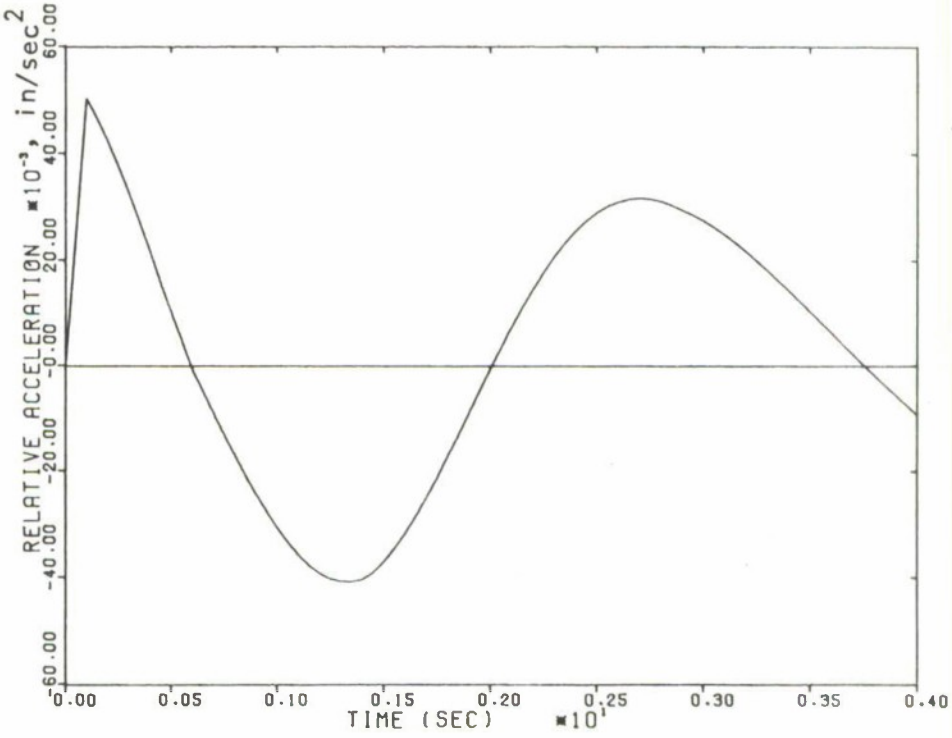

(b) NODE 47

FIGURE 4-2. RELATIVE ACCELERATION (IN/SEC^2) TIME HISTORIES

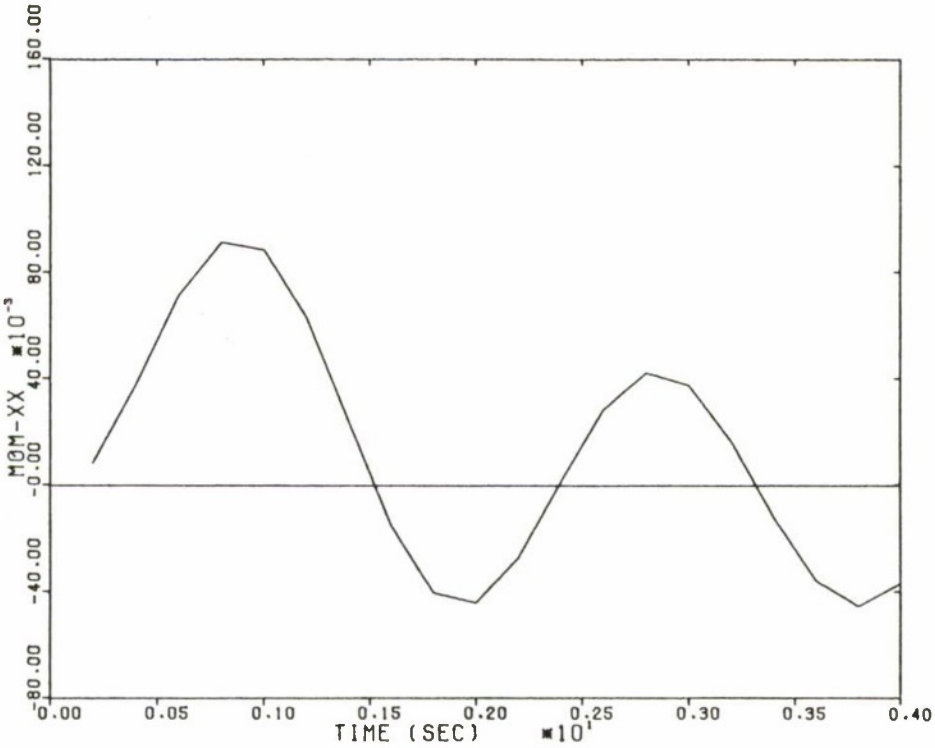

(a) M_{xx}

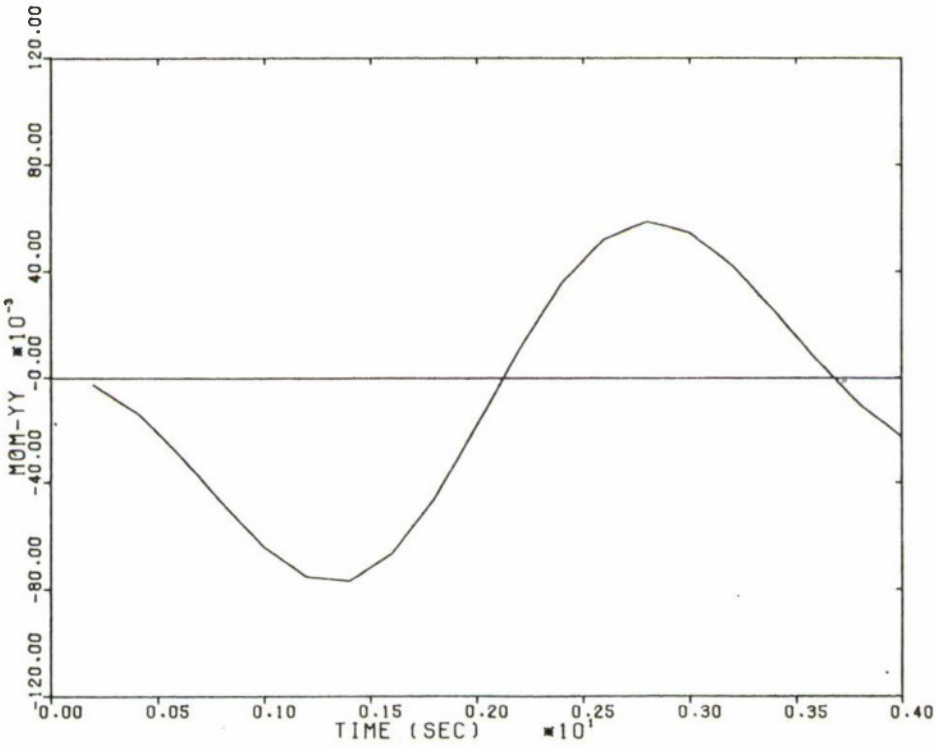

(b) M_{yy}

FIGURE 4-3. MOMENT (IN-KIP/IN) TIME HISTORIES FOR NODE 47

TABLE 4-2. A MATRIX OF TIME STEPS AND DURATIONS USED IN THE ANALYSES

Case No.	Time Step	No. of Steps	Total Steps	Total Duration
Case 1 East Igloo	0.25 msec	12	109*	99.6 msec
	0.40 msec	5		
	0.80 msec	62		
	1.5 msec	30		
Case 2 North Igloo	0.25 msec	12	120	115.4 msec
	0.40 msec	5		
	0.80 msec	63		
	1.5 msec	40		
Case 3 South and West Igloos	0.25 msec	12	131	117.9 msec
	0.40 msec	5		
	0.80 msec	83		
	1.5 msec	31		

*Only the results of the first 60 steps are reported.

In each case, the smallest time step is used during the first 3 msec to account for sharp variations in magnitudes in the input loading. Thereafter, the magnitudes drop and the length of the time step is increased. The basis for deriving the total duration is to add at least one period (39.7 msec) corresponding to the fundamental frequency of the headwall to the duration of the input pressure pulse so that the maximum response occurs within the duration of the response calculations.

SECTION 5

NONLINEAR DYNAMIC RESPONSES OF THE HEADWALL

5.1 INTRODUCTION

The purpose of this section is to describe the nonlinear dynamic response calculations for the four headwall magazines. The mathematical models are identical for all four cases. Since the south and west igloos were exposed to the same blast pressure (Section 2), there are actually only three different calculations identified for south, north, and east igloos. Unlike the linear analysis case, three different calculations are required because the responses are not proportional to input magnitudes when the stresses exceed yield limit.

5.2 RESPONSE OF SOUTH IGLOO

As mentioned above, the response time histories for the south igloo apply to the west igloo as well. In Figures 5-1* to 5-10, the time histories of motion (displacement, velocity, and acceleration) are shown for nodes 7, 16, 28, 31, 33, 46, 47, 48, 49, and 54. The displacements for all the nodes are seen to be building up rapidly in the beginning stage and stabilizing at a level ranging from 5 in. at the bottom of the headwall to about 12 in. at the center of the door. These stabilized values are the permanent displacements commonly observed in the response of nonlinear systems. The maximum displacements at nodes 33 and 47 are compared with the same node in the linear calculation (Figure 4-1). A substantial increase in displacement is observed in the nonlinear calculation. Although different models are used in representing the supporting soil medium, the node selected for the comparison is inside the steel arch; and therefore the increase in displacement in the nonlinear case is predominantly due to nonlinear material behavior.

Like displacements, velocities are found to reach maxima rapidly and then oscillate at smaller amplitudes, with the frequency of oscillation corresponding to the fundamental frequency of the linear system. This is particularly true at nodes within the steel arch. The behavior of the nodes within the arch is different from those outside, due to the presence of the viscous damping elements simulating the soil.

---

*All the figures for Section 5 are located at the end of the section text, pp. 5-6 to 5-42 inclusive.

The test results from the south igloo indicate that no element yields before 2 msec, whereas the rise time of the blast pressure is 1 msec. Therefore, it can be expected that the acceleration time histories before 2 msec are about the same for both linear and nonlinear calculations. After 2 msec, the deviations begin to show up as illustrated at nodes 33 and 47 (see Figures 5-5 and 5-7). The nonlinear calculation shows significant decreases in acceleration amplitudes due to hysteretic damping. In the linear calculation, the acceleration amplitudes remain at a constant level because no damping was assigned.

5.3 RESPONSE OF NORTH IGLOO

The response time histories for the north igloo are shown in Figures 5-11 to 5-20. Since the blast pressures in this case are greater than those of the south igloo, the responses are, in general, greater in magnitude. The displacement at the center of the door (node 49, Figure 5-19) rises to 26 in., then drops off rapidly, and finally oscillates at around the 10-in. level. Because all the maximum responses, except accelerations, occur after the headwall yielded, the results for both south and north igloos are not proportional to the results of the linear solution shown in Section 4. A comparison of the maximum values from the north and south igloos are shown in Table 5-1.

A comparison between the two igloos is also made through contour plots of the displacements. Figures 5-21 to 5-26 show the displacement contours of the north and south igloos at times 31.4 msec, 47.4 msec, and at the ends of the computations. Throughout the computations, the south igloo exhibits the maximum displacements on the door, whereas the north igloo shows a shift of maximum displacements from the center of the door toward the top of the headwall.

5.4 RESPONSE OF EAST IGLOO

The response time histories for the east igloo, shown in Figures 5-27 to 5-36, indicate that the east igloo in general experiences larger magnitudes of response quantities than the north igloo. Although the peak pressure

TABLE 5-1. COMPARISON OF MAXIMUM RESPONSES BETWEEN NORTH AND SOUTH IGLOOS

Nodes	Displacement in.		Velocity in./sec		Acceleration in./sec^2	
	North	South	North	South	North	South
7	10.97	6.05	214.4	125.6	1.2×10^5	0.30×10^5
16	10.22	6.06	260.2	142.5	0.97×10^5	0.24×10^5
28	8.39	5.22	256.0	149.9	1.1×10^5	0.27×10^5
31	9.62	5.90	350.9	198.8	1.5×10^5	0.37×10^5
33	10.71	6.73	502.4	241.1	2.0×10^5	0.50×10^5
46	8.33	5.03	390.8	183.0	1.2×10^5	0.35×10^5
47	9.86	5.92	495.1	224.7	1.9×10^5	0.48×10^5
48	17.38	8.22	1300.0	547.7	7.1×10^5	1.8×10^5
49	26.62	10.55	2500.0	913.6	7.4×10^5	2.4×10^5
54	6.90	4.71	274.3	162.9	1.4×10^5	0.35×10^5

is almost two times greater (525 vs. 300), the duration of the high pressure pulse for the east igloo is only about half as long as that for the north igloo. Thus the impulses, defined as the areas under the input pressure time histories, on the north and east igloos are about the same. For short duration pulses the resulting velocity of the headwall should be proportional to the amount of impulse applied. This serves to explain the small differences in the maximum velocities between north and east igloos. The accelerations are higher (though not proportionally) in the east igloo than in the north igloo.

All the time history plots shown were terminated at about 40 msec, although the calculations were performed up to about 100 msec. After about 40 msec, all the time histories exhibited unstable oscillations not experienced in the previous calculations for the north and south igloos. Since the mathematical model and the integration time steps are the same for all cases, it is believed that the instability was due to significantly large changes in displacements within one integration step. The large and abrupt changes of displacements may give rise to an erroneous formulation of structural stiffness. A reduction in the duration of integration time steps, especially at later times, can be used to eliminate the numerical instability, but will increase computer time and costs. However, the gain from this extra effort is expected to provide no realistic additional information because the displacements of the doorways are observed to be as high as 28 in. (see Table 5-2), which indicates that the doors have been already blown open. To continue the calculations beyond this point, the structural model of the headwall must be reformulated. Furthermore, the extent of damage caused by the blast was masked by the subsequent detonation of the acceptor charges within the igloo in the actual test, so the comparisons of the field data with the computed response of the headwall will not be meaningful. For these reasons, additional calculations using the present finite element model of the east igloo are considered unnecessary.

TABLE 5-2. MAXIMUM RESPONSES OF THE EAST IGLOO

Node	Displacement East in.	Velocity East in./sec	Acceleration East $in./sec^2$
7	7	230	2.0×10^5
16	8.2	280	1.8×10^5
28	8.2	280	1.90×10^5
31	10.5	400	2.60×10^5
33	11.6	590	3.6×10^5
46	9.0	440	2.2×10^5
47	10.6	580	3.4×10^5
48	18.5	1600	12.4×10^5
49	28.5	3050	12.8×10^5
54	7.3	300	2.4×10^5

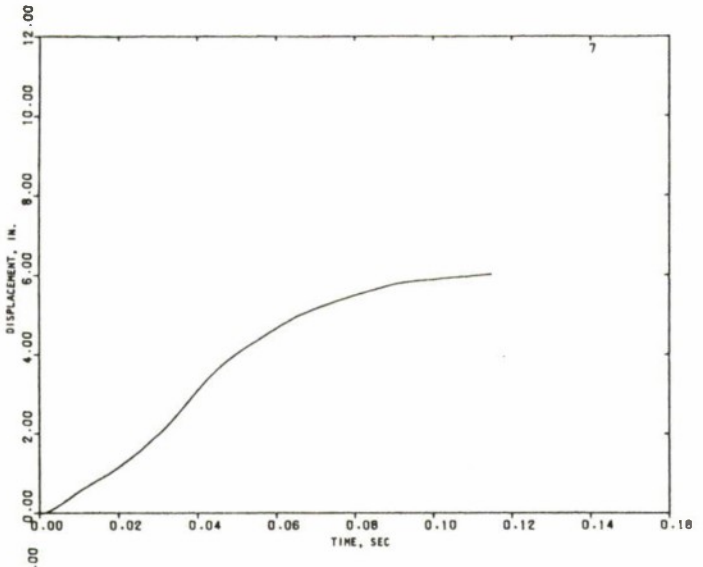

(a) DISPLACEMENT

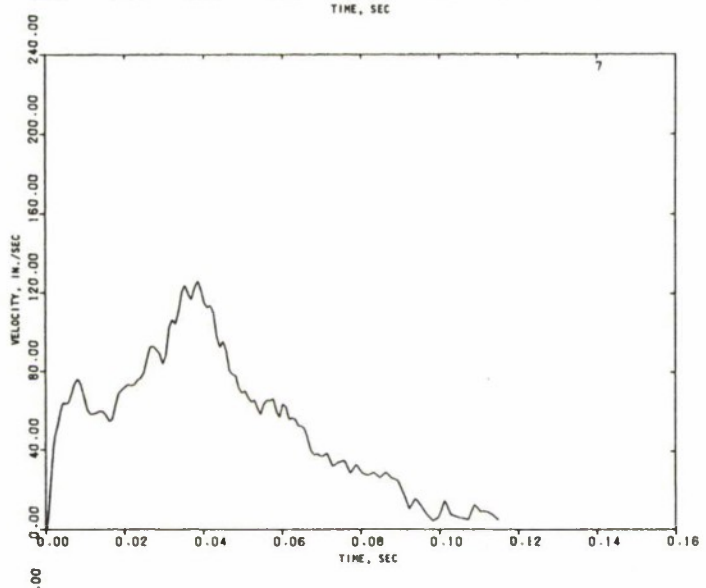

(b) VELOCITY

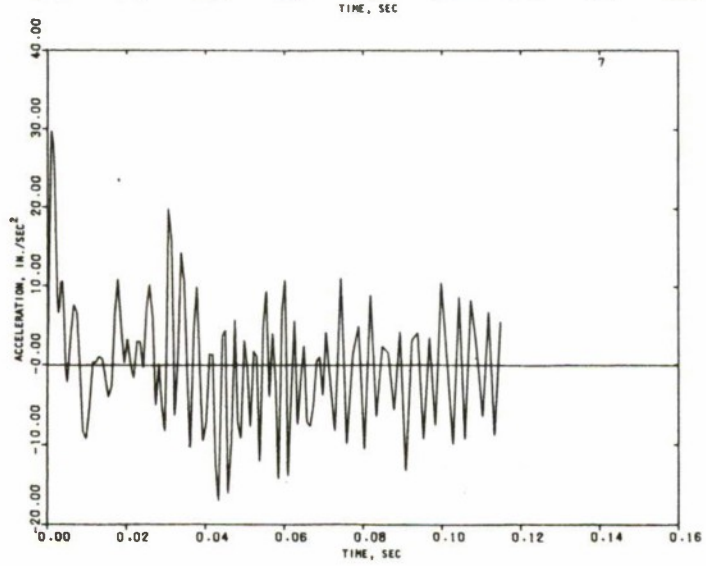

(c) ACCELERATION

FIGURE 5-1. MOTION TIME HISTORIES OF THE SOUTH IGLOO (NODE 7)

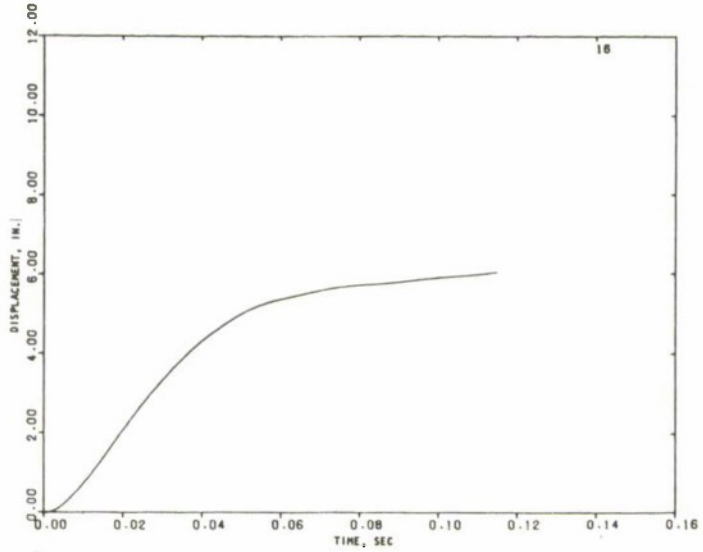

(a) DISPLACEMENT

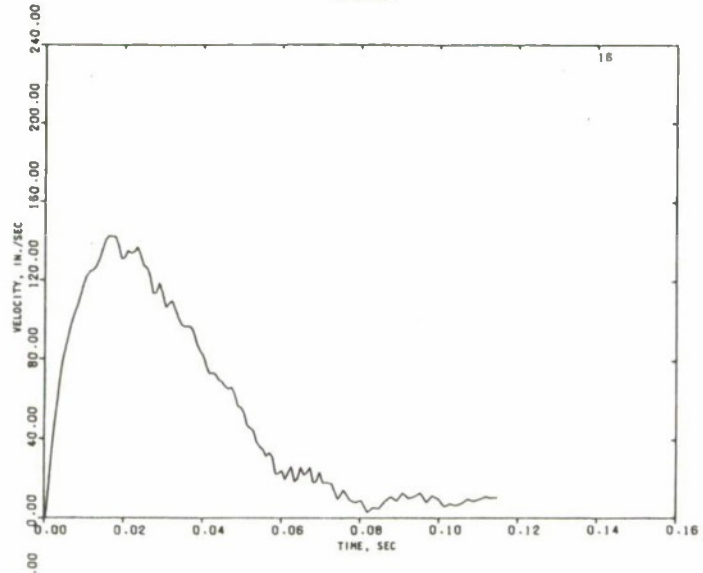

(b) VELOCITY

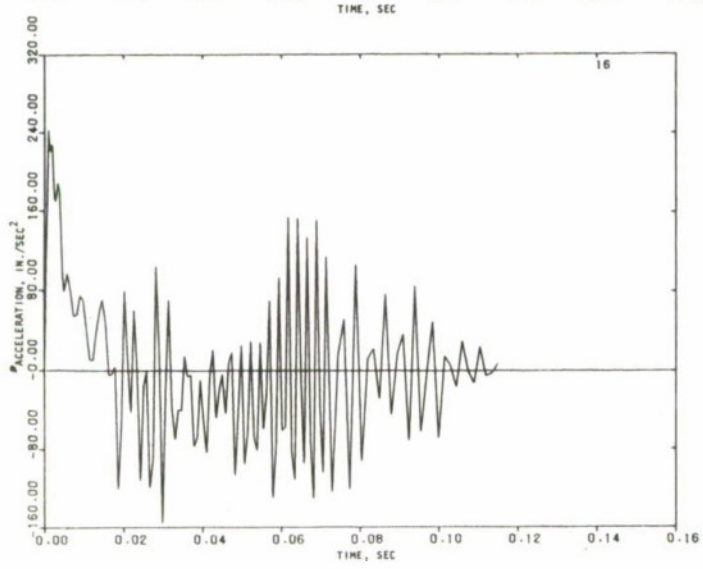

(c) ACCELERATION

FIGURE 5-2. MOTION TIME HISTORIES OF THE SOUTH IGLOO (NODE 16)

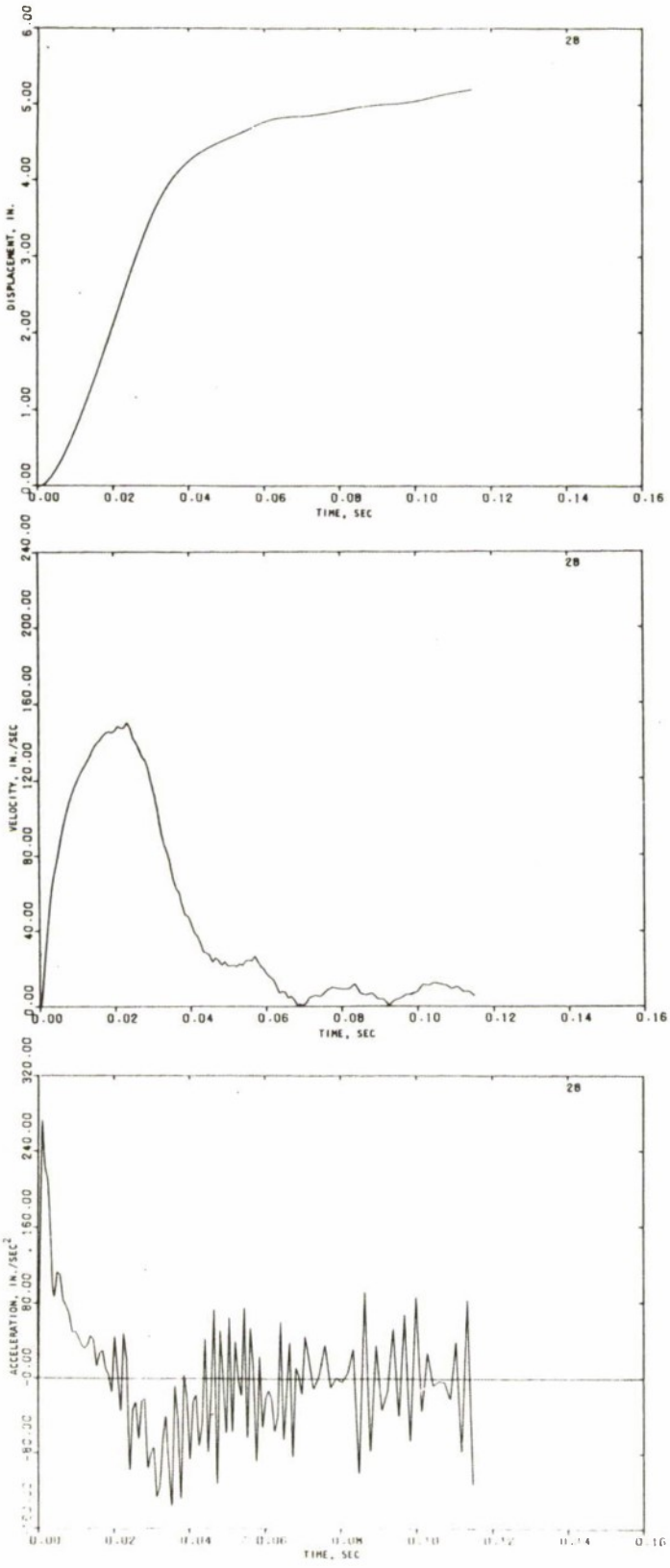

(a) DISPLACEMENT

(b) VELOCITY

(c) ACCELERATION

FIGURE 5-3. MOTION TIME HISTORIES OF THE SOUTH IGLOO (NODE 28)

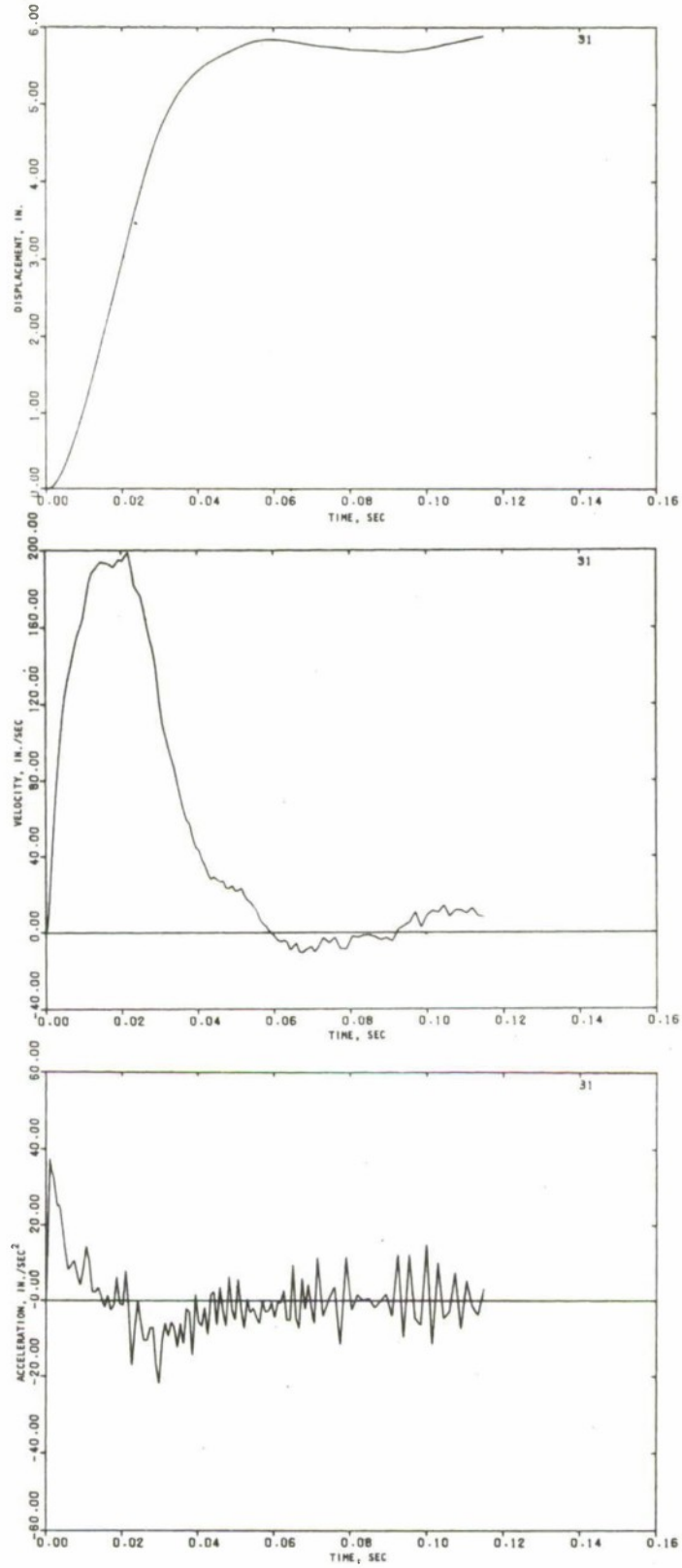

(a) DISPLACEMENT

(b) VELOCITY

(c) ACCELERATION

FIGURE 5-4. MOTION TIME HISTORIES OF THE SOUTH IGLOO (NODE 31)

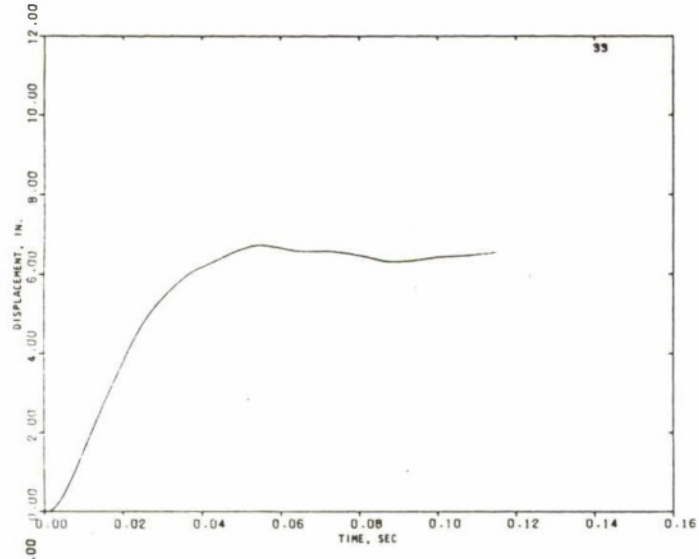

(a) DISPLACEMENT

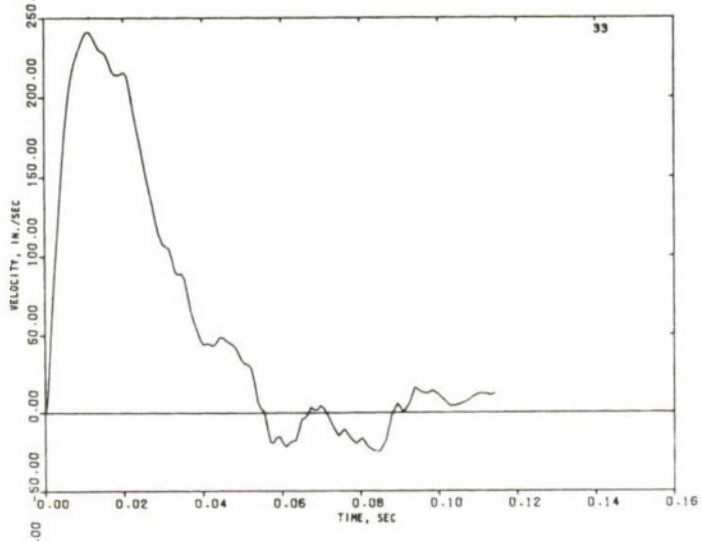

(b) VELOCITY

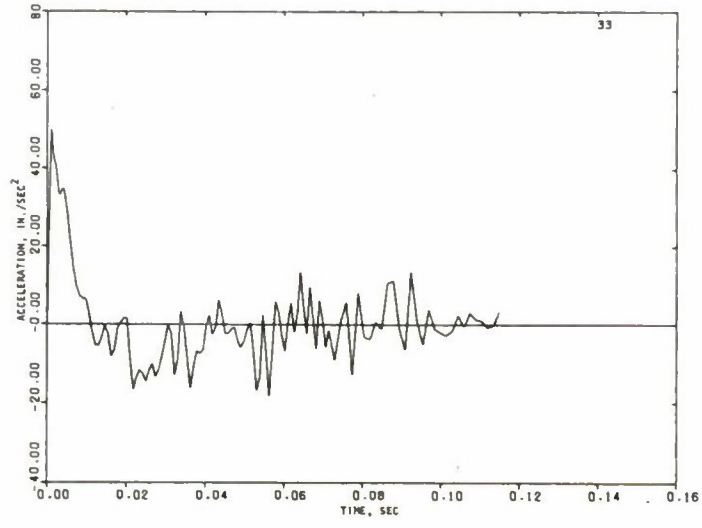

(c) ACCELERATION

FIGURE 5-5. MOTION TIME HISTORIES OF THE SOUTH IGLOO (NODE 33)

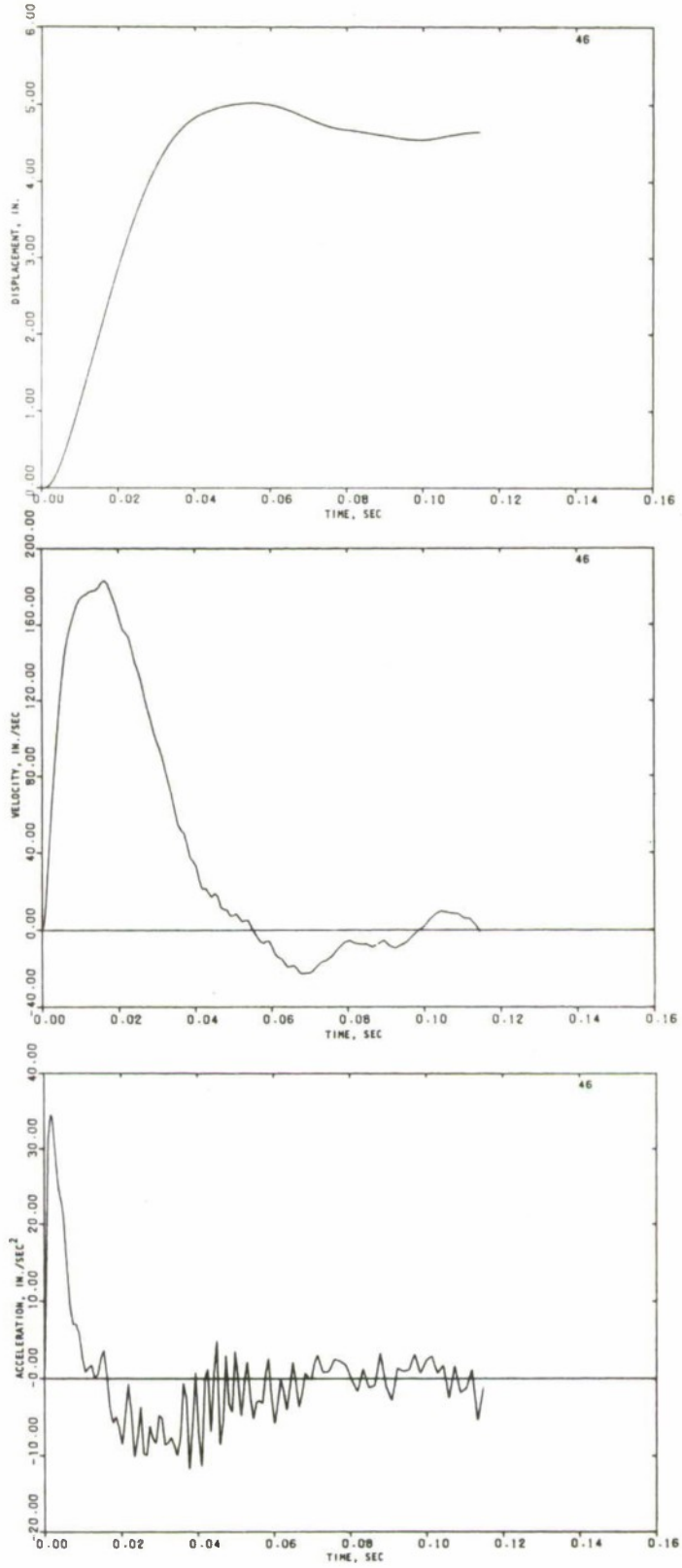

(a) DISPLACEMENT

(b) VELOCITY

(c) ACCELERATION

FIGURE 5-6. MOTION TIME HISTORIES OF THE SOUTH IGLOO (NODE 46).

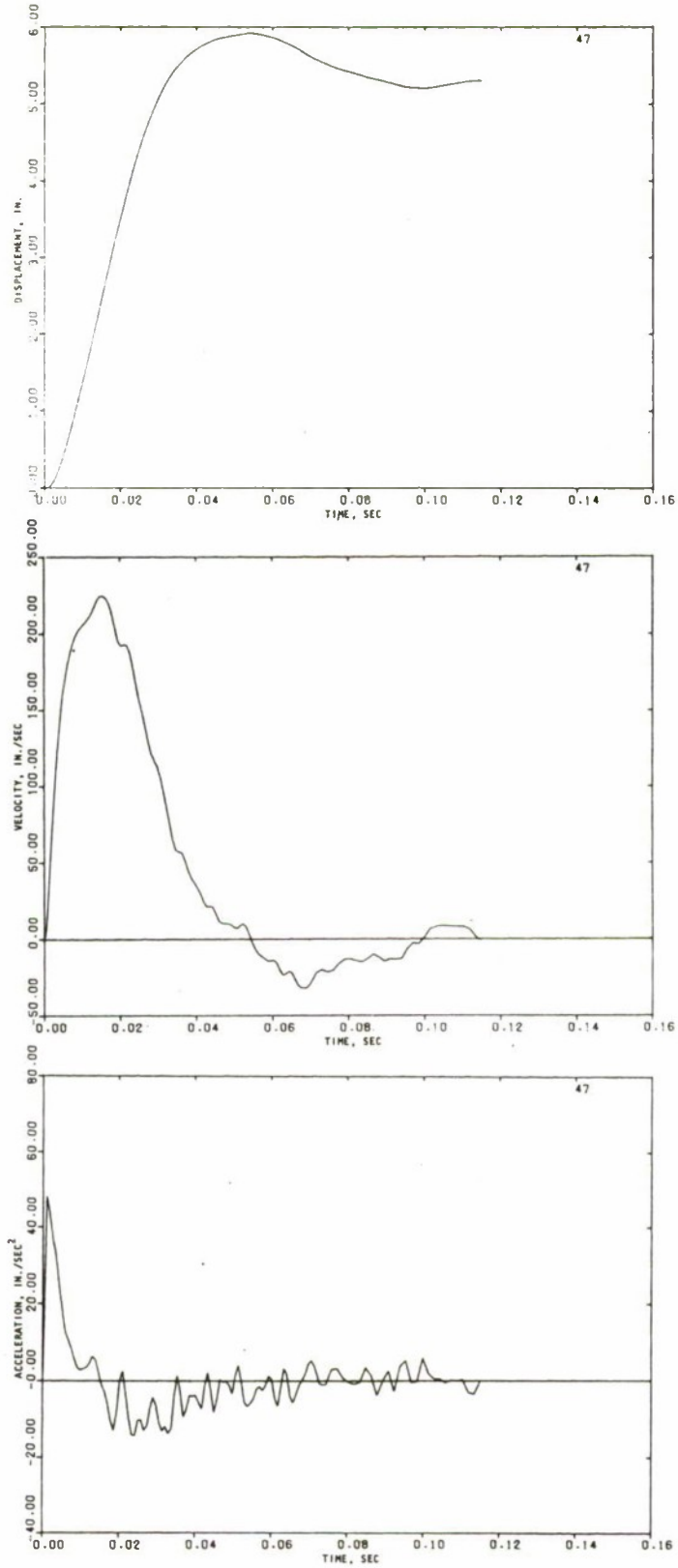

FIGURE 5-7. MOTION TIME HISTORIES OF THE SOUTH IGLOO (NODE 47)

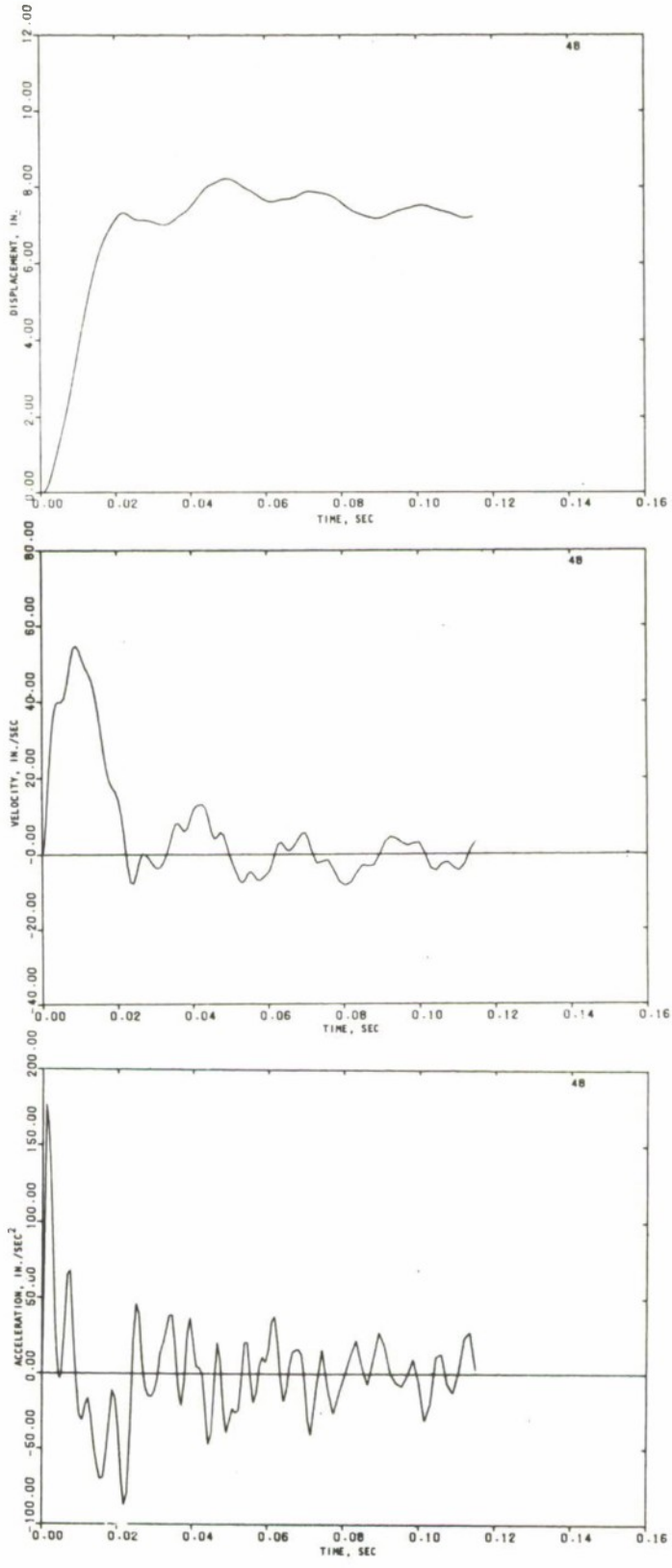

(a) DISPLACEMENT

(b) VELOCITY

(c) ACCELERATION

FIGURE 5-8. MOTION TIME HISTORIES OF THE SOUTH IGLOO (NODE 48)

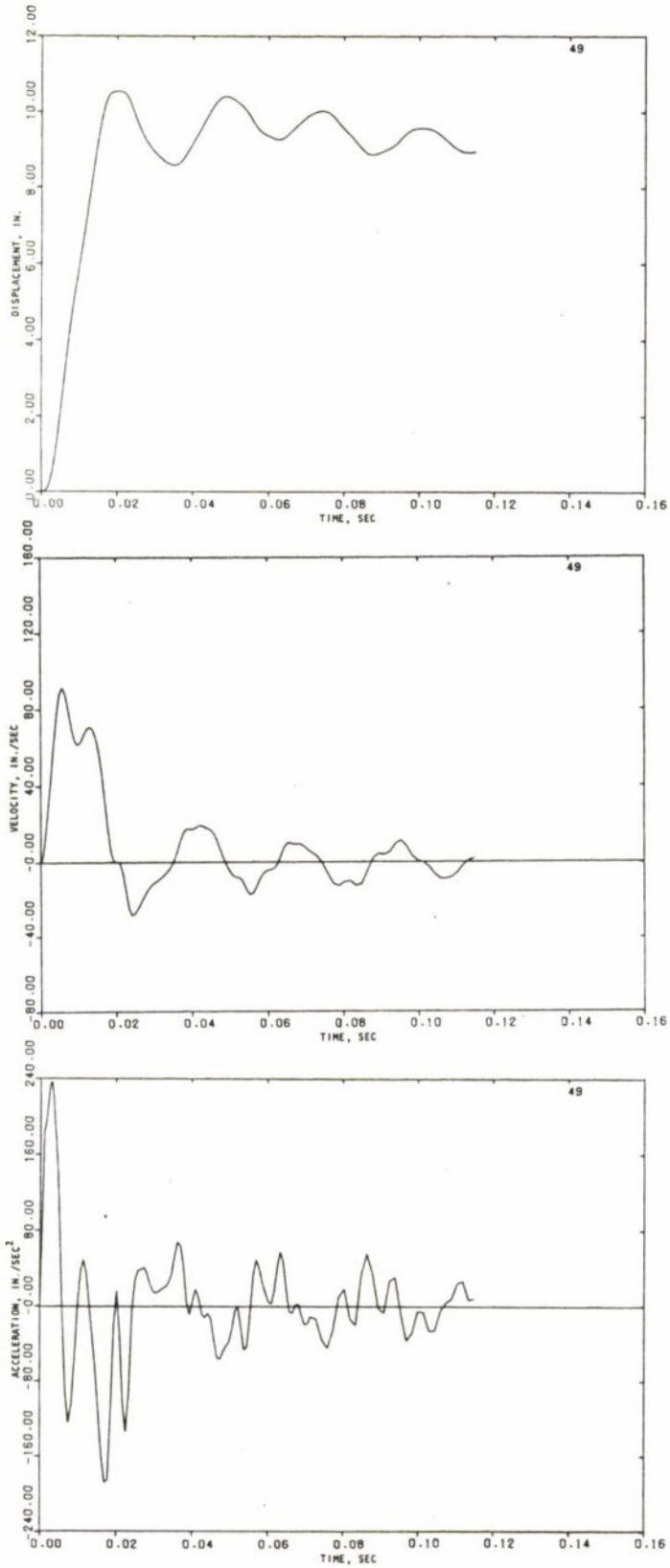

(a) DISPLACEMENT

(b) VELOCITY

(c) ACCELERATION

FIGURE 5-9. MOTION TIME HISTORIES OF THE SOUTH IGLOO (NODE 49)

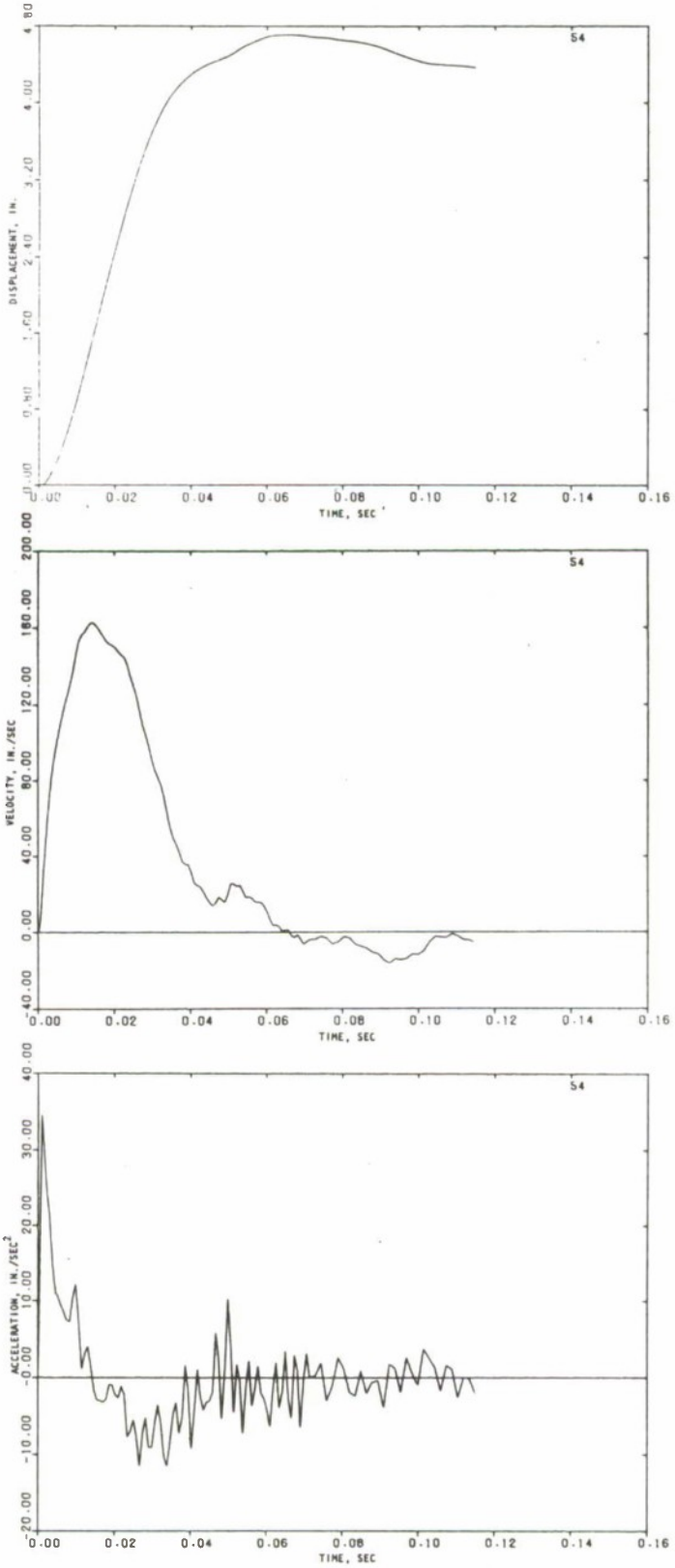

FIGURE 5-10. MOTION TIME HISTORIES OF THE SOUTH IGLOO (NODE 54)

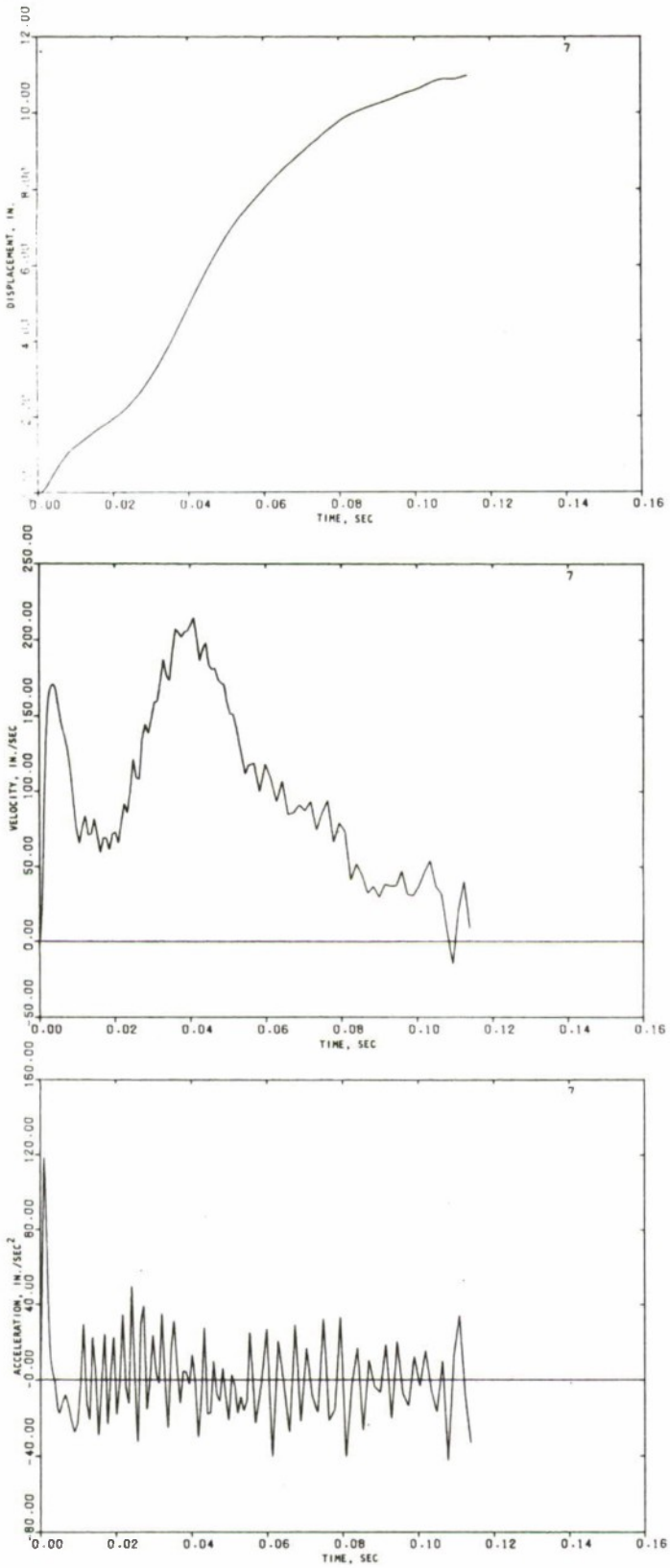

FIGURE 5-11. MOTION TIME HISTORIES OF THE NORTH IGLOO (NODE 7)

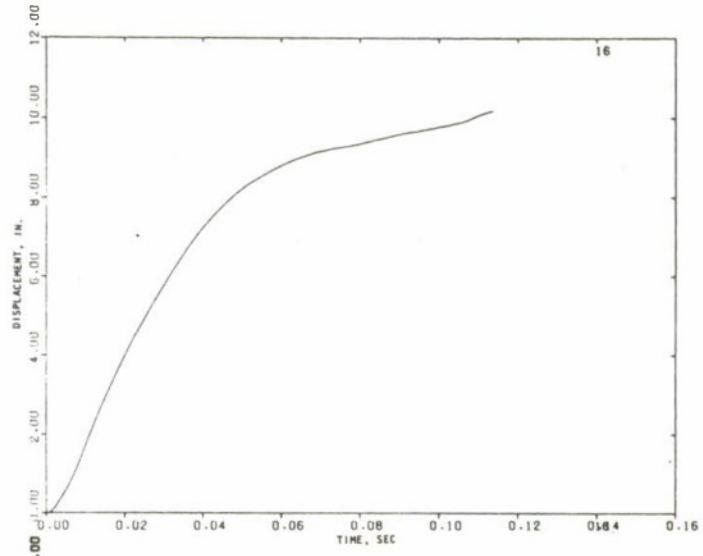

(a) DISPLACEMENT

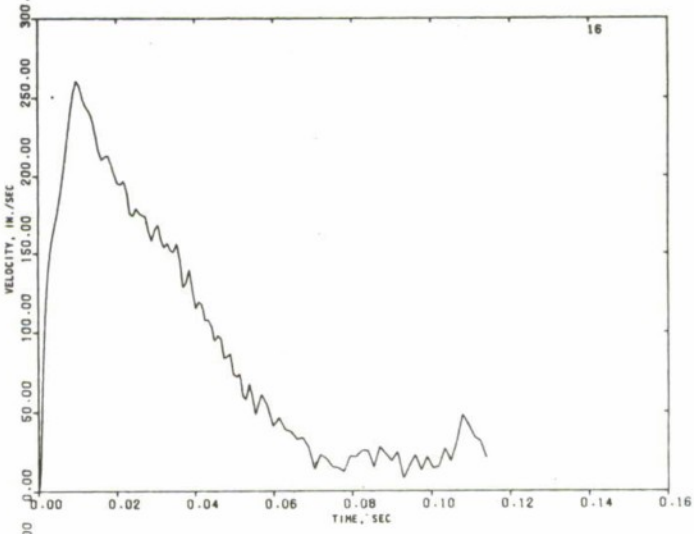

(b) VELOCITY

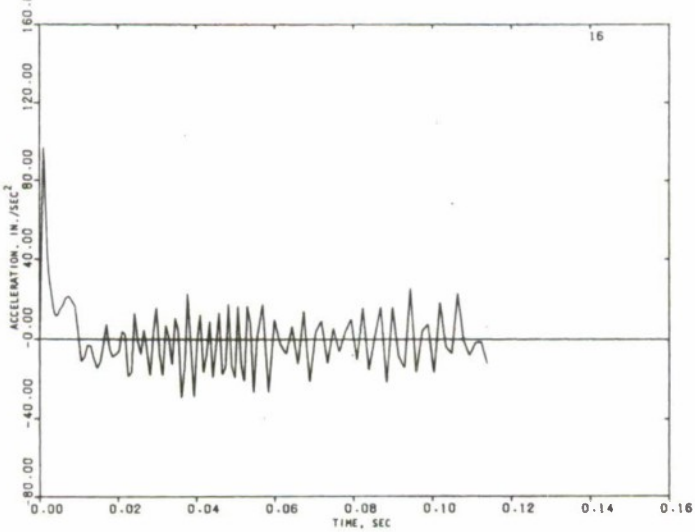

(c) ACCELERATION

FIGURE 5-12. MOTION TIME HISTORIES OF THE NORTH IGLOO (NODE 16)

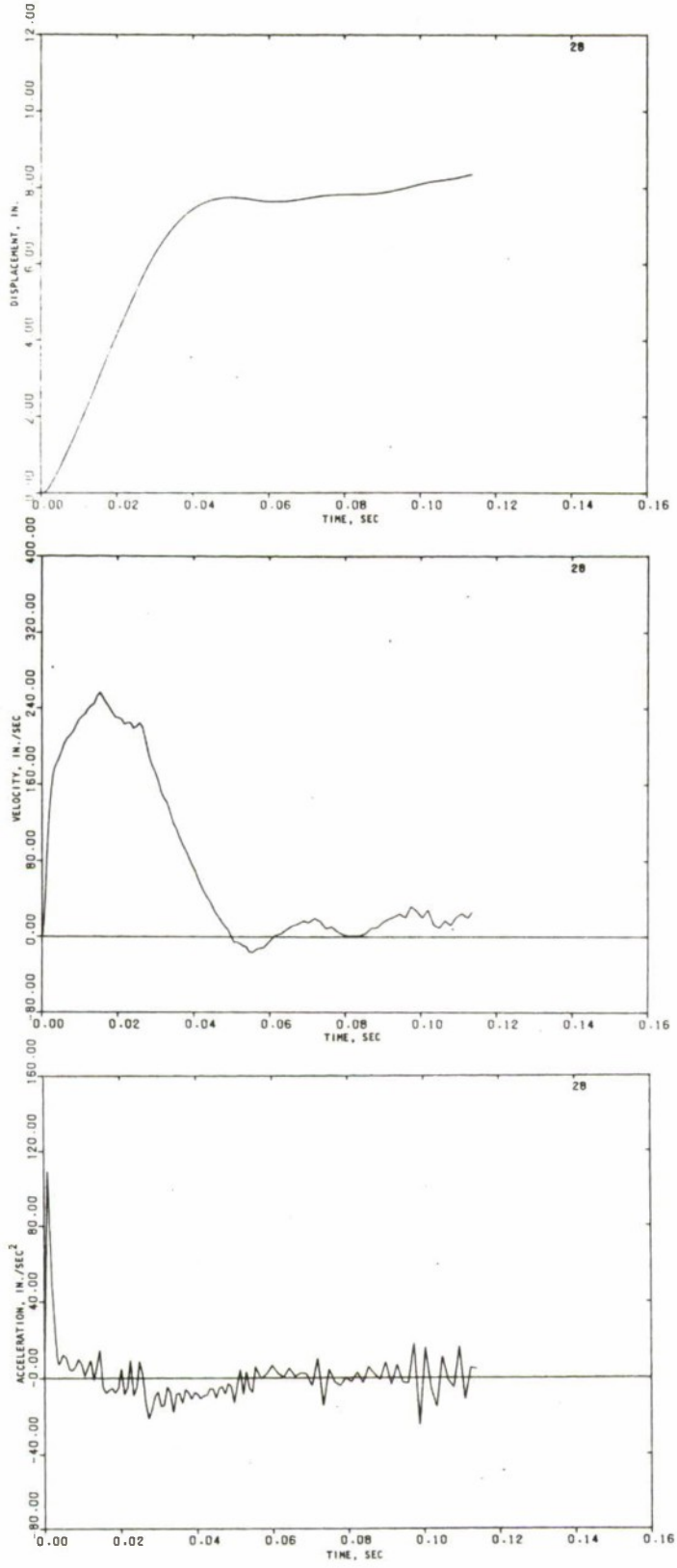

(a) DISPLACEMENT

(b) VELOCITY

(c) ACCELERATION

FIGURE 5-13. MOTION TIME HISTORIES OF THE NORTH IGLOO (NODE 28)

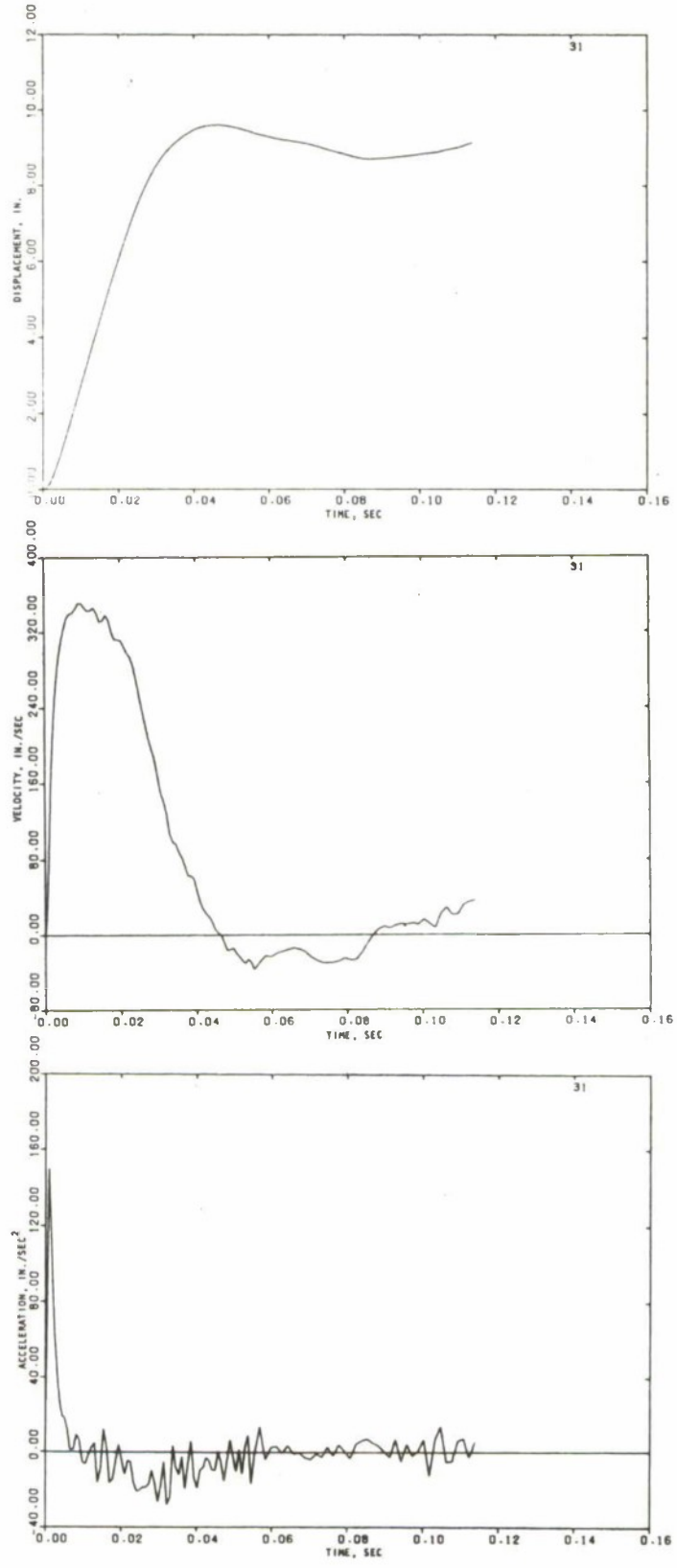

FIGURE 5-14. MOTION TIME HISTORIES OF THE NORTH IGLOO (NODE 31)

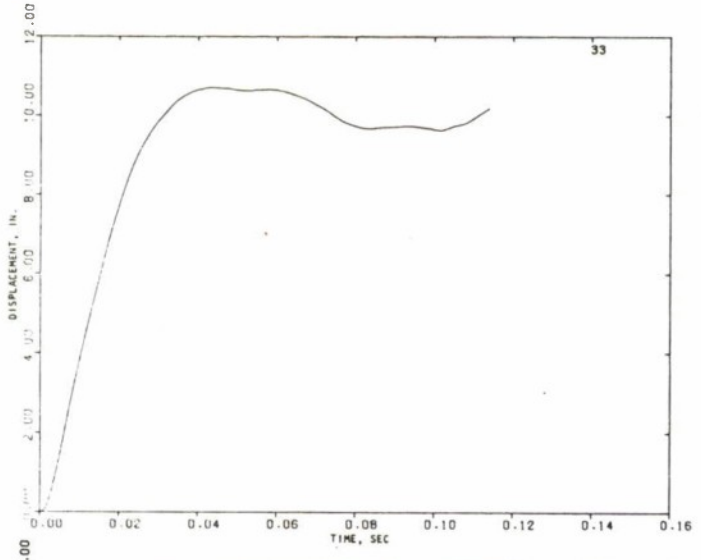

(a) DISPLACEMENT

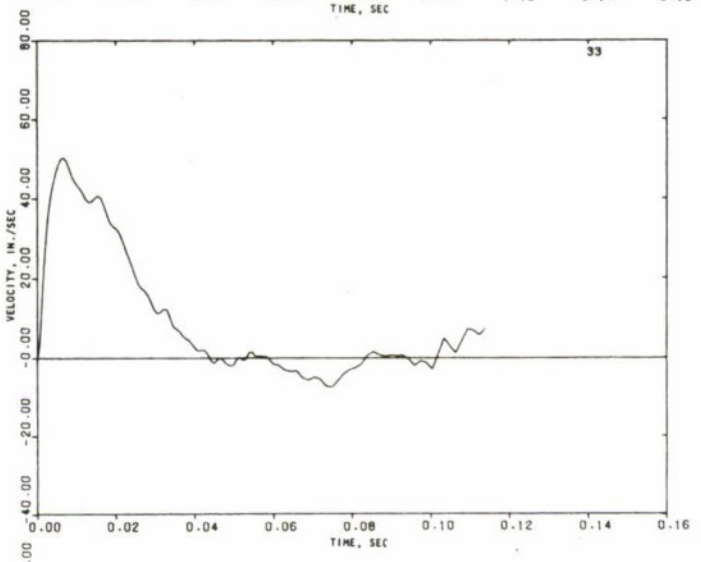

(b) VELOCITY

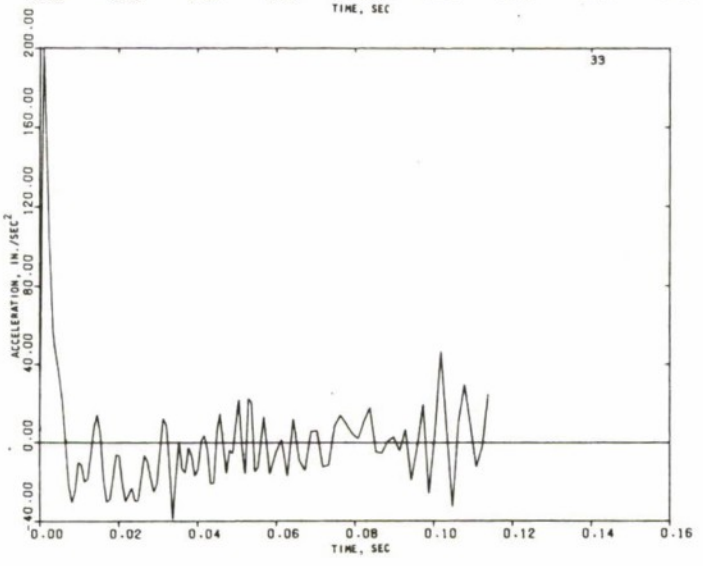

(c) ACCELERATION

FIGURE 5-15. MOTION TIME HISTORIES OF THE NORTH IGLOO (NODE 33)

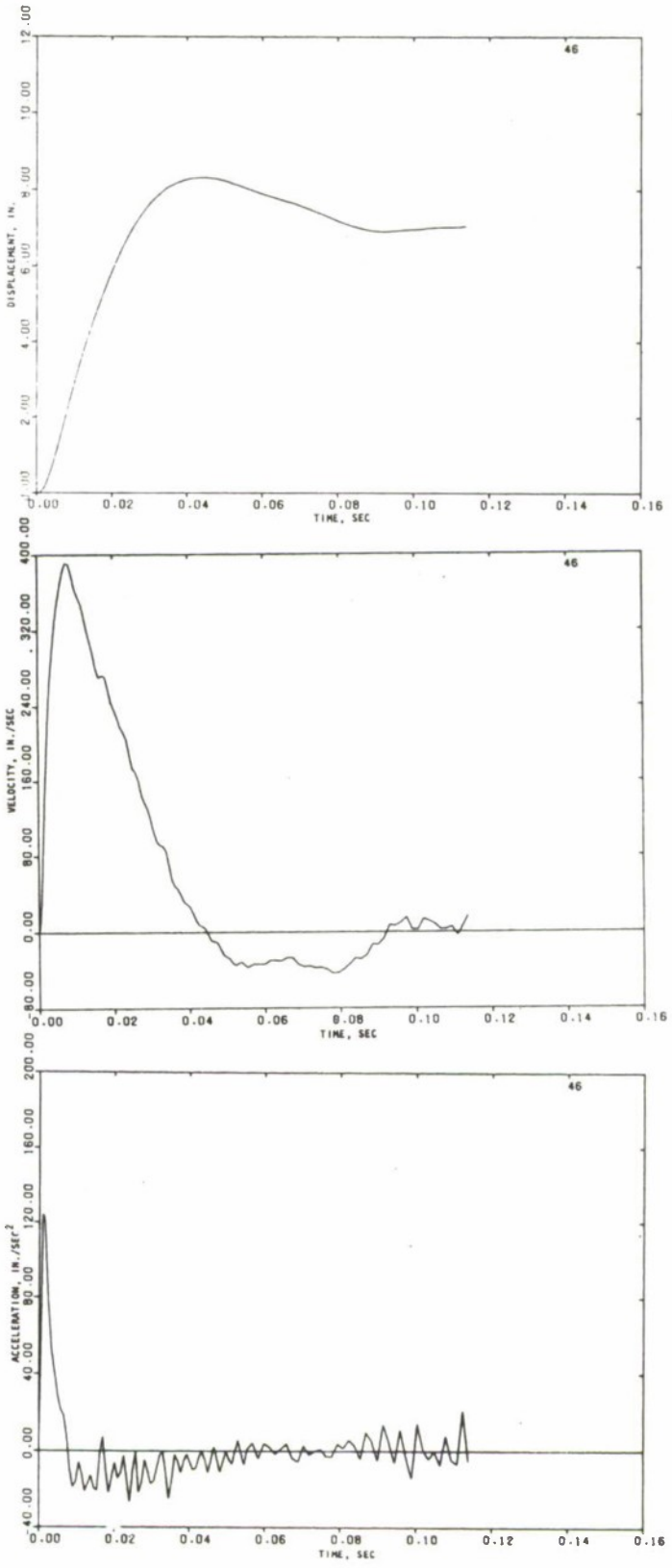

FIGURE 5-16. MOTION TIME HISTORIES OF THE NORTH IGLOO (NODE 46)

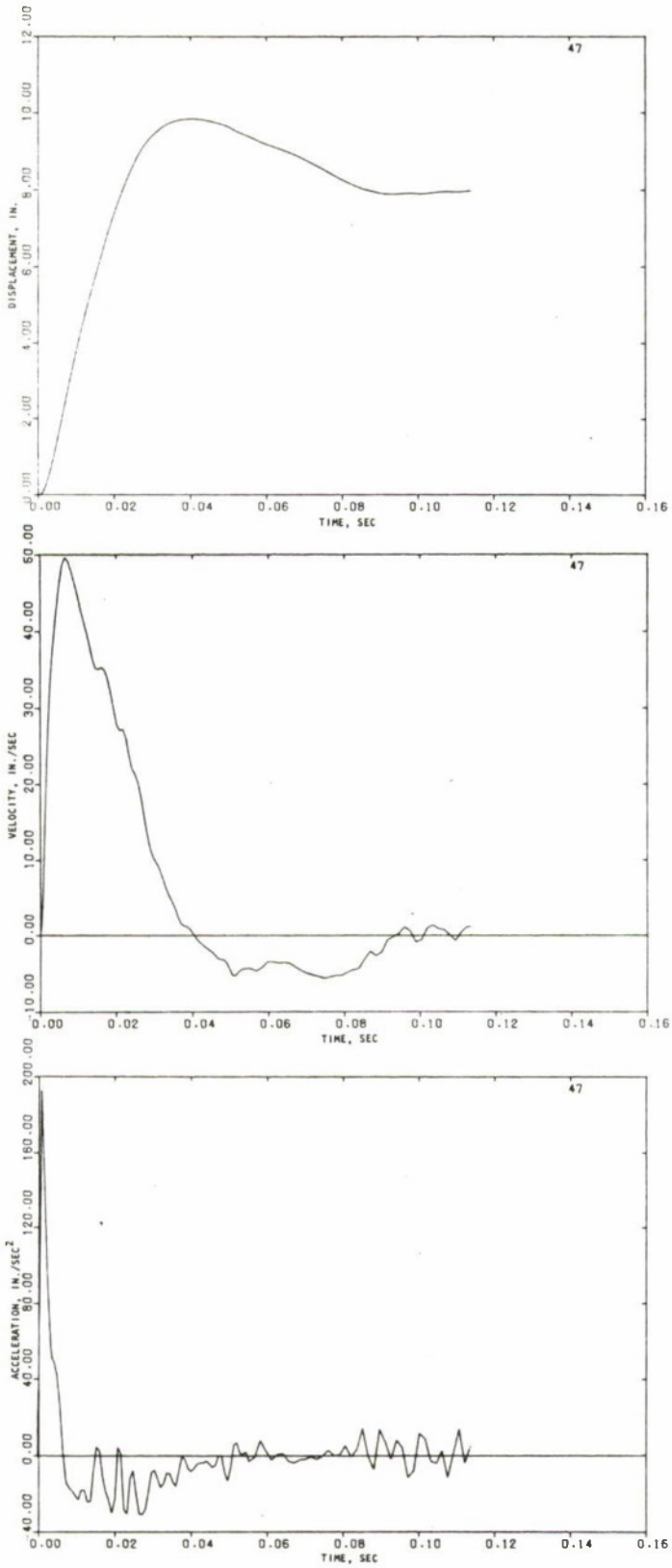

FIGURE 5-17. MOTION TIME HISTORIES OF THE NORTH IGLOO (NODE 47)

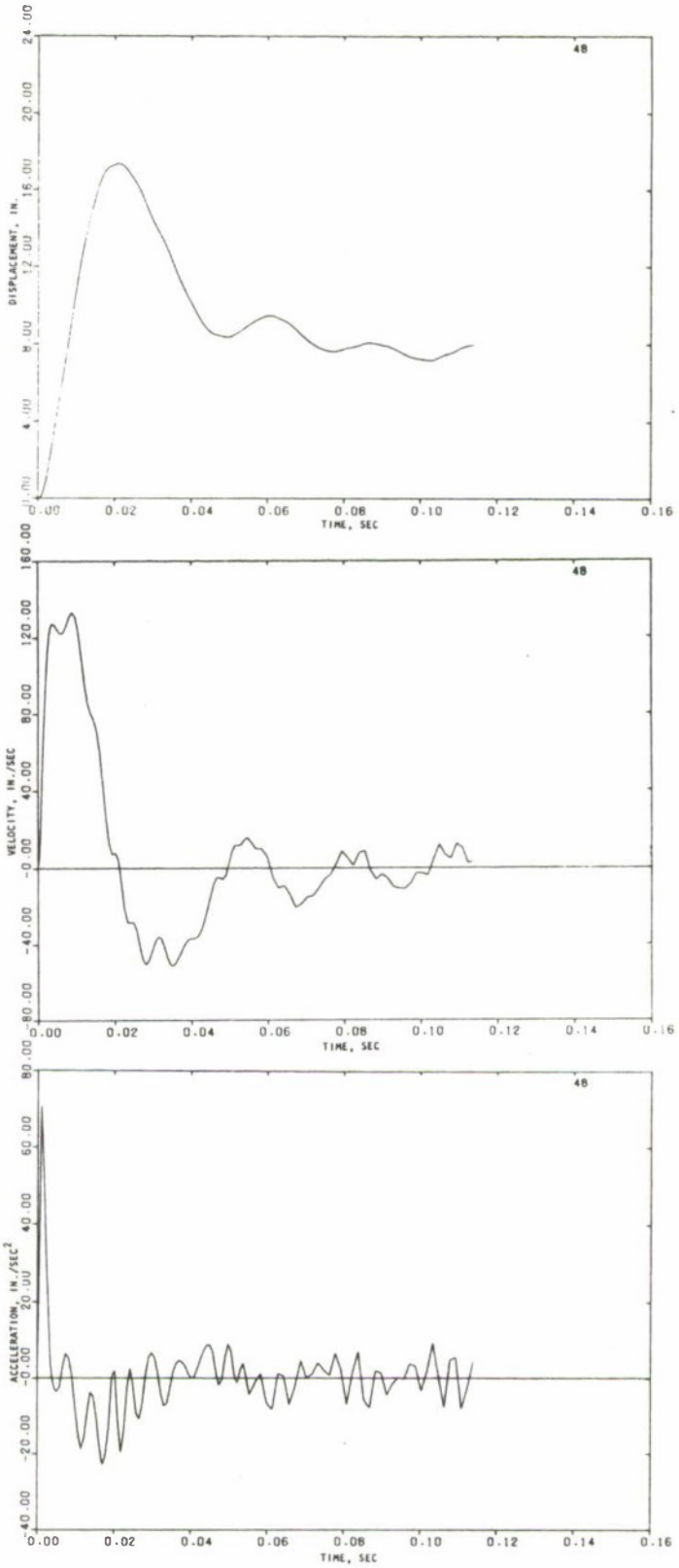

FIGURE 5-18. MOTION TIME HISTORIES OF THE NORTH IGLOO (NODE 48)

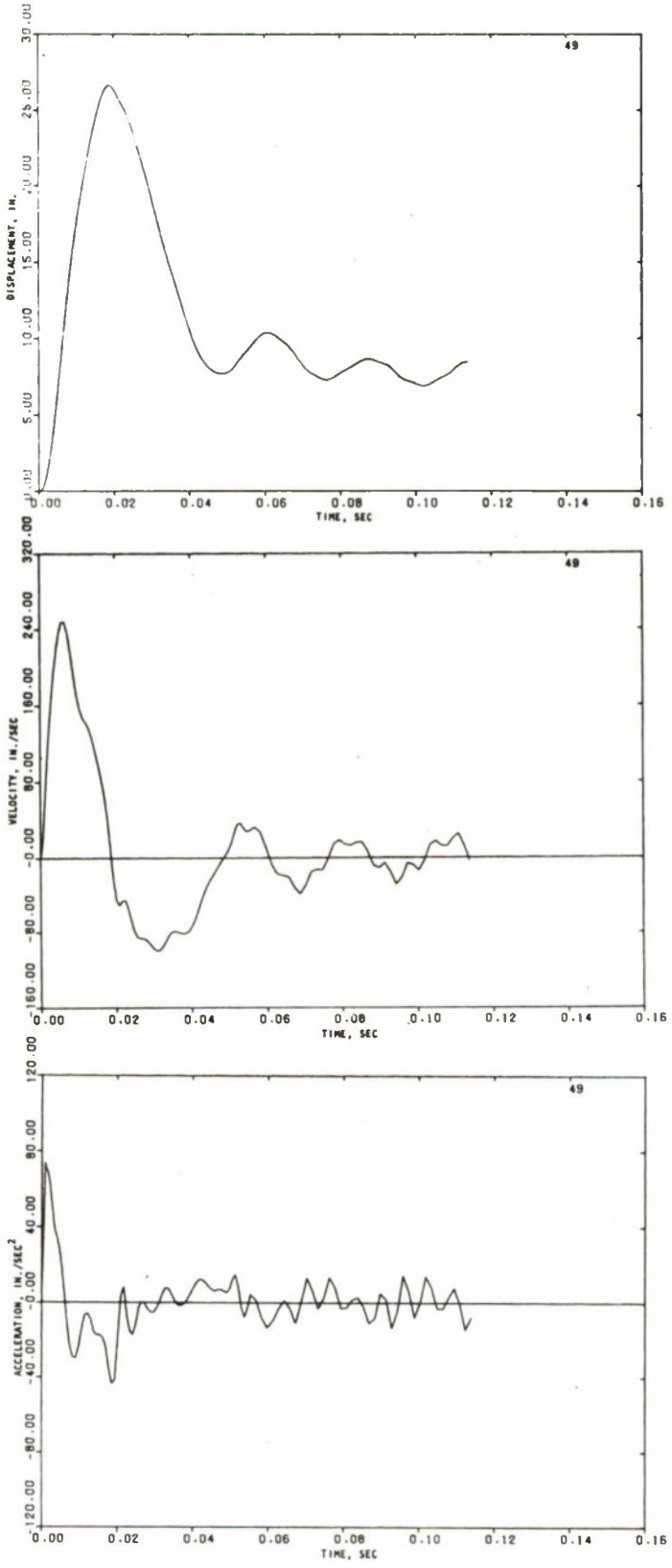

FIGURE 5-19. MOTION TIME HISTORIES OF THE NORTH IGLOO (NODE 49)

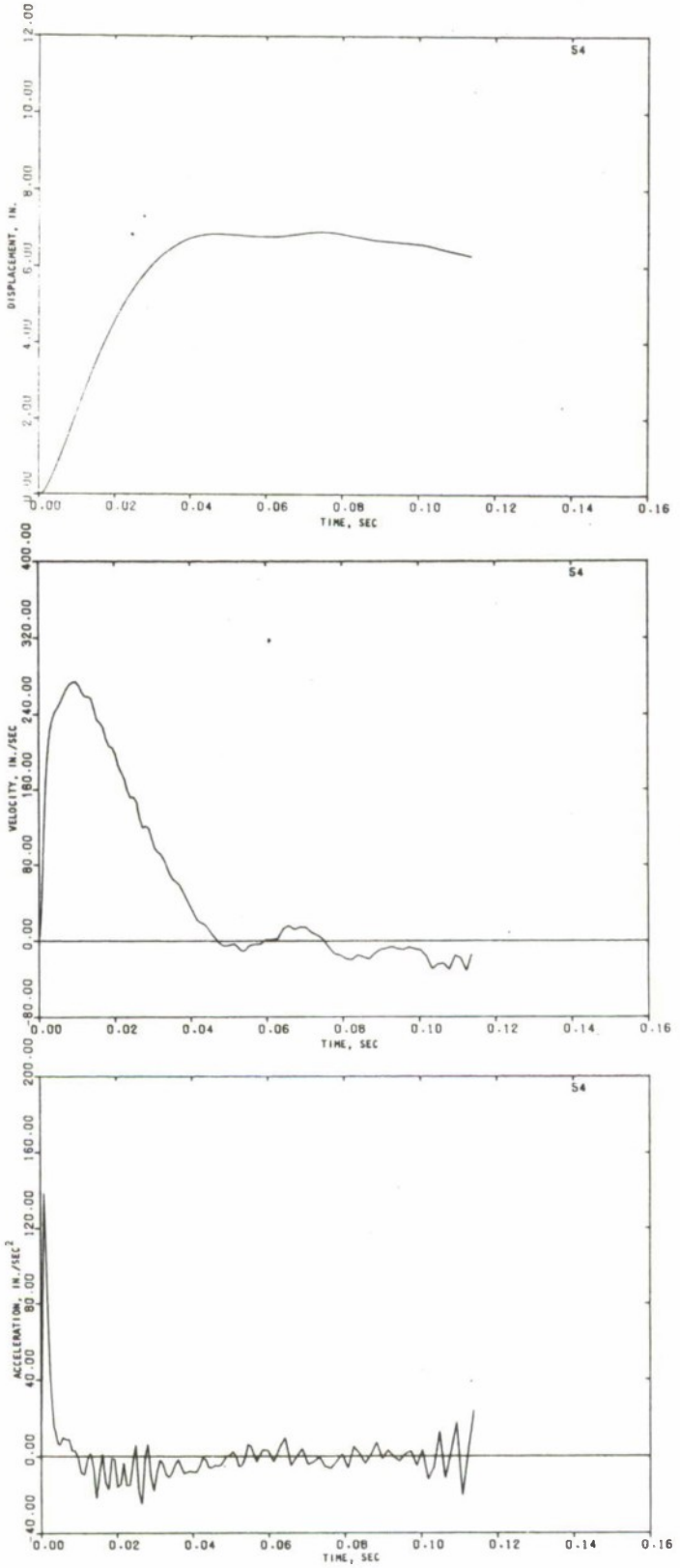

FIGURE 5-20. MOTION TIME HISTORIES OF THE NORTH IGLOO (NODE 54)

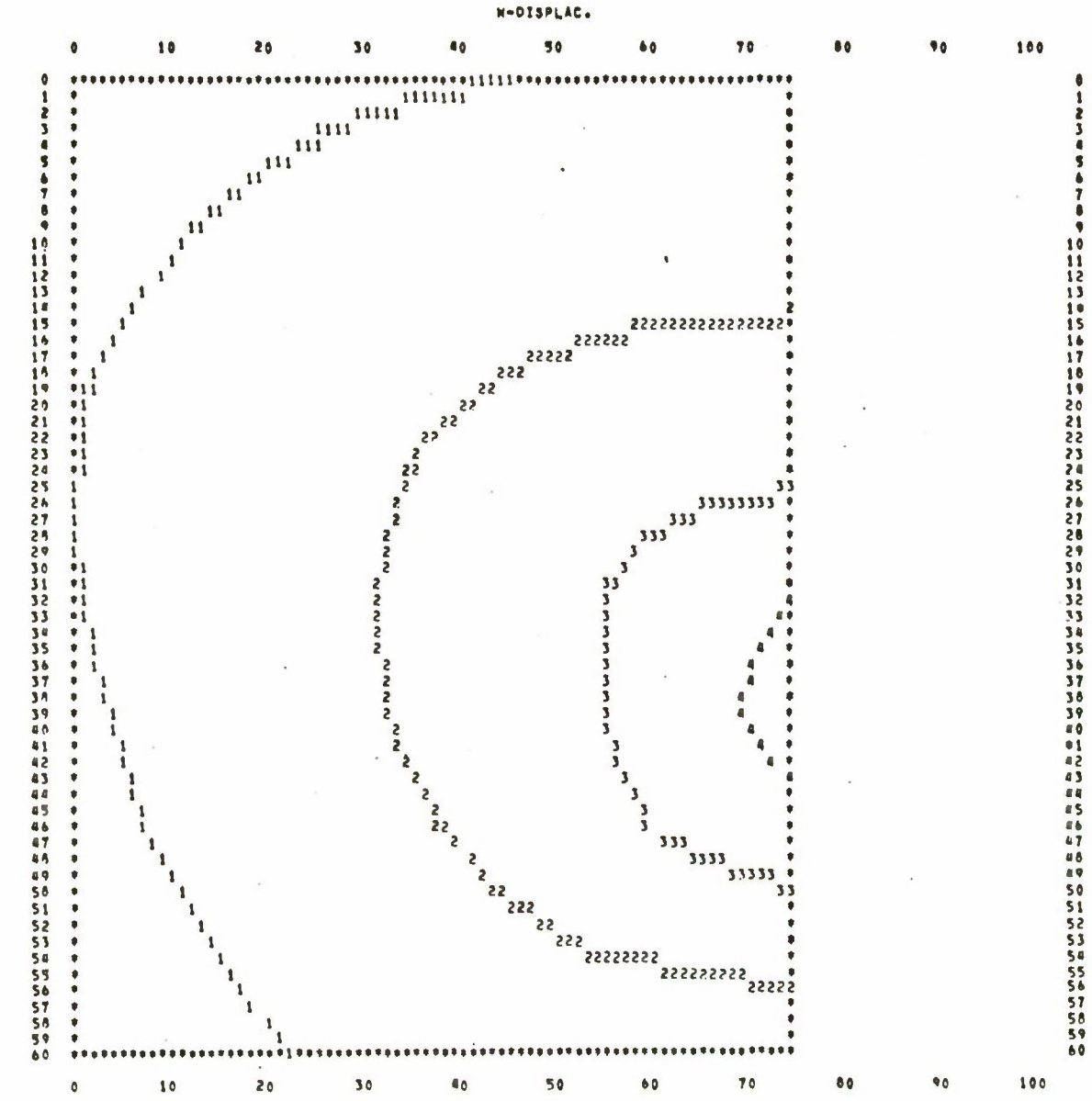

REFERENCES

LINE SYMBOL	VALUES	
0	.000000	.000000
1	2.000000	-2.000000
2	4.000000	-4.000000
3	6.000000	-6.000000
4	8.000000	-8.000000
5	10.000000	-10.000000
6	12.000000	-12.000000
7	14.000000	-14.000000
8	16.000000	-16.000000
9	18.000000	-18.000000
D	20.000000	-20.000000
*	BOUNDARY POINTS	

FIGURE 5-21. DISPLACEMENT CONTOUR PLOT OF SOUTH IGLOO AT t = 31.4 MSEC

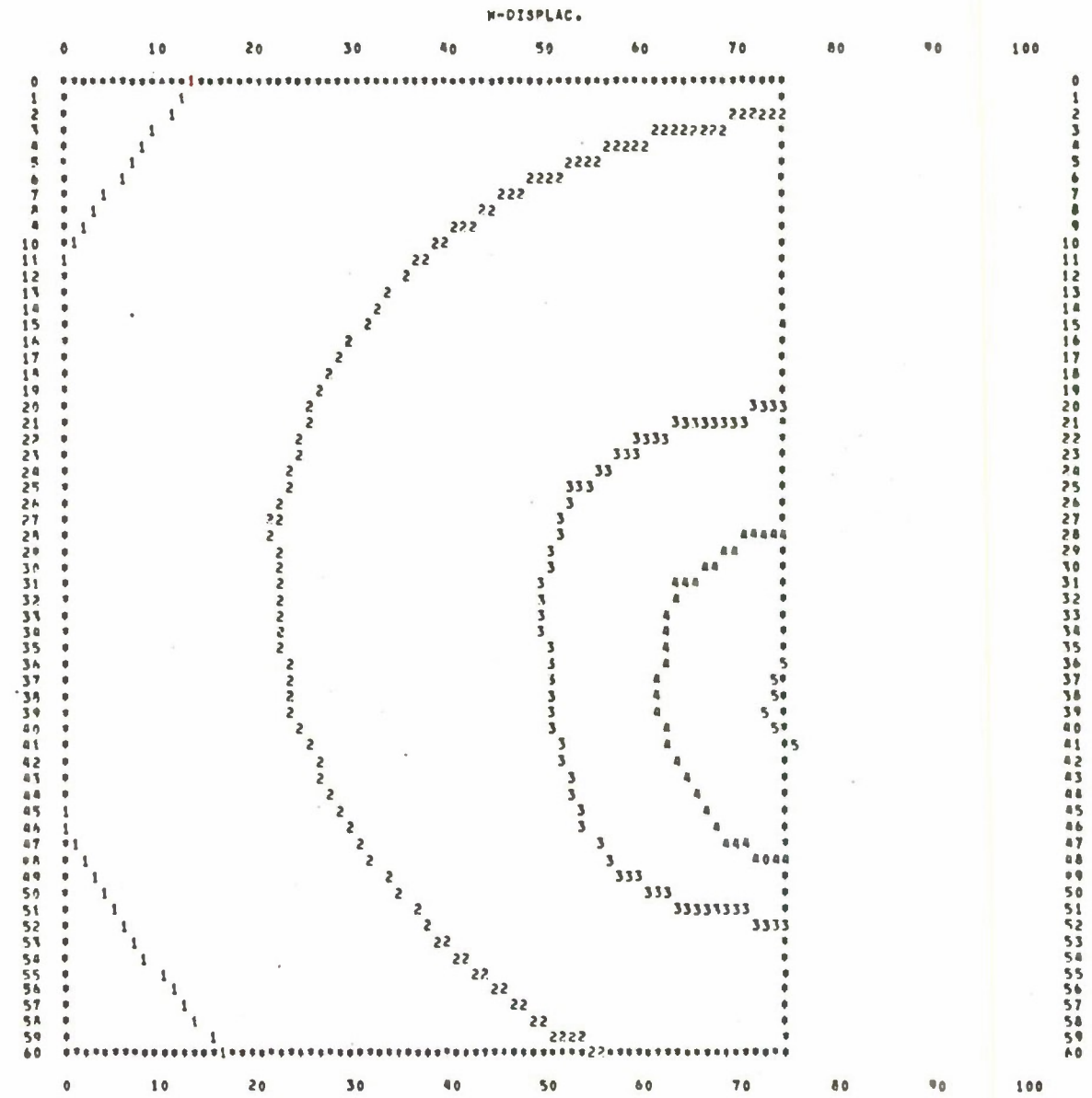

FIGURE 5-22. DISPLACEMENT CONTOUR PLOT OF SOUTH IGLOO AT t = 47.4 MSEC

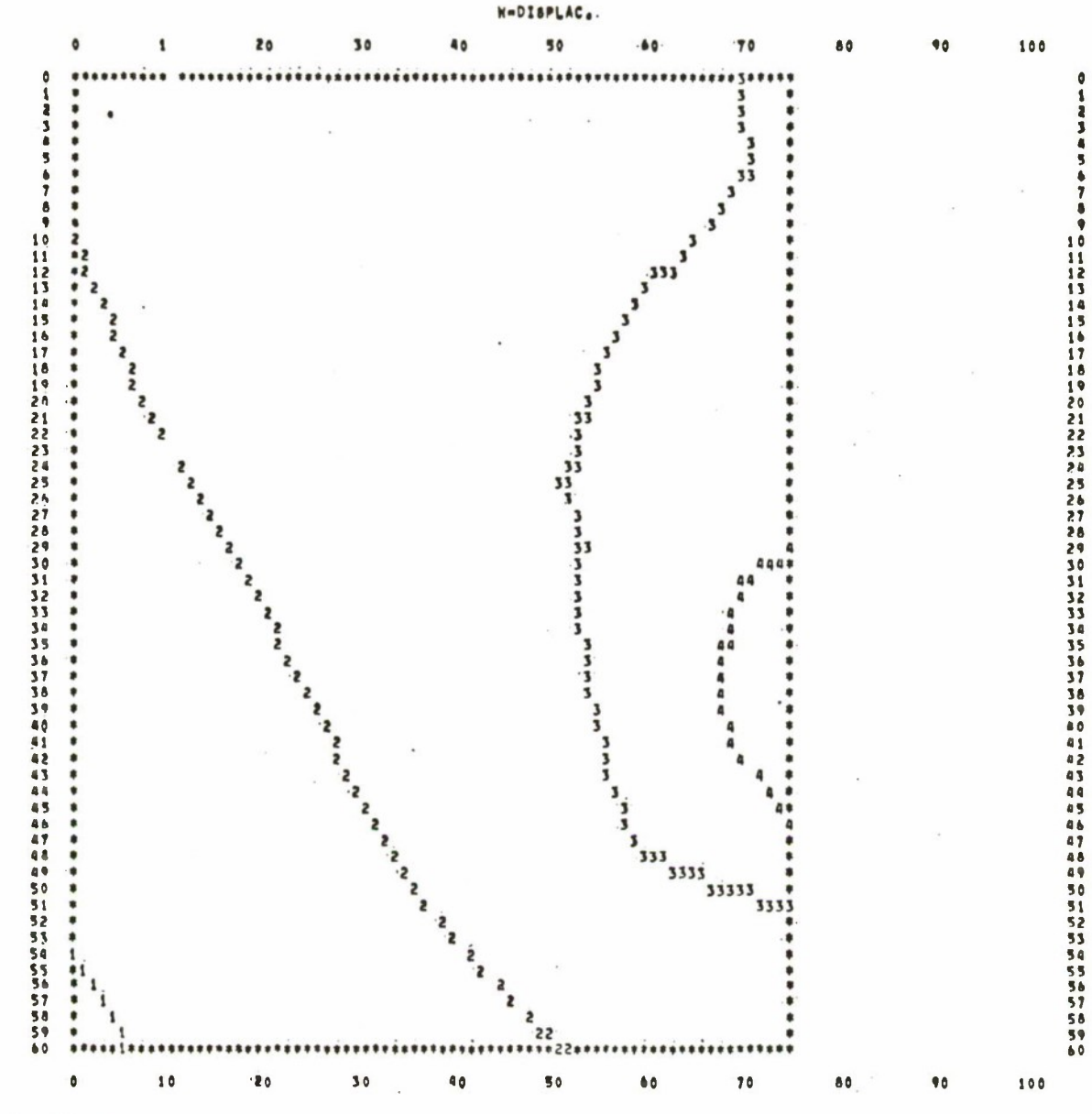

REFERENCES

LINE	SYMBOL	VALUES	
	0	.000000	.000000
	1	2.000000	-2.000000
	2	4.000000	-4.000000
	3	6.000000	-6.000000
	4	8.000000	-8.000000
	5	10.000000	-10.000000
	6	12.000000	-12.000000
	7	14.000000	-14.000000
	8	16.000000	-16.000000
	9	18.000000	-18.000000
	0	20.000000	-20.000000
	*	BOUNDARY POINTS	

FIGURE 5-23. DISPLACEMENT CONTOUR PLOT OF SOUTH IGLOO AT t = 116.4 MSEC

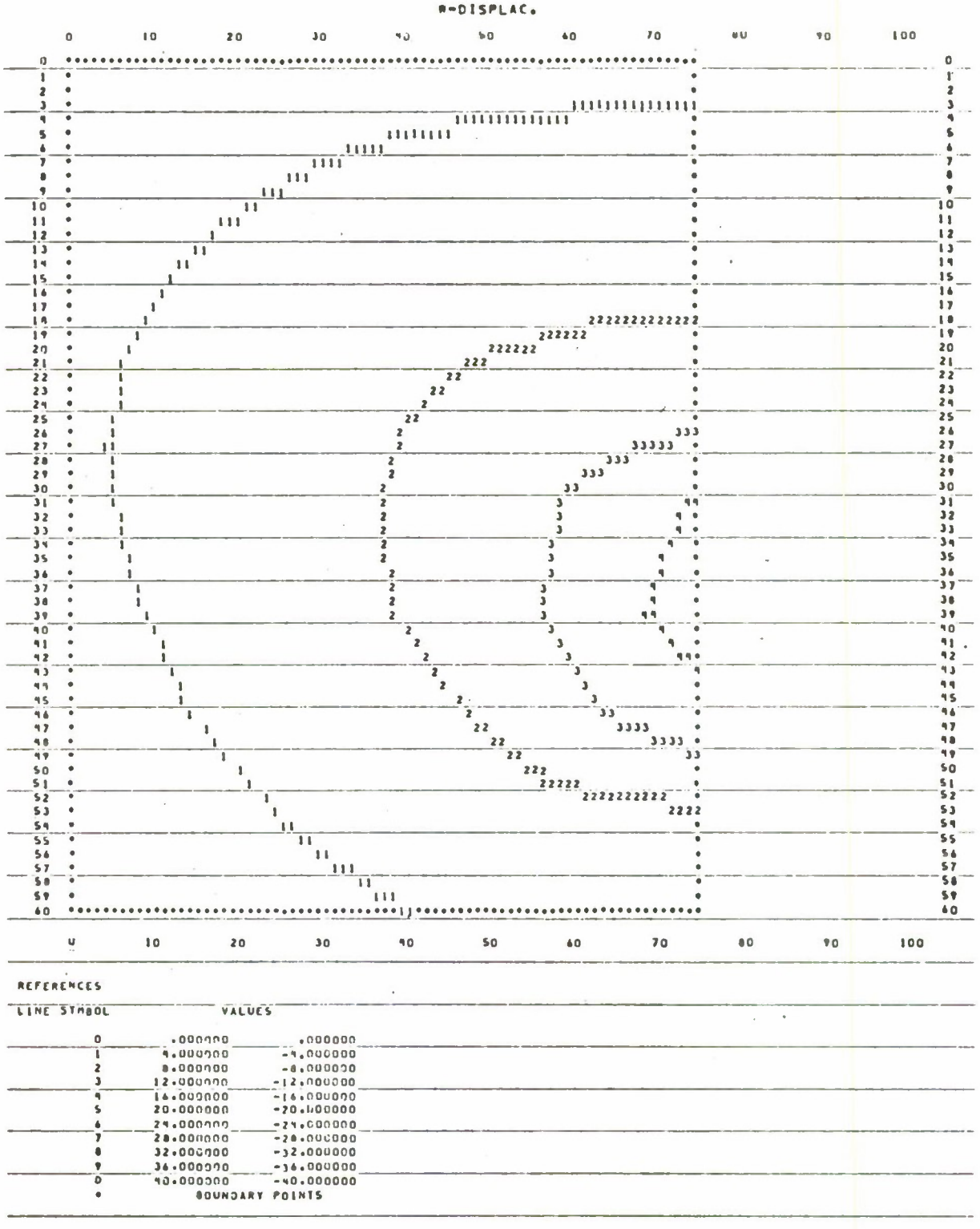

FIGURE 5-24. DISPLACEMENT CONTOUR PLOT OF NORTH IGLOO AT t = 31.4 MSEC

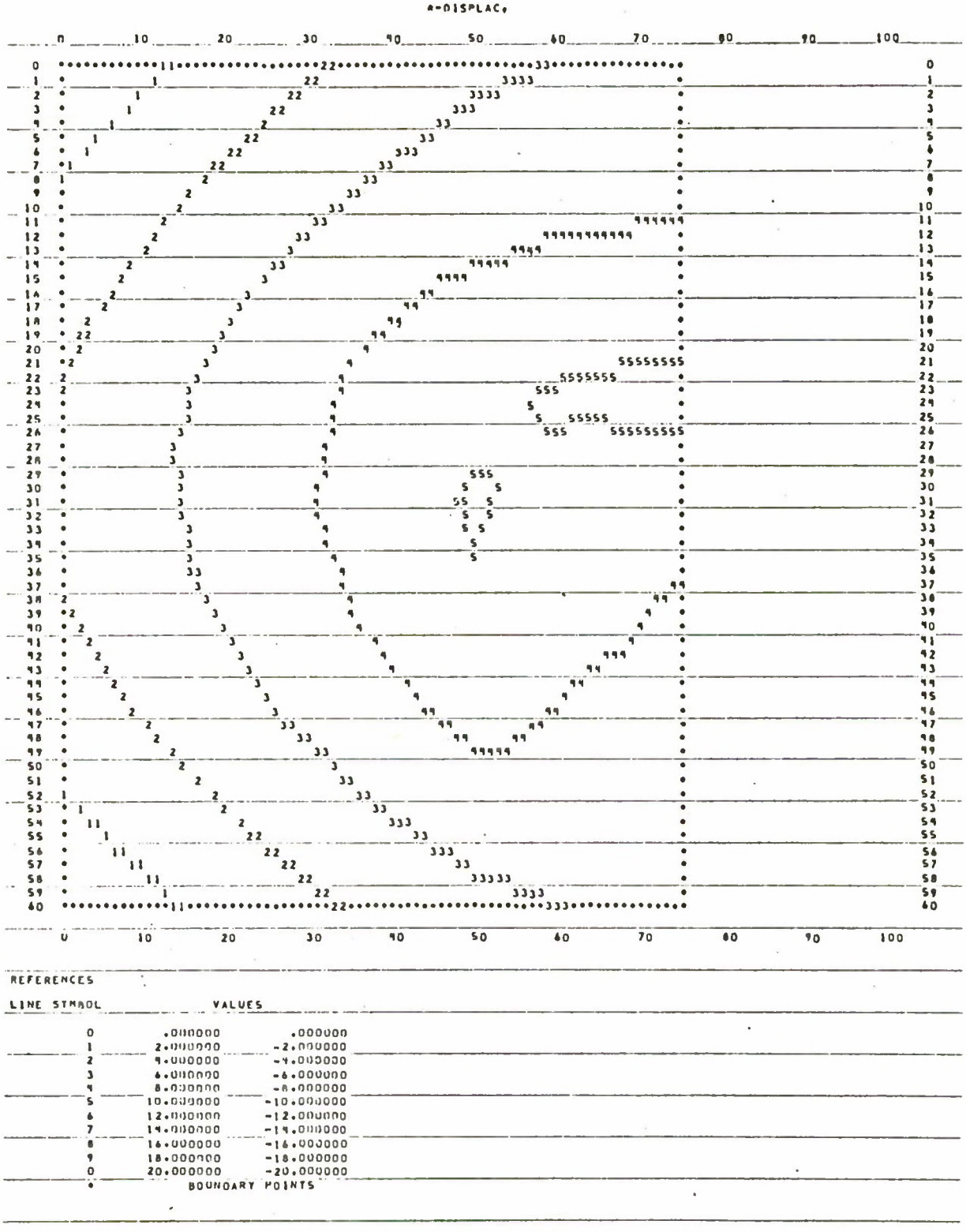

FIGURE 5-25. DISPLACEMENT CONTOUR PLOT OF NORTH IGLOO AT t = 47.4 MSEC

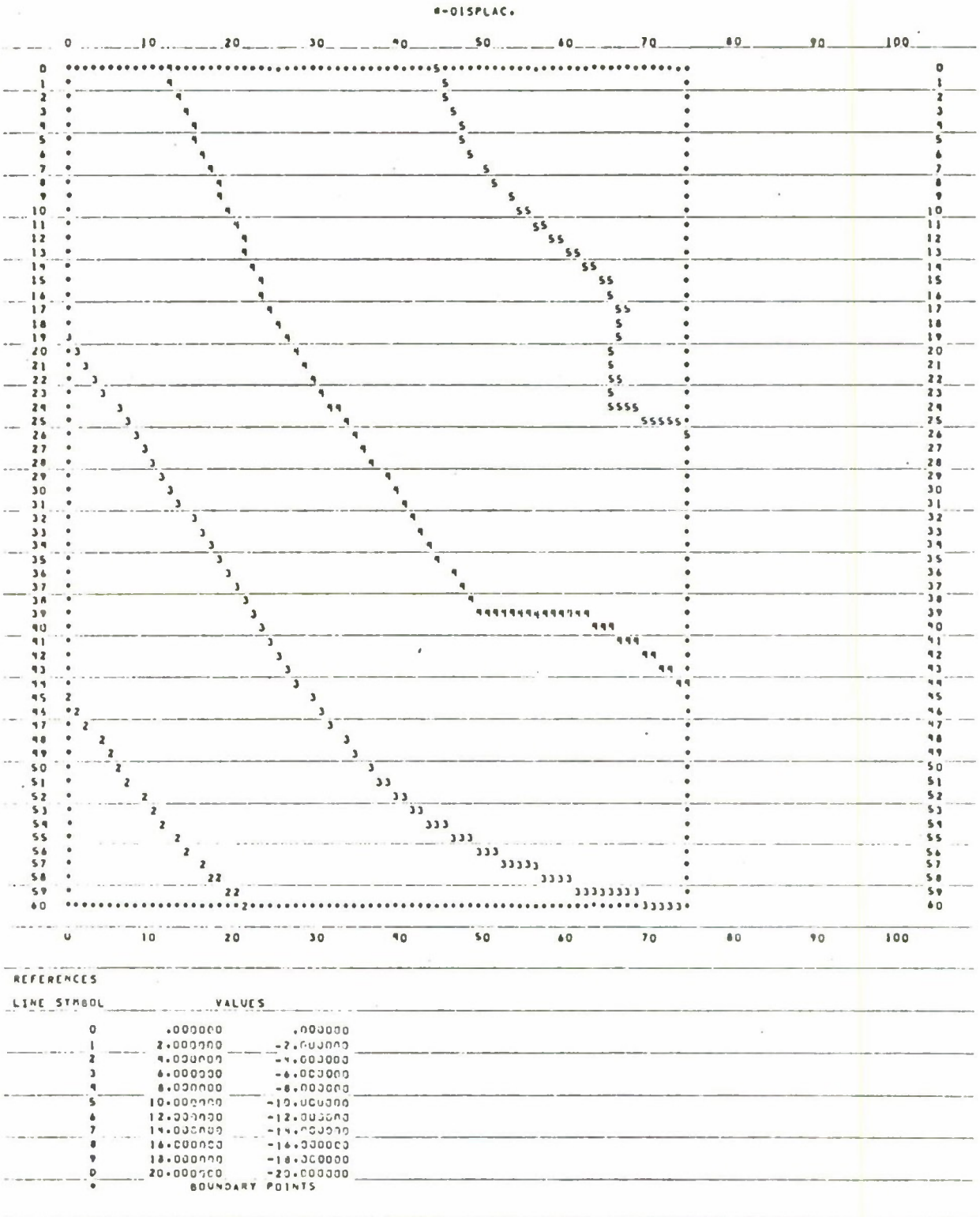

FIGURE 5-26. DISPLACEMENT CONTOUR PLOT OF NORTH IGLOO AT t = 115.4 MSEC

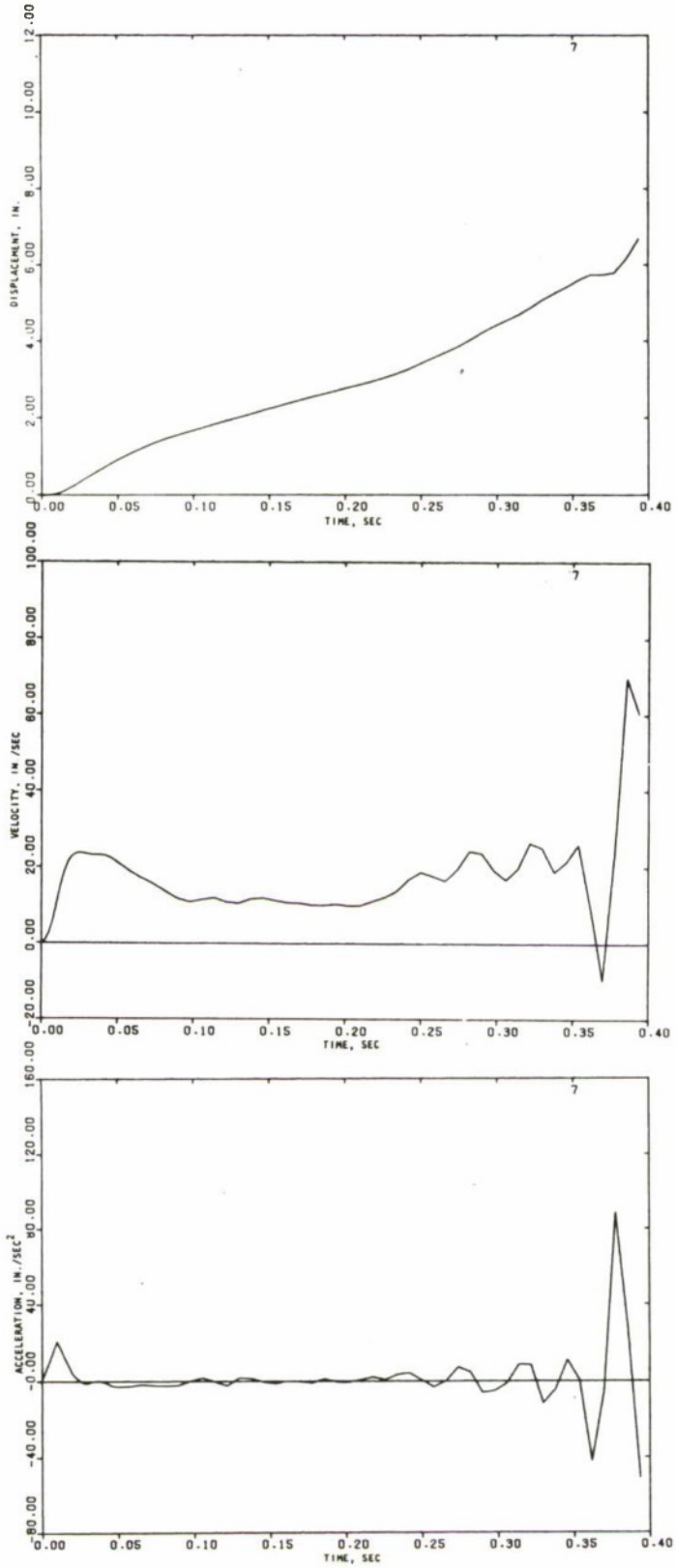

(a) DISPLACEMENT

(b) VELOCITY

(c) ACCELERATION

FIGURE 5-27. MOTION TIME HISTORIES OF THE EAST IGLOO (NODE 7)

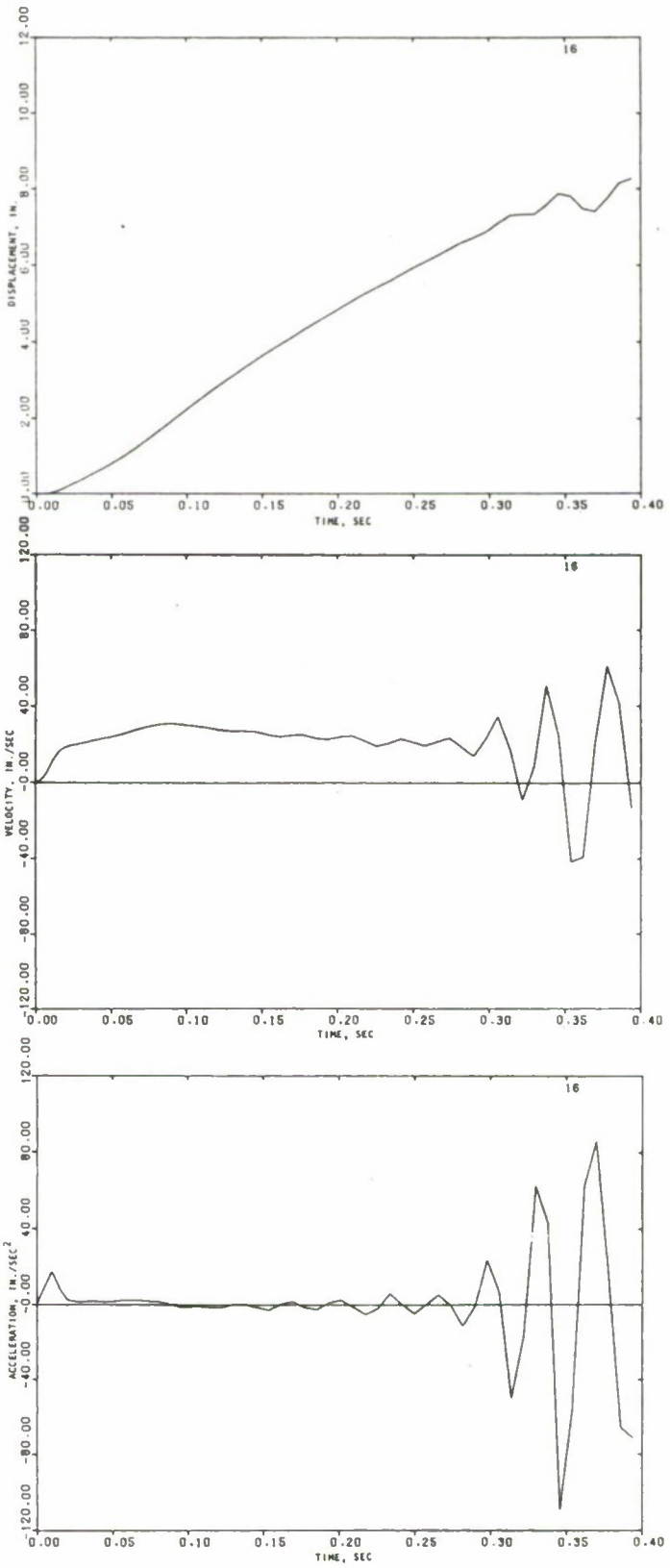

(a) DISPLACEMENT

(b) VELOCITY

(c) ACCELERATION

FIGURE 5-28. MOTION TIME HISTORIES OF THE EAST IGLOO (NODE 16)

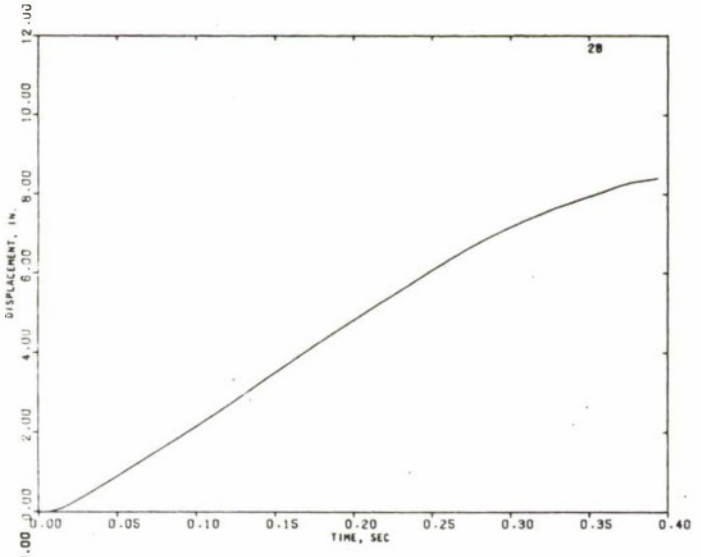

(a) DISPLACEMENT

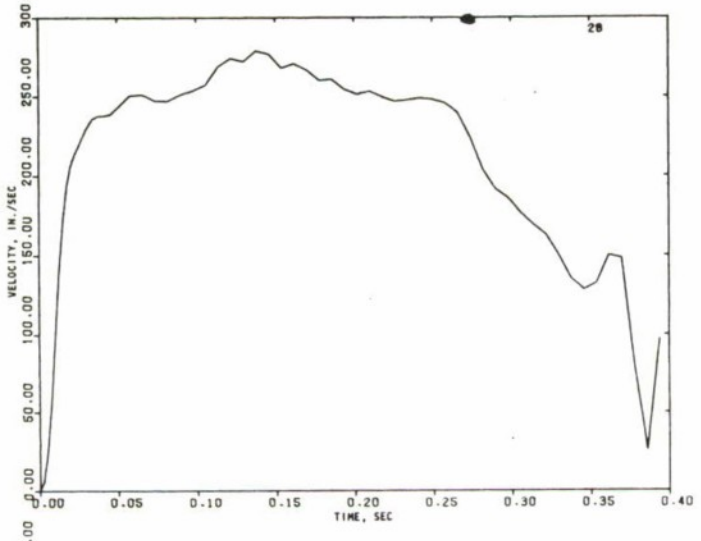

(b) VELOCITY

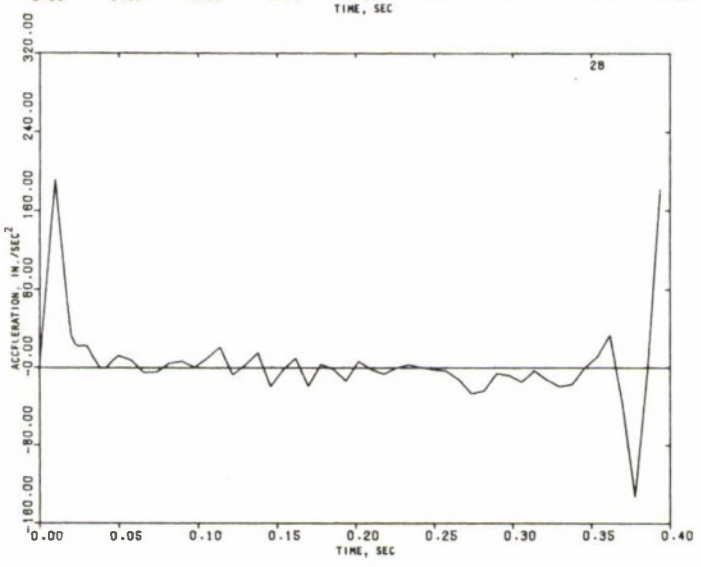

(c) ACCELERATION

FIGURE 5-29. MOTION TIME HISTORIES OF THE EAST IGLOO (NODE 28)

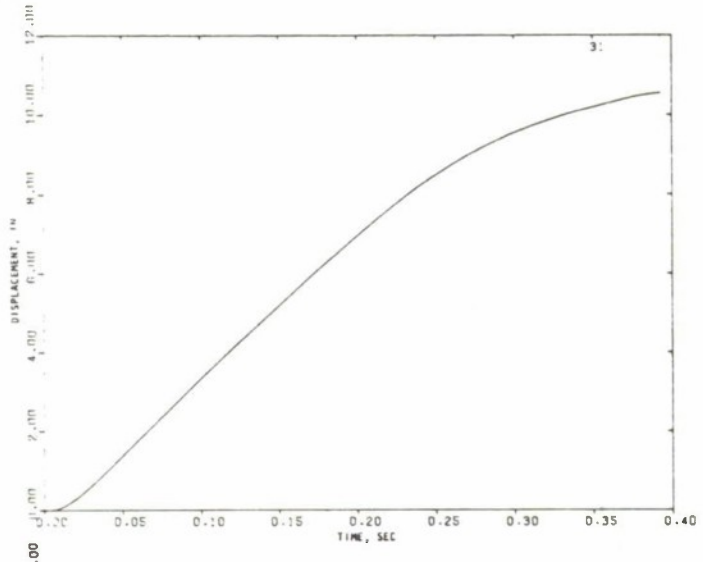

(a) DISPLACEMENT

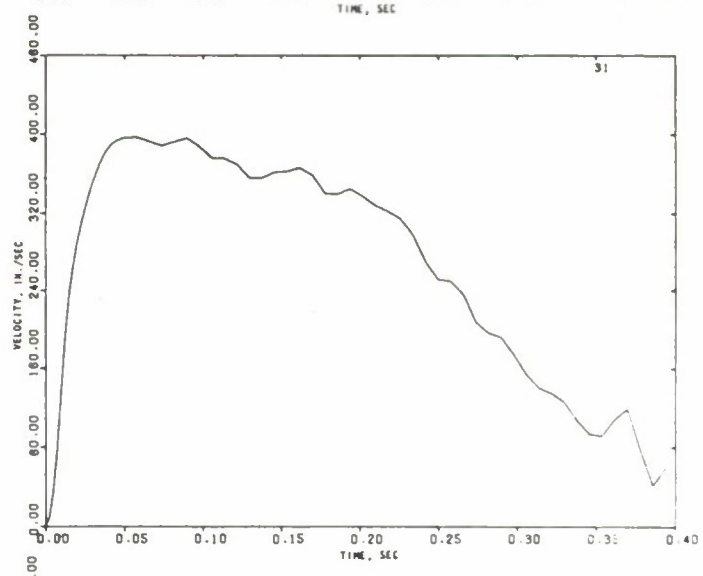

(b) VELOCITY

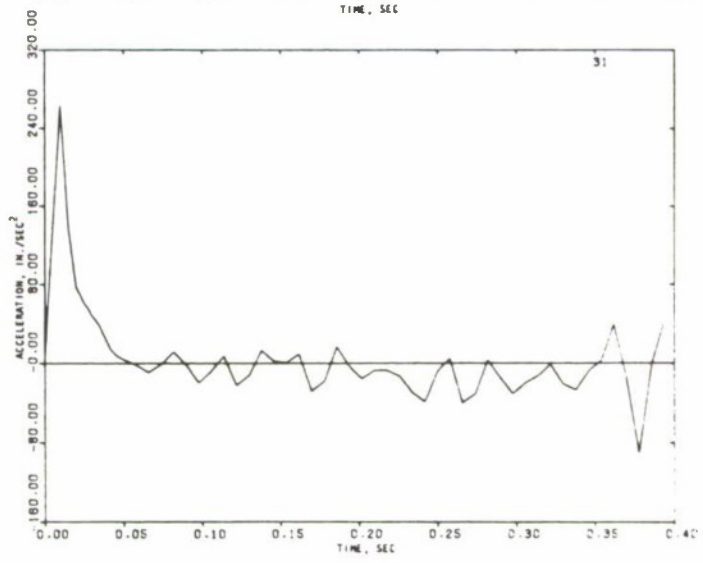

(c) ACCELERATION

FIGURE 5-30. MOTION TIME HISTORIES OF THE EAST IGLOO (NODE 31)

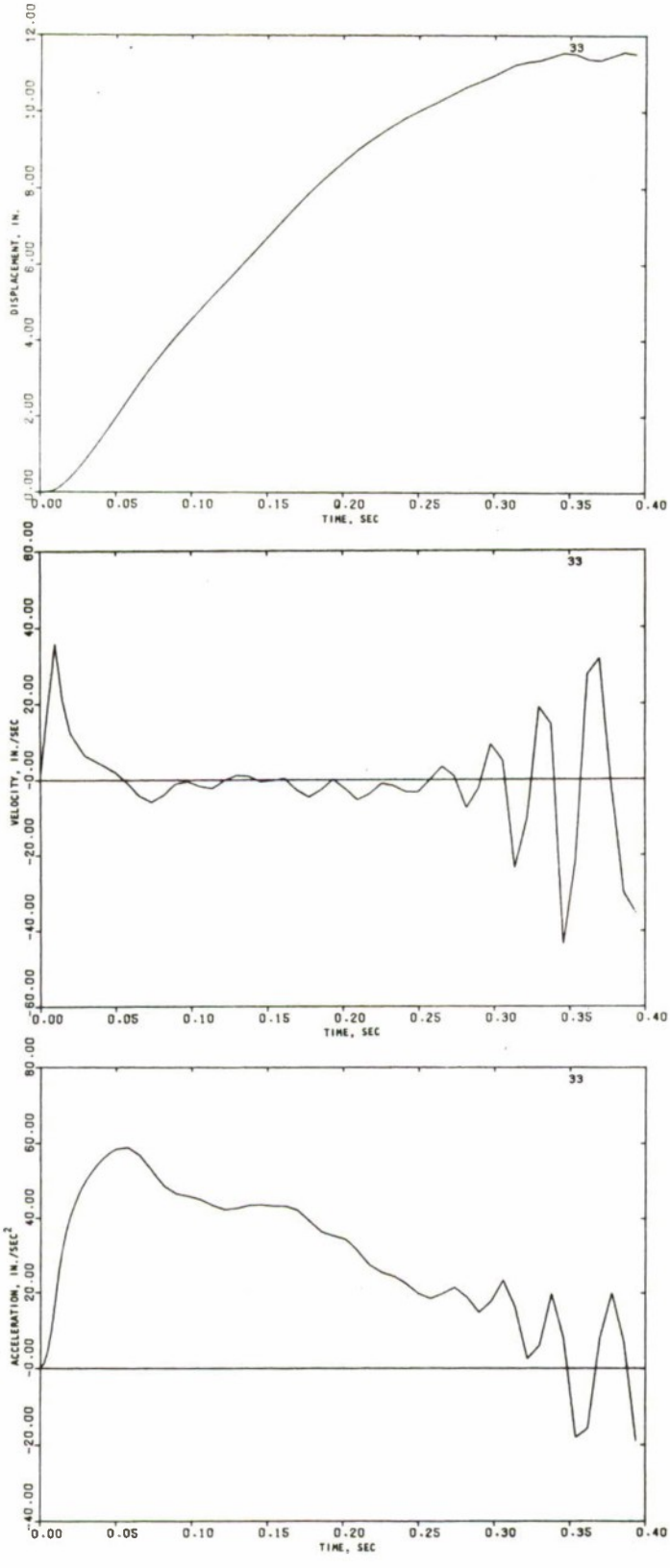

(a) DISPLACEMENT

(b) VELOCITY

(c) ACCELERATION

FIGURE 5-31. MOTION TIME HISTORIES OF THE EAST IGLOO (NODE 33)

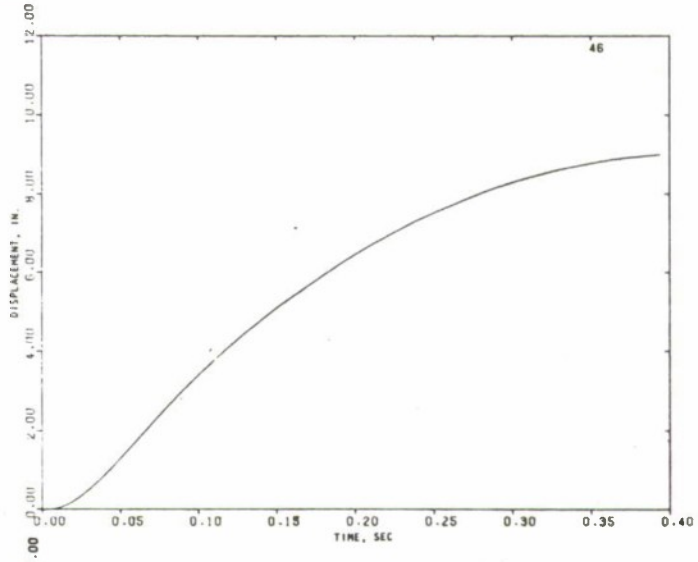

(a) DISPLACEMENT

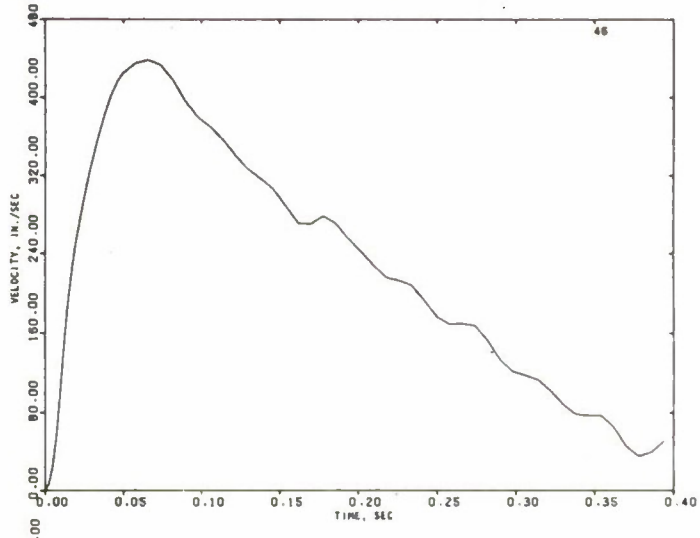

(b) VELOCITY

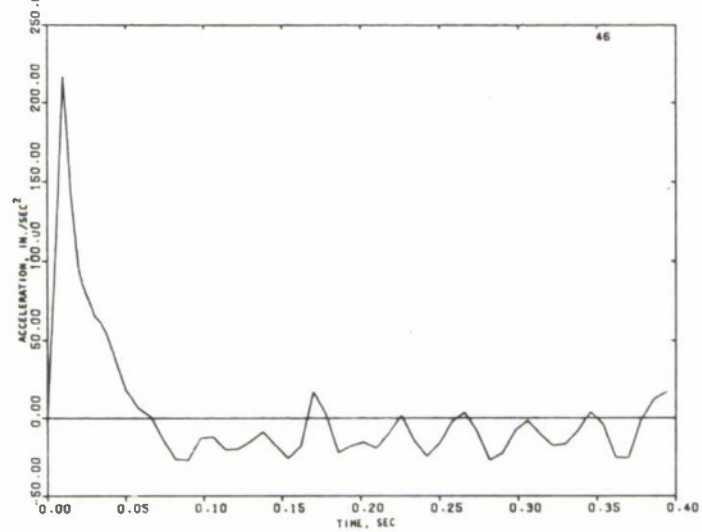

(c) ACCELERATION

FIGURE 5-32. MOTION TIME HISTORIES OF THE EAST IGLOO (NODE 46)

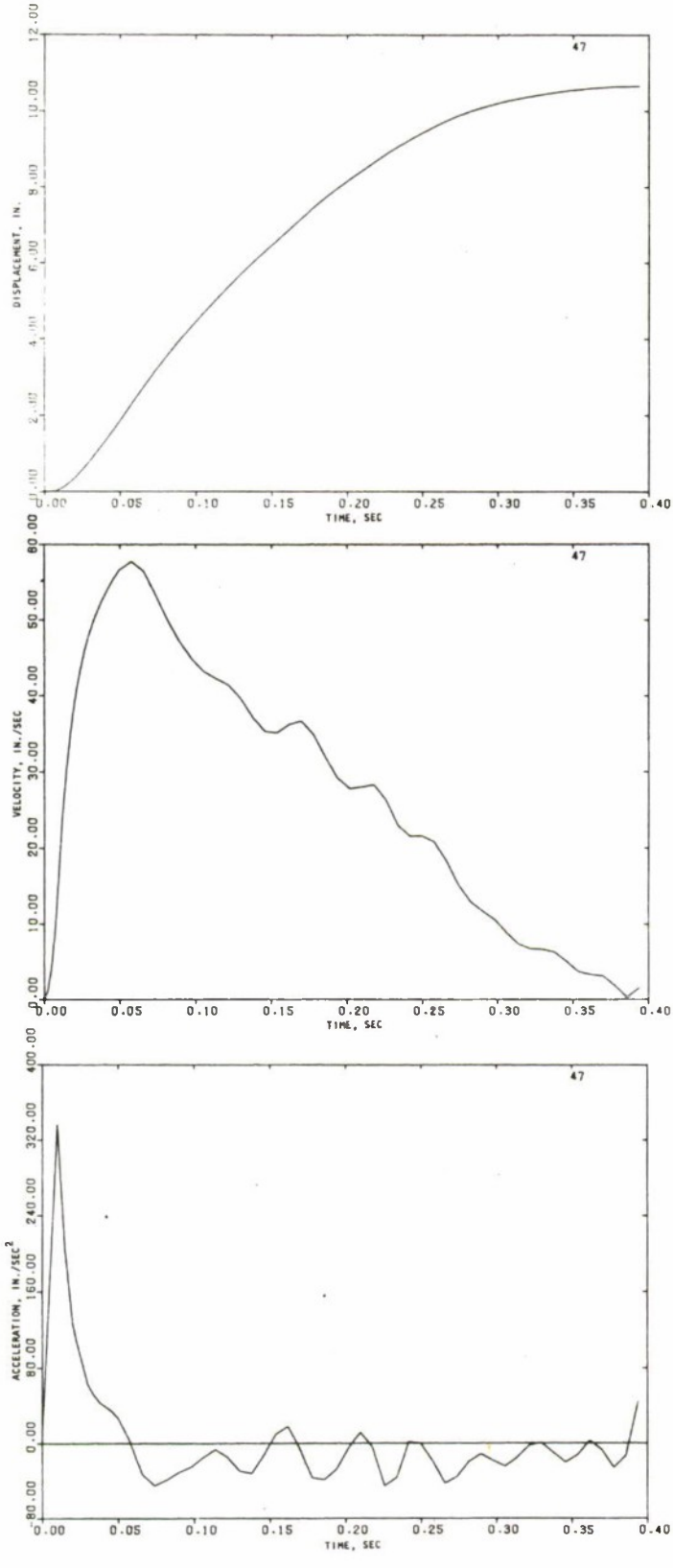

(a) DISPLACEMENT

(b) VELOCITY

(c) ACCELERATION

FIGURE 5-33. MOTION TIME HISTORIES OF THE EAST IGLOO (NODE 47)

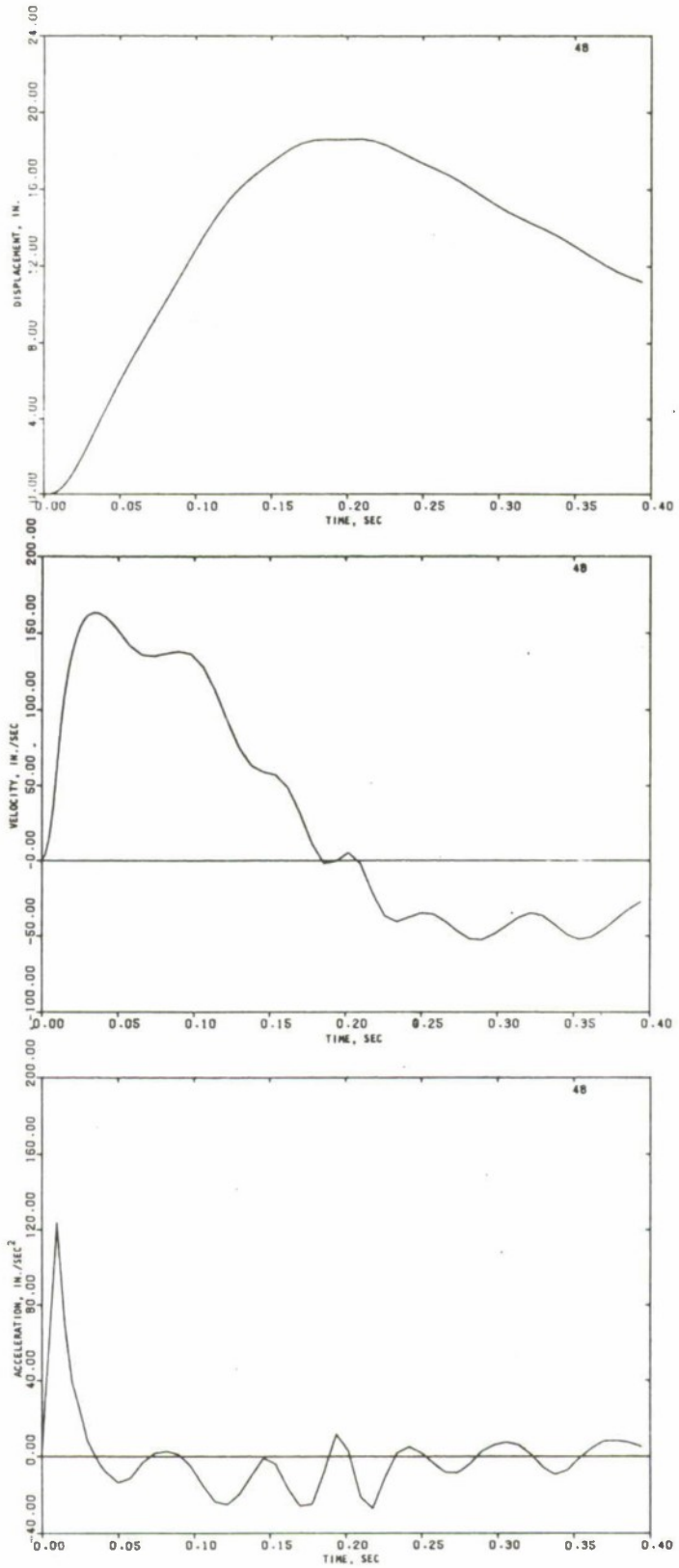

(a) DISPLACEMENT

(b) VELOCITY

(c) ACCELERATION

FIGURE 5-34. MOTION TIME HISTORIES OF THE EAST IGLOO (NODE 48)

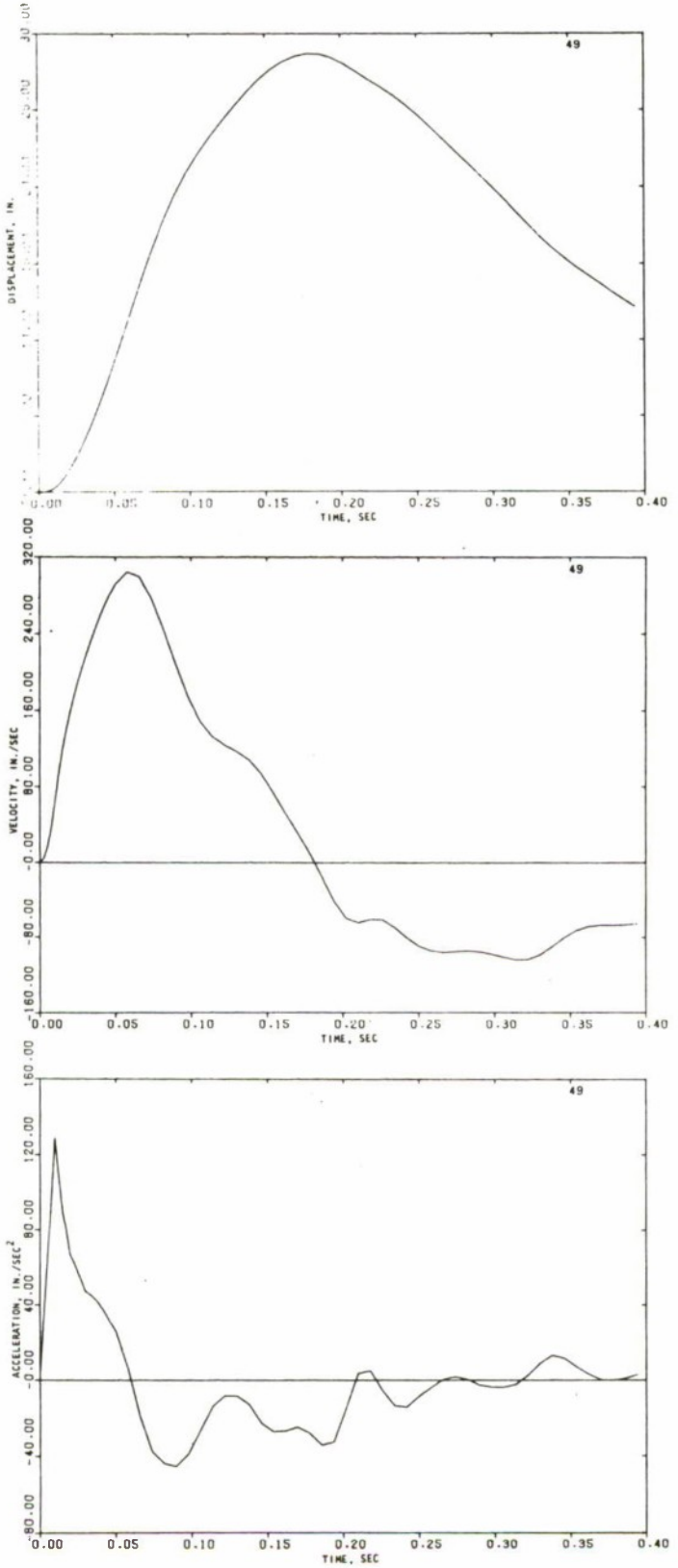

(a) DISPLACEMENT

(b) VELOCITY

(c) ACCELERATION

FIGURE 5-35. MOTION TIME HISTORIES OF THE EAST IGLOO (NODE 49)

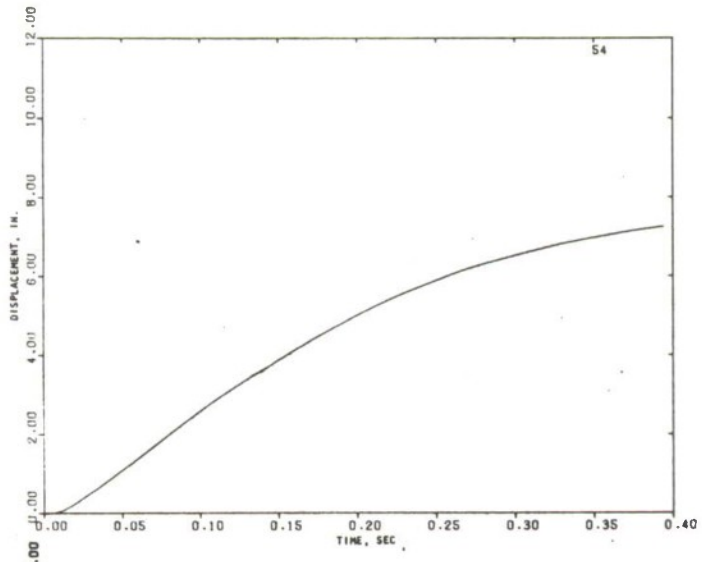

(a) DISPLACEMENT

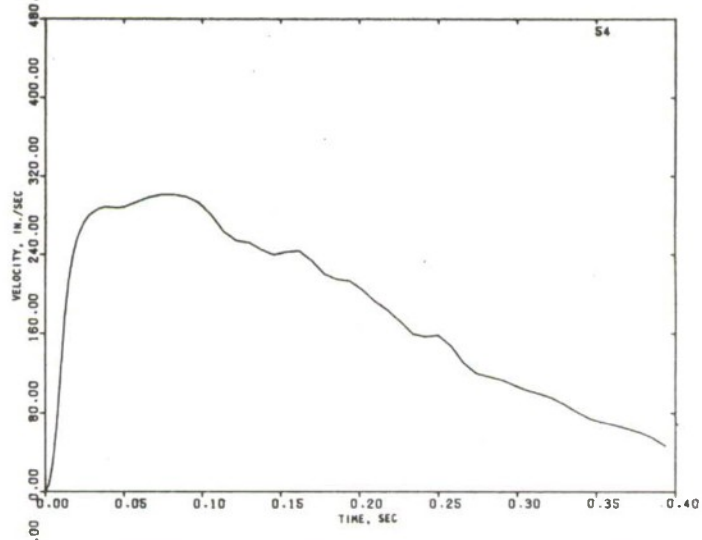

(b) VELOCITY

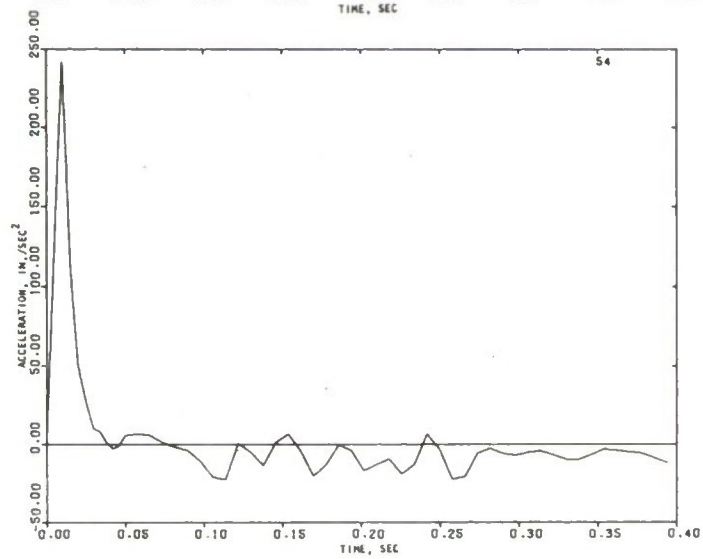

(c) ACCELERATION

FIGURE 5-36. MOTION TIME HISTORIES OF THE EAST IGLOO (NODE 54)

BLANK

SECTION 6

COMPARISON OF MATHEMATICAL COMPUTATIONS AND FIELD MEASUREMENTS

There are two sources of measured data available for the Eskimo I Magazine Separation Test. One is the Naval Weapons Center report of Reference 1 and the other is the movie taken inside the igloos, which was made available to AA by the Department of Defense Explosives Safety Board. Both sources of information are very limited, and the measurements of the maximum response and permanent deflections of the headwall are not expected to be very accurate. On the other hand, any attempt to use a limited number of individual elements to represent a complicated structural system requires that certain approximations be made. As a consequence of using these approximations, some structural details will inevitably be lost. Therefore, the adequacy of the mathematical model for predicting the responses depends to some extent on the engineering experience and judgment of the engineer/analyst.

6.1 ESKIMO I MAGAZINE SEPARATION TEST

In this section, the data from the measurements of the structural motion of the igloos in response to the explosion (as reported in Reference 1) are compared with the corresponding results from the finite element calculations, reported in detail in the previous sections. The measured data that are available for comparison purposes are linear motion transducer data, accelerometer data, and static headwall measurements.

6.1.1 LINEAR MOTION TRANSDUCER DATA

The linear motion transducers are positioned above the center of the igloo doorways to measure movement of the concrete headwalls of the north, east, and south igloos. The motion values listed in Table 6-1 were derived from the recorded data. Listed in Table 6-2 are the corresponding values obtained from the finite element calculations. These values were taken at node 33 (Figure 3-2), which corresponds to the actual point on the headwall where measurements were recorded.

TABLE 6-1. SUMMARY OF LINEAR MOTION TRANSDUCER DATA

Location of Headwall Transducer	Max. Velocity, ft/sec	Av. Velocity from Initial Motion to Peak Excursion, ft/sec	Time from Initial Motion to Max. Velocity, ms	Av. Acceleration from Initial Motion to Max. Velocity, g
North Igloo	29.8	20.0	8.1	114
East Igloo	29.5	18.5	8.0	114
South Igloo	27.9	13.3	14.4	60

TABLE 6-2. MOTION VALUES FROM THE MATHEMATICAL MODEL

Headwall	Max. Velocity, ft/sec	Av. Velocity from Initial Motion to Peak Excursion, ft/sec	Time from Initial Motion to Max. Velocity, ms	Av. Acceleration from Initial Motion to Max. Velocity, g
North Igloo	42.2	28.3	6.8	259
East Igloo	49.1	36.5	5.8	285
South Igloo	20	11.7	11.2	64.8

A direct comparison of Tables 6-1 and 6-2 shows that the only agreement between them appears to be in the average acceleration of the south igloo (60 vs. 64.8). The ratio of the computed to the measured accelerations is found to be 2.5 for the east igloo and 2.27 for the north igloo. Since the peak acceleration is closely related to the peak input pressure, the ratio of the model to the measured peak inputs are evaluated. These ratios, based on the data listed in Table 2-1, are: 0.99 (75/76) for the south igloo, 1.26 (300/238) for the north igloo, and 2.1 (525/250) for the east igloo. Thus, it seems that there is better agreement between the ratios of peak inputs and the ratios of peak accelerations. It is not intended here to imply that the acceleration responses are directly proportional to the peak pressures but to indicate that better agreement can be achieved if the measured pressures are used as input to the headwall model.

Since the pressure history input disappears well before any large structural motions occur, the average velocity responses are approximately proportional to the total accumulated impulses from the initiation of motion to the maximum velocity. Because the pressure histories are approximately triangular in shape (Figures 2-1 through 2-3) the total impulses can be considered to be proportional to the peak pressures. Therefore, the average velocities are, in turn, proportional to peak pressures. The ratios of the computed to the measured results are summarized in Table 6-3.

TABLE 6-3. RATIOS OF THE ANALYTICAL AND THE MEASURED RESULTS

Headwall	Peak Pressure	Average Acceleration	Average Velocity	Maximum Velocity
North Igloo	1.26	2.27	1.41	1.41
East Igloo	2.10	2.50	1.98	1.66
South Igloo	0.99	1.08	0.88	0.72

The ratios presented in Table 6-3 and discussed previously indicate that the calculated responses for the south igloo are in good agreement with the measured data. The development in Section 2 revealed that the theoretically predicted pressure input data were higher than the measured data for north and east igloos. As a consequence, the predicted responses for the north and east igloos are also higher.

6.1.2 STATIC HEADWALL MEASUREMENT

The static headwall measurements involved setting up survey monuments 3 ft in front of the igloo headwalls. The distances from the monuments to the headwalls were measured at selected points before the test. These distances were again measured after the test. The net changes in displacements represented the permanent settlements of the headwalls. A gap of approximately 0.2 ft was found between the back of the south headwall and the earth cover at the top left corner, and a similar space 0.1 ft wide was found at the top right corner. This demonstrates that the static measurements are not the maximum displacements but are the permanent movements of the headwall. These permanent displacements of the headwalls are shown in Figures 6-1 through 6-3 (Reference 1). All the measurements are subject to $\pm$0.05 ft of error because pretest measurements showed that the walls deviated from a true vertical plane by that amount. The measured displacement patterns indicate that the headwalls appear to have responded in different ways. More pronounced yielding on the steel arch was found in the south igloo. In the west igloo, there was clear indication that the steel arch acted as a reaction line resisting headwall movement. The difference in the observed data, therefore, implies that material properties in the two igloos are not the same. As was mentioned before, the finite element models used to predict the responses of the south and west igloos are identical. The assumed material properties of the model would therefore seem to represent characteristics that are a compromise between the actual properties of the south igloo and those of the west igloos.

The predicted permanent displacement contours from the calculations for the south igloo were selected at the end of the numerical computation (t = 116.4 msec) and are shown in Figure 6-4. The general yield patterns are similar to measurements of the south igloo. However, computed contour lines indicate that all the points on the south and west headwalls move away from the donor magazine, and thus no lines of zero displacement exist. This appears to be consistent, nevertheless, with actual measurements found for the west igloo. In both igloos, the measured displacements are smaller than the

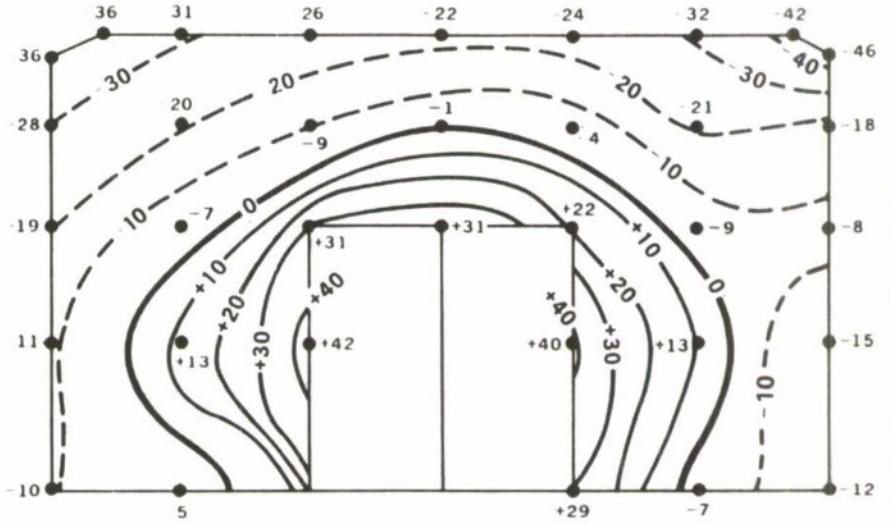

FIGURE 6-1. MOVEMENT OF HEADWALL OF NORTH ACCEPTOR IGLOO
A plus value shows movement away from the donor magazine; a minus value shows movement toward. The units are in hundredths of feet.

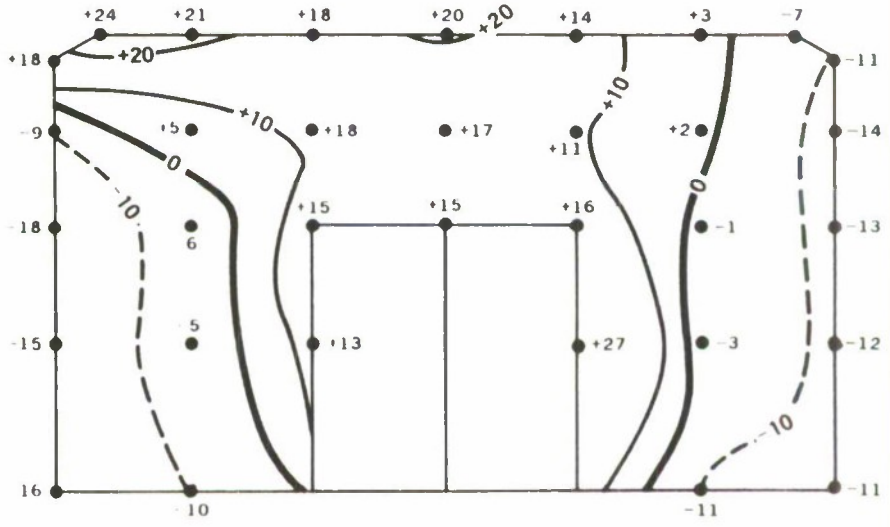

FIGURE 6-2. MOVEMENT OF HEADWALL OF SOUTH ACCEPTOR IGLOO
A plus value shows movement away from the donor magazine; a minus value shows movement toward. The units are in hundredths of feet.

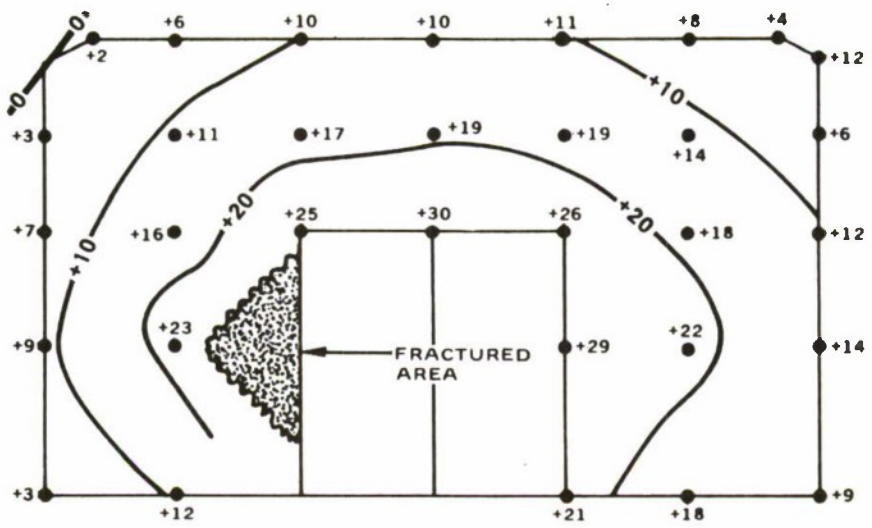

FIGURE 6-3. MOVEMENT OF HEADWALL OF WEST ACCEPTOR IGLOO
Plus values show movement away from donor magazine; one point (upper left) showed no movement. The units are in hundredths of feet.

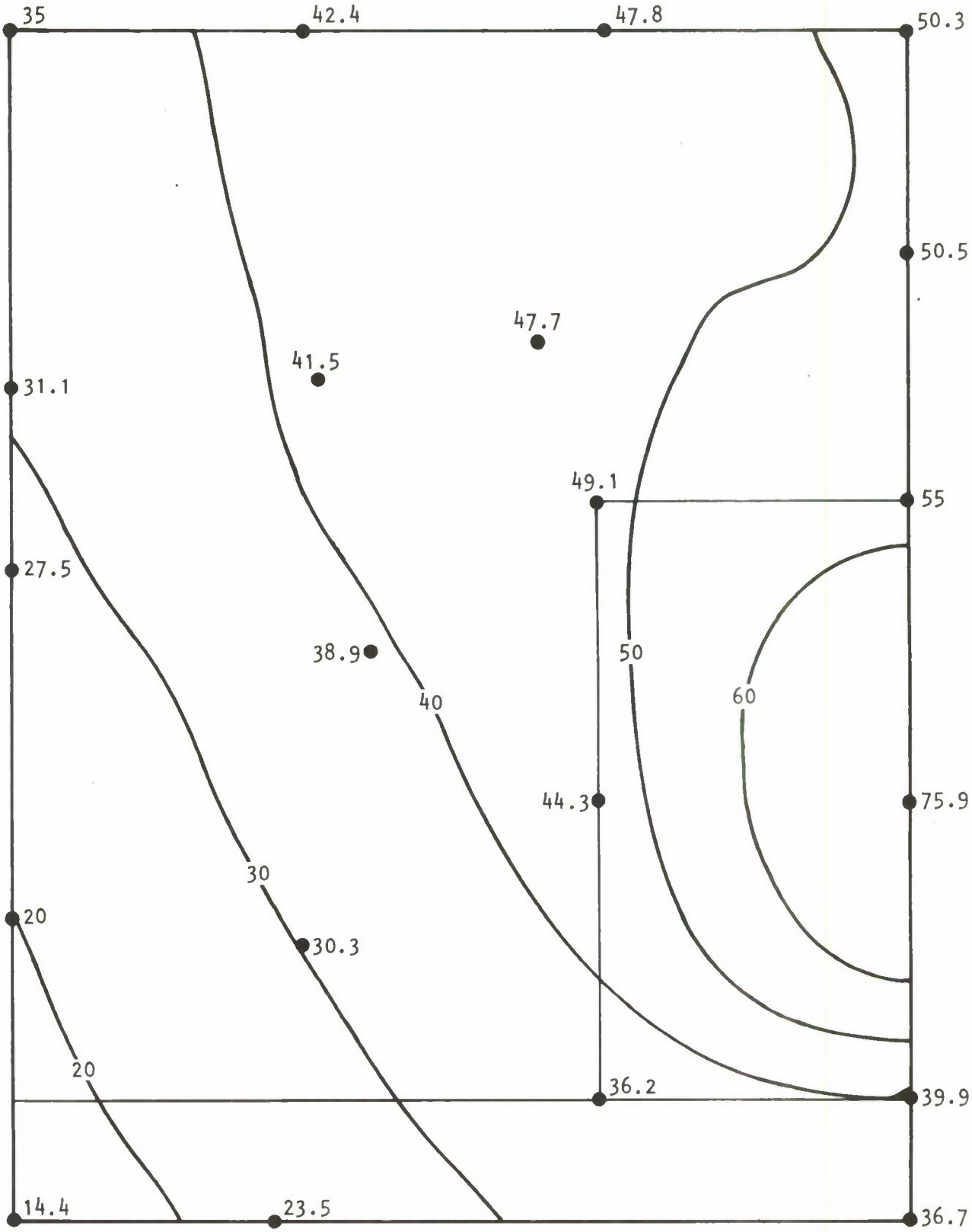

FIGURE 6-4. COMPUTED MOVEMENT OF HEADWALL OF SOUTH ACCEPTOR IGLOO
(Units in hundredths of feet)

computed displacement values. Parameters that can possibly affect the computed results are discussed below:

a. The dampers used to represent the supporting soil behind the headwall were determined by the expression ρC (Section 3.3.5). The actual test data for the earth fill showed a range for C, the wave velocity of the soil medium, from 2,000 to 6,000 ft/sec. In the finite element calculations, a constant value of 4,000 ft/sec was used. Therefore, the damping coefficients may have an error of ± 50 percent. An increase in the wave velocity implies an increase in the damping coefficients. Higher damping coefficients generally result in lower response.

b. It is recognized that the finite element model can only represent the approximate behavior of the structure. The door hinges, for example, were modeled by releasing the moments at discrete points. The modification of stiffnesses due to door hinges was accounted for by the static condensation method (Appendix C). However, the computer program calculates the moments at a node by averaging the moments in all the elements that connect to the node. This averaging in general resulted in large nonzero moments at the door hinges; and when these moments reached yield levels, stiffness of all the elements connecting to the node were erroneously modified. The soil resistance is also lumped at discrete points. If more refined elements were used in the model such that the resisting forces of the arch and of the soil are separated, the high concentration of resisting forces may bring the computational results in closer agreement with observed data for the west igloo.

c. In the mathematical model, the moment/curvature relationship of the concrete headwall and the steel doorways was described by bilinear curves. The yield point and after-yield behavior were estimated by extrapolating from experience with similar data. The results presented in Sections 4 and 5 indicate that

elastic response is a small percentage of the total displacements. A slight change in the slope of the moment/curvature curve after yielding will give rise to substantial changes in the maximum displacements, as well as in the permanent deformations. This phenomenon is illustrated schematically in Figure 6-5.

The computed permanent displacements of the headwall of the north igloo, shown in Figure 6-6, produce contour patterns quite different from the measured displacements (Figure 6-1). The distinctive lines of zero permanent displacement along the steel arch (Figure 6-1) suggest the possibility that the steel arch responds elastically throughout the response history. The elastic property of the steel arch is represented by the dynamic stiffness of the steel, which is extremely high during the initial stage of the responses. The variations of the dynamic stiffness can be obtained by making a study similar to that made in Section 3.3.4 for the supporting soil. The elastic representation of the steel arch does not explain the behavior shown in Figure 6-3 for the west igloo, in which the arch line undergoes permanent displacement. This implies that to predict the response accurately, it is necessary to represent each igloo by a different model with pertinent material properties.

The qualitative similarities between Figure 6-2 and 6-4 suggest that the rigid body rotation about the floor level is about the same in both cases. Therefore, a more favorable comparison will result in this case if the rigid body translations (normal to the headwall) are neglected in each. The elimination of the rigid body components, in any case, does not influence computed stresses in the headwall.

6.1.3 ACCELEROMETER DATA

The accelerometers were installed on the center lines of the igloo floors near the front. Both vertical and horizontal motions were recorded. Only the horizontal component is listed here (Table 6-4) for comparison. The corresponding accelerations computed at node 65 of the mathematical model are tabulated In Table 6-5.

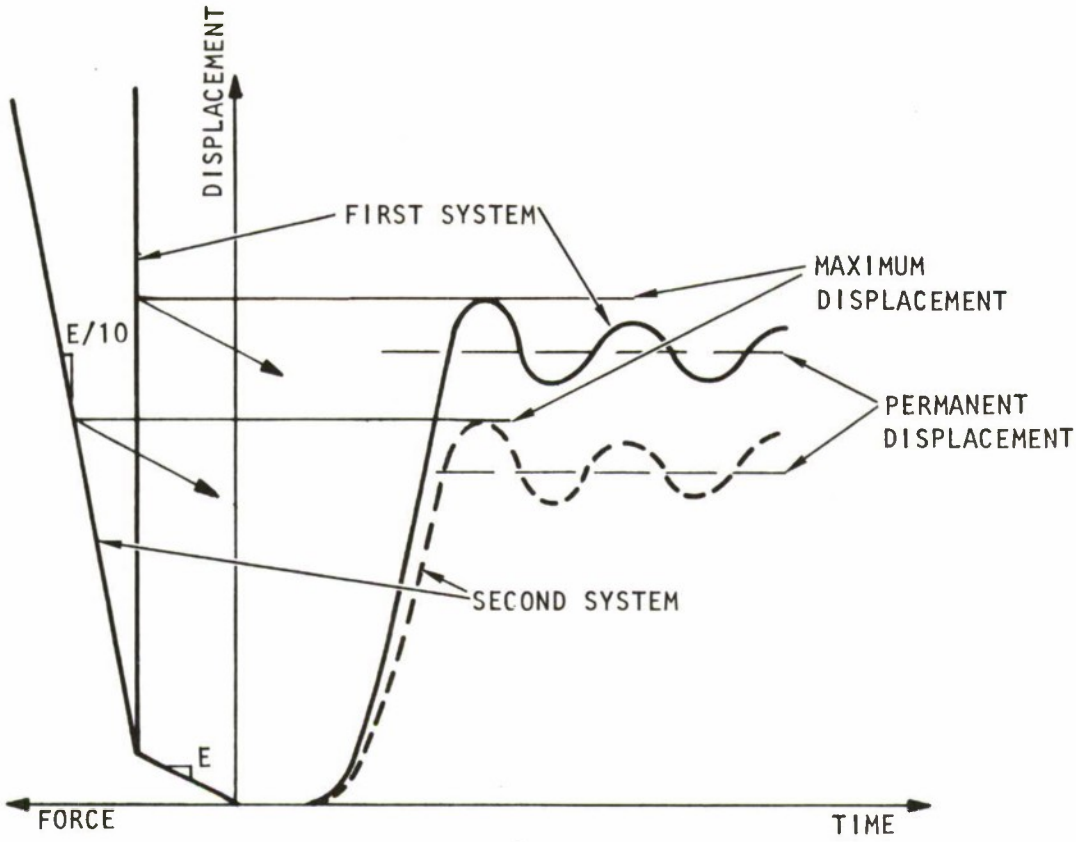

FIGURE 6-5. SCHEMATIC DIAGRAM SHOWING MAXIMUM AND PERMANENT DISPLACEMENTS FOR TWO DIFFERENT AFTER-YIELD STIFFNESSES

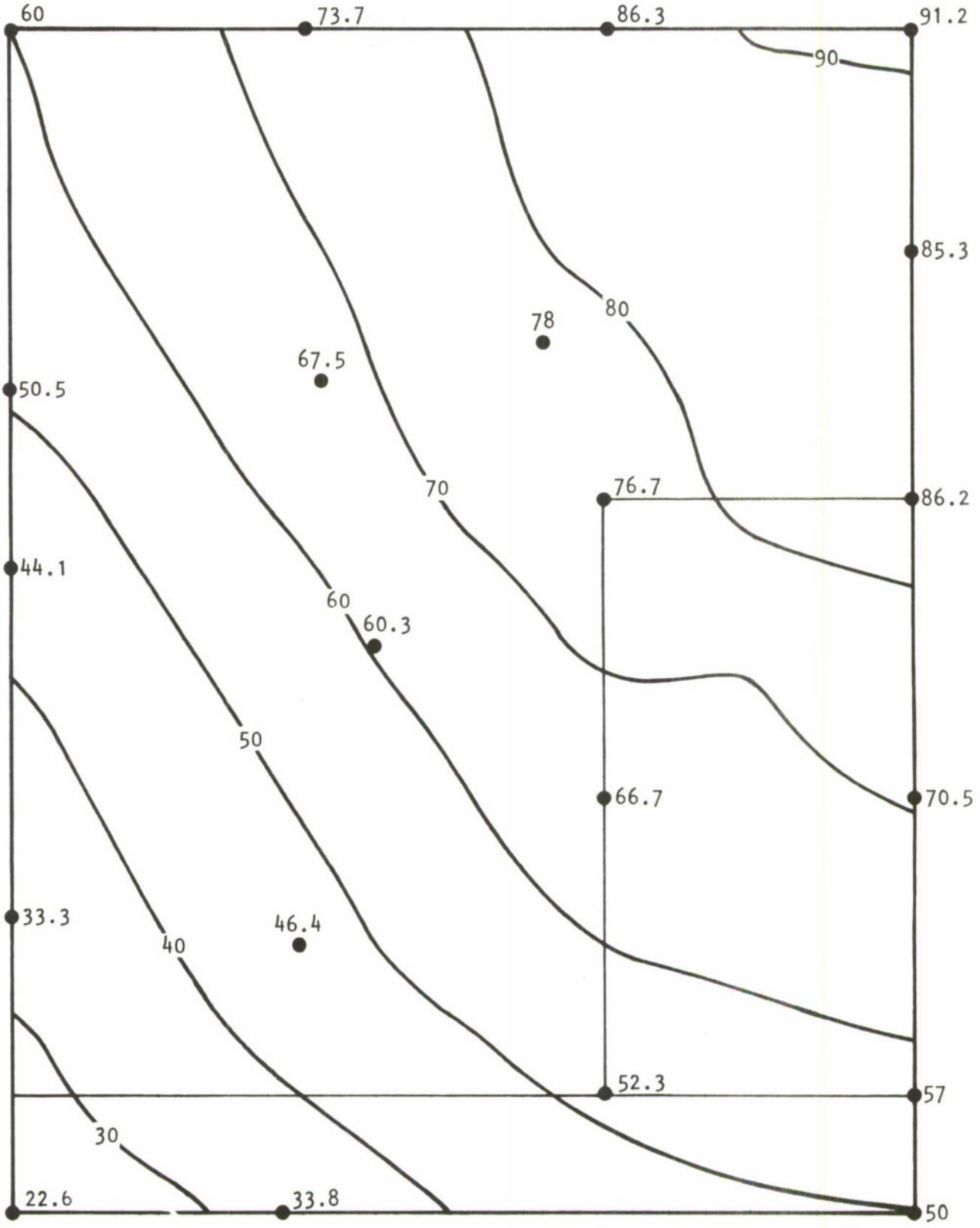

FIGURE 6-6. COMPUTED MOVEMENT OF HEADWALL OF NORTH ACCEPTOR IGLOO
(Units in hundredths of feet)

TABLE 6-4. HORIZONTAL COMPONENTS OF ACCELEROMETER DATA

Location of Accelerometer	Maximum Acceleration g	Approximate Frequency of Accelerations Hz
North Igloo	10.3	490
East Igloo	33.0	545
South Igloo	6.3	500
West Igloo	5.5	533

TABLE 6-5. MAXIMUM ACCELERATIONS OF THE MATHEMATICAL MODEL (NODE 65)

Headwall	Maximum Acceleration g	Approximate Frequency of Accelerations Hz
North Igloo	488*	500
East Igloo	846	500
South & West Igloos	121	500

*The value was obtained by interpolation.

The maximum accelerations between the computed and the measured data are quite different. If the acceleration values in Table 6-5 are averaged over the period from initial motion to maximum velocity--as was done in the last column of Table 6-2--the motions at the center of the top and bottom of the doorways are roughly the same. The displacement contour lines shown in Figures 6-1 through 6-3 also indicate that the doorways are subjected to similar translation. The comparison, therefore, leads to the conclusion that the floor slabs in actual tests behaved very differently from the bottom of the doorway in the finite element representation. In other words, the floor slab predicated in the finite element model is much softer than the actual floor slab in the igloos.

Better agreement may be reached if stiffer material properties are assigned to the concrete base slab and the foundation than were used in the calculations. Nevertheless, this modification of material strengths is not likely to alter the conclusions drawn in the previous paragraphs because it is expected to have only local effects.

6.2 MOTION PICTURE PHOTOGRAPHY

In the Eskimo I Magazine Separation Test, motion picture cameras were installed in the south and west igloos to capture the motion of the doors on film. Since the camera setup was not designed for measuring the door response, the estimates derived for the door motions were very crude and merely served as a description of the measurements from the instrumentation. Two types of data were extracted from the movie film: one was the angular change of the door of the south igloo; the other was the movement of the two top corner points on the doorways of the south and west igloos.

The maximum angular change was observed to be 30^{o}, using the line of the door hinges as reference. If a linear relationship is assumed, the maximum displacement at the center of one door panel is calculated to be

$$d_{max} = 60 \times \sin 30^{o} = 30 \text{ in.}$$

where the width of the door panel is taken as 60 in. This value appears to be high in comparison to either the calculations or the measured permanent deflections.

The maximum displacements on the corner points of doorways were measured to be 4.8 in. $\pm$1.2 in. for the south igloo, and 3.36 $\pm$1.2 in. for the west igloo. The order of magnitude of these values is in the same order as those from the calculations or from the measured permanent deflections.

The maximum velocities measured at the same locations as the displacements are 32.5 ft/sec for the south igloo and 20 ft/sec for the west igloo. These two values are higher than the computed result, which is 16.5 ft/sec.

SECTION 7

CONCLUSIONS AND RECOMMENDATIONS

In this study, the dynamic analyses of a headwall subjected to different explosive loadings were performed using the finite element method. The computed results are compared with the available data from the Eskimo I Test. The following is a summary of the important conclusions of the study:

a. As part of a general program sponsored by the Department of Defense Explosives Safety Board, the present study is a relatively successful attempt to predict the response of magazine headwalls using the finite element techniques.

b. The measured values of the maximum velocities and accelerations in the south igloo are in good agreement with the calculated results.

c. The characteristics of the response time histories of the headwalls are similar to those of a simple elastoplastic system. Since the concrete headwall undergoes considerable yielding, the present study indicates the suitability of the INSLAB Code for predicting the dynamic response of magazine headwalls.

d. The calculated permanent displacement contours in the south igloo are in part similar to those of the measured contours in the south and west igloos. It is believed that the model of material properties in the finite element calculations represents a combination of characteristics found in the actual properties of the south igloo and the west igloo.

e. The computed values of the maximum velocities and accelerations in the east and north igloos are found to be consistently greater than the measured values. The distribution of the permanent displacements as computed are quite different from those measured.

For a better correlation of the analytical and measured responses, it is recommended that any future analytical studies should include the following considerations:

a. The input to the finite element model, whether obtained from measurements or estimates, will significantly affect the calculated responses. The time histories of the blast loadings, the yield criteria of the headwall, and the material properties of the supporting soil and the steel arch are among the most important factors that must be evaluated with care.

b. The existing mathematical model should be improved to better represent the geometrical details of the headwall. Every important location on the headwall for which measurements are available should be assigned a node in the finite element mesh for proper comparison of calculated responses with measured responses. This can be accomplished only by increasing the total number of nodes and elements in the mesh. Although the INSLAB Code at present has limitations on the maximum number of elements or nodes that can be used, the capacity of the code can very easily be increased.

c. The soil supporting the headwalls is represented by equivalent damping elements based on one-dimensional wave propagation theory. A better model for the soil may be obtained by spring-mass-dashpot elements. The appropriate properties of the spring-mass-dashpot systems can be obtained from the auxiliary study, preferably a linear three-dimensional analysis.

d. The solution for the east igloo exhibited some instabilities at late times. Since the large integration time-step used in the calculation is suspected to be responsible for the instabilities, it should be investigated further. It may be found necessary to reduce the integration time-step, particularly at late times.

e. The input data to the finite element model always involve some uncertainties. The response is very sensitive to some of the input parameters. It is suggested that in future studies, more than one calculation be performed, using preferably the upper bound, the mean, and the lower bound values of important parameters for each calculation.

f. For future tests similar to Eskimo I and II, pretest prediction analyses should be considered. The results from the pretest analyses will help guide the test planners in selecting the type and location of instrumentation.

APPENDIX A

DESCRIPTION OF INSLAB AND SLAB CODES

The development of the finite element method for plate analysis has concentrated on the search for a suitable element. One of the main problems was to reduce the three-dimensional problem to a two-dimensional one, which could be more easily treated. The assumption that there is linear kinematic variation along the thickness requires normal slope compatibility along element interfaces in order to achieve three-dimensional continuity and monotonic convergence. Nevertheless, lack of continuity between nodes may not be very important. However, presence of rigid body and constant curvature modes is fundamental to uniform convergence to the true solution.

Rectangular elements have been developed by a number of workers. Adini and Clough, Reference 2, developed a 12-degree-of-freedom rectangular element by employing a complete 3rd-order polynominal expansion in x and y and two additional terms in x^3y and xy^3. A similar element was developed by Melosh, Reference 3. These elements maintained slope conformity only at the four corner points. The development of a fully compatible parallelogram element is attributed to Argyris (Reference 4). The construction of fully compatible polynomial expansion for rectangular shapes was solved by Bogner et al. (Reference 5).

The development of triangular elements was prompted by their wider range of application to plates and shells of arbitrary geometry than the rectangular elements. The search for a suitable coordinate system and interpolation functions retarded the development of triangular elements. Tocher, Reference 6, and Clough and Tocher, Reference 7, did work that has resulted in fully compatible cubic triangles.

Arbitrary quadrilaterals can be constructed by assembling several triangles and eliminating internal nodes by static condensation. One such element is due to De Veubeke, Reference 8. Another is due to Felippa and

Clough, Reference 9, and is used in the computer program (INSLAB Code) that AA has used in this project. This element is described in greater detail below.

Recently, isoparametric shape functions have been used to develop curved shell and plate elements. An example is given in Reference 10.

Sections A.1 through A.6 describe the INSLAB Code, an existing computer program available at AA for the inelastic dynamic analysis of bending and transverse shear deformations in thin and moderately thick inelastic plates. Transverse pressure loadings along the surface of the plate and rigid-body motions of the plate boundaries comprise the input excitations. The plate can be of arbitrary shape and can have beam or column supports, concentrated masses, and interior holes at any arbitrary location. INSLAB Code is also capable of analyzing folded plate structures with transverse pressure loadings along the surface of the plate.

Section A.7 presents a brief description of SLAB Code, another existing AA program available for elastic analysis of plates.

A.1 COORDINATE SYSTEM AND TYPE OF ELEMENTS

The sign convention for the INSLAB Code is based on a right-hand Cartesian coordinate system. The sign conventions for deformation and loading are shown in Figure A-1.

The basic element used in INSLAB Code is a quadrilateral element that is assembled from four linear curvature compatible triangles. These triangles have a cubic displacement function with a piece-wise continuous second derivative, assuring compatibility of the displacements and the internal rotations at the nodal points. The quadrilateral elements have 12 degrees of freedom. If shear distortions are considered, 6 additional degrees of freedom are added to the element stiffness matrix; however, these 6 degrees of freedom are eliminated from the solution by static condensation.

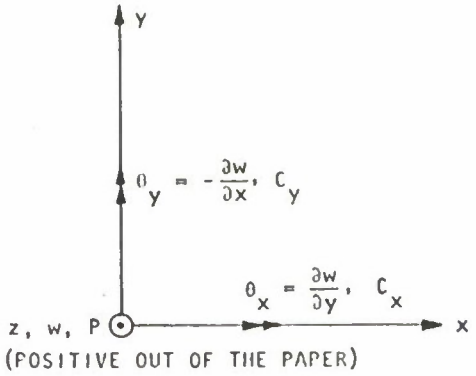

x, y, z = LOCAL COORDINATE SYSTEM

w, θ_x, θ_y = TRANSLATIONAL AND ROTATIONAL DEGREES OF FREEDOM AT EACH NODE POINT

P = APPLIED EXTERNAL TRANSVERSE FORCES

C_x, C_y = APPLIED EXTERNAL MOMENTS ABOUT THE X AND Y AXES

(a) DISPLACEMENT AND FORCE CONVENTIONS

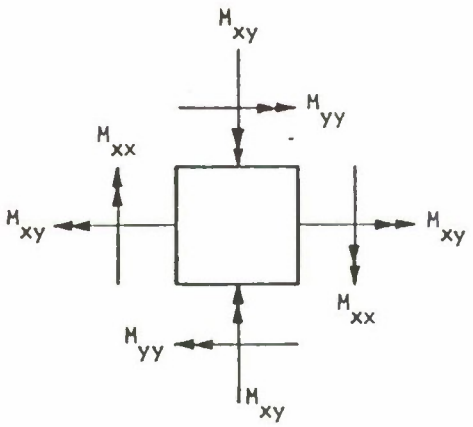

X-Y MOMENTS

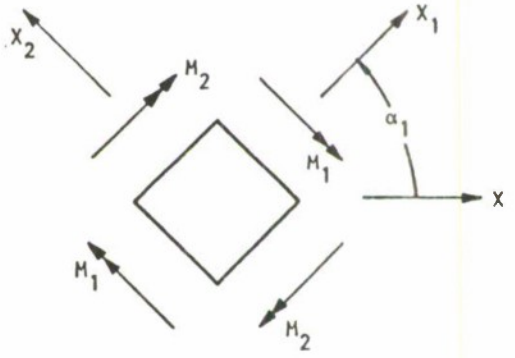

PRINCIPAL MOMENTS

POSITIVE MOMENTS PRODUCE COMPRESSION AT THE UPPER SURFACE

(b) INTERNAL MOMENT CONVENTIONS

⊕ INTO THE PAPER

⊙ OUT OF THE PAPER

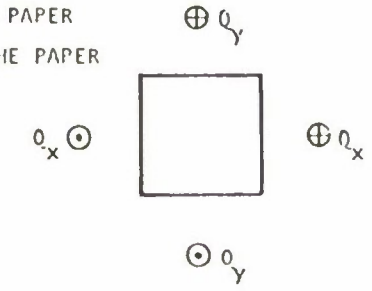

(c) TRANSVERSE SHEAR CONVENTION

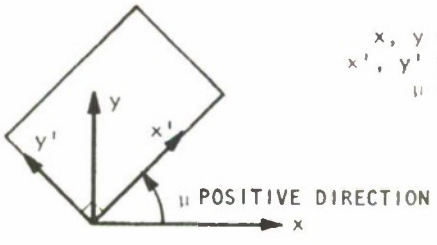

x, y = GLOBAL AXES

x', y' = SKEW AXES

μ = SKEW ANGLE

(d) SKEWED PLATE CONVENTION

AJA1860

FIGURE A-1. SIGN CONVENTIONS FOR INSLAB CODE

The construction of the quadrilateral element is shown in Figures A-2(a) through A-2(d). The LCCT-12 triangle of Figure A-2(a) is first constrained to the LCCT-11 triangle of Figure A-2(b) by defining a linear variation of slope along one boundary. Four LCCT-11 triangles are then combined to obtain the quadrilateral element shown in Figure A-2(c). The internal degrees of freedom are eliminated by static condensation as shown in Figures A-2(d) and A-2(e). Individual triangular elements and prismatic beam elements are also provided. The individual triangular elements have nine degrees of freedom while the prismatic beam elements have six degrees of freedom. These elements and their corresponding degrees of freedom are shown in Figures A-3(a) and A-3(b). Column element with three unknown degrees of freedom are shown in Figure A-3(c).

In the formulation of the element stiffness matrix, the Kirchoff hypothesis has been assumed, i.e., plane sections remain plane both before and after bending. It is noted that this assumption effectively eliminates shear distortions from the assumed behavior and is exact only for relatively thin plates; however, this theory has been extended to account for shear distortion in an approximate way by adding a simple shear mechanism to the Kirchoff hypothesis.

A.2 MATERIAL

A.2.1 ELASTIC ANALYSIS

A.2.1.1 Orthotropic Material

The principal elastic axes are assumed to be $\bar{x}$, $\bar{y}$, $\bar{z}$, where $\bar{x}$ forms an angle ϕ with the global x-axis, Figure A-4.

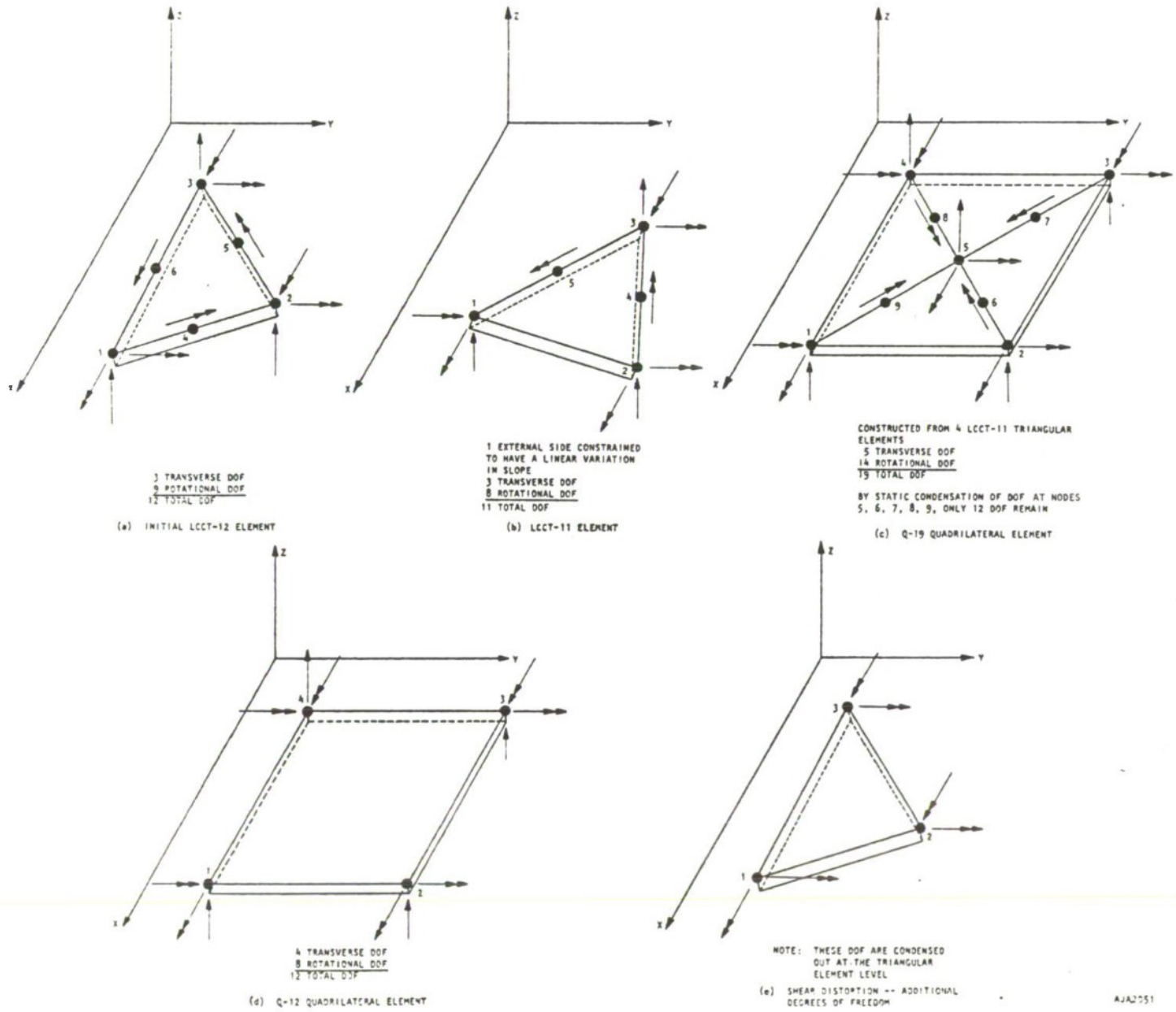

FIGURE A-2. CONSTRUCTION OF 12-DOF QUADRILATERAL ELEMENT

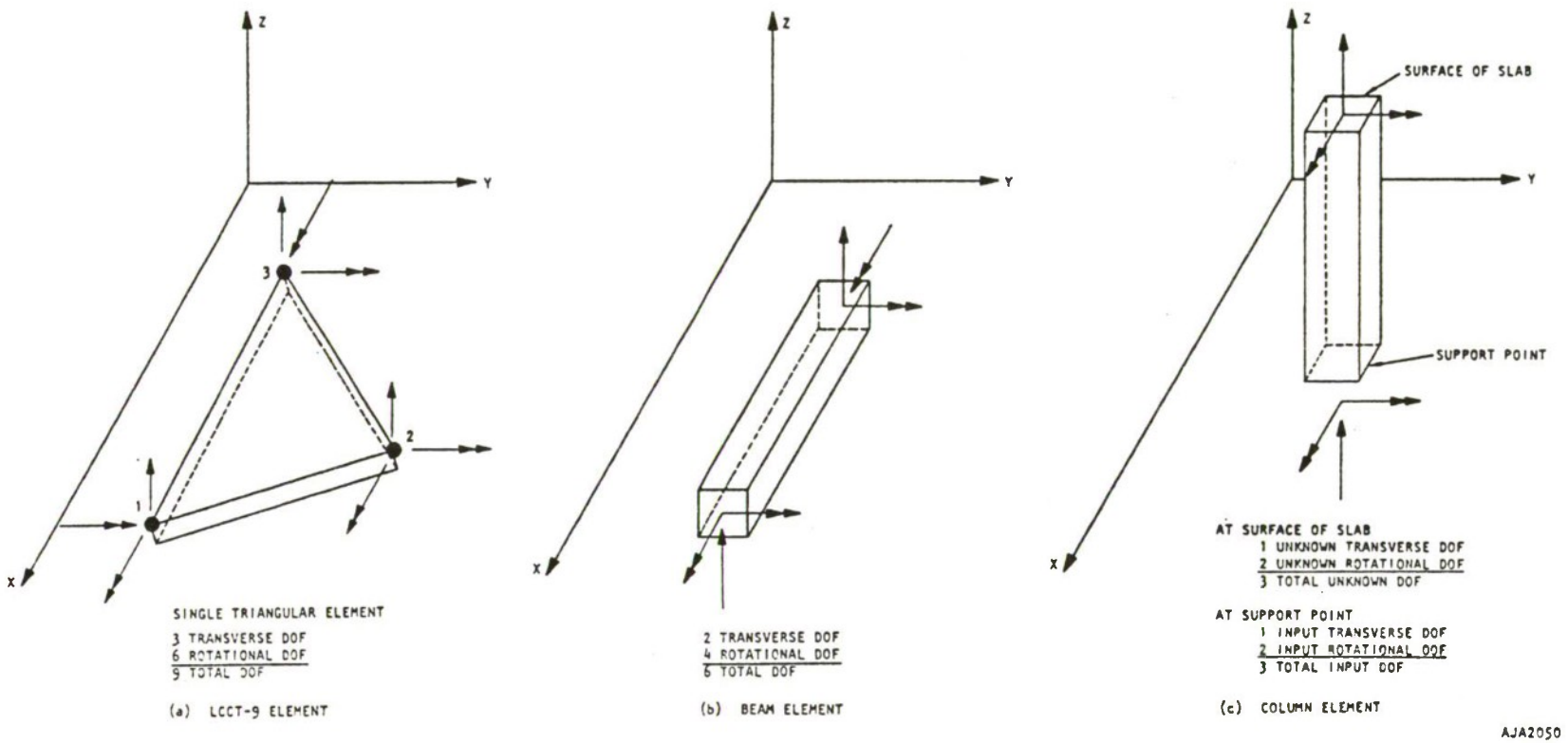

FIGURE A-3. TRIANGULAR ELEMENT, BEAM ELEMENT, AND COLUMN ELEMENT DEGREES OF FREEDOM

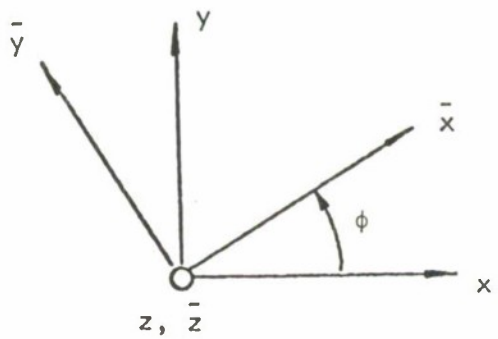

FIGURE A-4. PRINCIPAL ELASTIC AXES FOR ORTHOTROPIC MATERIAL

The stress-strain relation referred to the elastic axes is

$$\begin{Bmatrix} \sigma_{\bar{x}} \\ \sigma_{\bar{y}} \\ \tau_{\bar{x}\bar{y}} \\ \tau_{\bar{x}\bar{z}} \\ \tau_{\bar{y}\bar{z}} \end{Bmatrix} = \begin{bmatrix} E_1/\chi & E_2\nu_{12}/\chi & . & . & . \\ E_1\nu_{21}/\chi & E_2/\chi & . & . & . \\ . & . & G_{12} & . & . \\ . & . & . & G_{13} & . \\ . & . & . & . & G_{23} \end{bmatrix} \begin{Bmatrix} \varepsilon_{\bar{x}} \\ \varepsilon_{\bar{y}} \\ \gamma_{\bar{x}\bar{y}} \\ \gamma_{\bar{x}\bar{z}} \\ \gamma_{\bar{y}\bar{z}} \end{Bmatrix}$$

where

E_1, E_2 = Elastic moduli in the $\bar{x}$ and $\bar{y}$ directions

ν_{12}, ν_{21} = Poisson's ratios ($E_2\ \nu_{12} = E_1\ \nu_{21}$)

χ = $1 - \nu_{12}\ \nu_{21}$

G_{12}, G_{13}, G_{23} = Shear moduli (the last two are needed only if the transverse shear effect is included)

To simplify the input, the following material constants will be defined as

$E = \sqrt{E_1 E_2}$ mean modulus

$\delta = E_1/E_2$ modulus ratio

$\nu = \sqrt{\nu_{12} \nu_{21}}$ mean Poisson's ratio

$\nu_{G12} = (E/2G_{12})-1$ fictitious Poisson's ratio associated with G_{12}

Then the in-plane stress-strain relation in the elastic axes becomes

$$\begin{Bmatrix} \sigma_x \\ \sigma_y \\ \tau_{xy} \end{Bmatrix} = \frac{E}{1-\nu^2} \begin{bmatrix} \sqrt{\delta} & \nu & \cdot \\ \nu & \frac{1}{\sqrt{\delta}} & \cdot \\ \cdot & \cdot & \frac{1-\nu^2}{2(1+\nu_{G12})} \end{bmatrix} \begin{Bmatrix} \varepsilon_x \\ \varepsilon_y \\ \gamma_{xy} \end{Bmatrix}$$

The moment-curvature relation is obtained by multiplying this matrix by $h^3/12$, where h is the plate thickness.

A.2.1.2 Isotropic Material

If the material is isotropic, $E_1 = E_2 = E$, $\nu_{12} = \nu_{21} = \nu = \nu_{G12}$ and $\delta = 1$. The angle ϕ is not needed.

A.2.2 BILINEAR ANALYSIS

Analysis is carried out by applying incremental load steps to the structure. The assumptions inherent in the bilinear analysis are as follows:

a. The plate materials must be initially isotropic and the moment-curvature relationship is bilinear in the principal directions, X_1 and X_2, with slopes D and ξD (Figure A-5(a)). Although D and ξ must be the same in all directions, the positive and negative yield moments in the X_a and X_b directions can be specified uniquely. (See Figure A-5 for definition of yield mechanisms and directions of axes.)

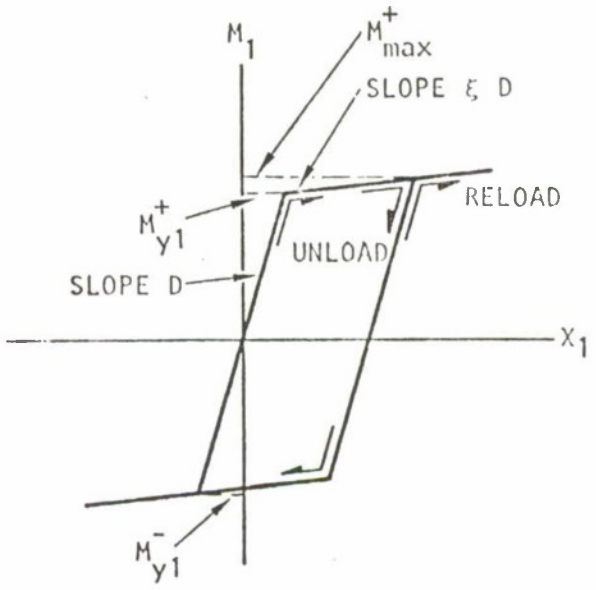

(a) MOMENT-CURVATURE RELATIONS IN X_1 PRINCIPAL DIRECTION

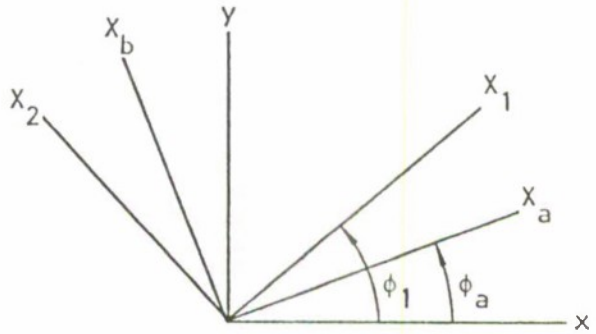

(b) COORDINATE AXIS DEFINITIONS

NOTE: IN ABOVE SKETCHES

$$D = \frac{Eh^3}{12(1 - \nu^2)}$$

x, y = REFERENCE AXES

X_a, X_b = ORTHOGONAL DIRECTIONS OF REINFORCEMENT IN SLAB

X_1, X_2 = PRINCIPAL DIRECTIONS

AJA1370

FIGURE A-5. DESCRIPTION OF YIELDING MECHANISM

b. The yield moments M^+_{ya}, M^+_{yb}, M^-_{yb} and M^-_{yb} in two orthogonal directions X_a, X_b (e.g., direction of reinforcements) define the bending resistance of the plate at each point (Figure A-5(b)). The yield moments in the principal direction X_1, X_2 are:

$$M^+_{y1} = M^+_{ya} \cos^2 (\phi_a - \phi_1) + M^+_{yb} \sin^2 (\phi_a - \phi_1)$$

$$M^+_{y2} = M^+_{ya} \sin^2 (\phi_a - \phi_1) + M^+_{yb} \cos^2 (\phi_a - \phi_1) \qquad \text{(A-1)}$$

$$M^-_{y1} = M^-_{ya} \cos^2 (\phi_a - \phi_1) + M^-_{by} \sin^2 (\phi_a - \phi_1)$$

$$M^-_{y2} = M^-_{ya} \sin^2 (\phi_a - \phi_1) + M^-_{yb} \cos^2 (\phi_a - \phi_1)$$

In Equation A-1, ϕ_a is the angle between the direction of reinforcement, X_a, and the positive X-axis; and ϕ_1 is the angle between the principal axis, X_1, and the positive X-axis (positive counterclockwise).

c. Yielding at a point is assumed to take place when the principal moment exceeds the yield moment in that direction, as defined by Equation A-1. Once yielding takes place at a point within an element, all checks as to whether the plate continues to yield at that point are referred to the principal direction at which yielding first occurred. This is equivalent to assuming a weakened direction at that point.

d. When one-way yielding occurs, Poisson's ratio is assumed to be zero, i.e., no interaction occurs between the perpendicular moments.

As indicated above, the user is free to specify different yield moments in the X_a and X_b directions; however, if these moments are significantly different from one another, the assumption that yielding occurs in the direction of the principal moment may be unrealistic. To illustrate this, consider the case in which $M^+_{ya} >> M^+_{yb}$. For this case, the magnitude of the principal yield moments, as calculated from the first two expressions in Equation A-1, will approach that of M^+_{ya}. Assumption (c) as given above then implies that, even though the principal moments are much greater than M^+_{yb}, no yielding will take place unless these principal moments are also greater than M^+_{y1} or M^+_{y2} in Equation A-1. This may not be physically realistic; hence when using this slab analysis, the yield moments defined for two perpendicular directions at a point should not differ greatly from one another.

A.2.3 ELEMENT PROPERTIES

The properties of a general quadrilateral element are defined by the nine points shown in Figure A-6. These points are the four external nodes, the cg of the quadrilateral, and the cg's of each of the four triangles that make up the quadrilateral. A 3 x 3 stress-strain relationship matrix [CM] is determined for each of these nine points. From this, moment-curvature relationships at each point can be defined.

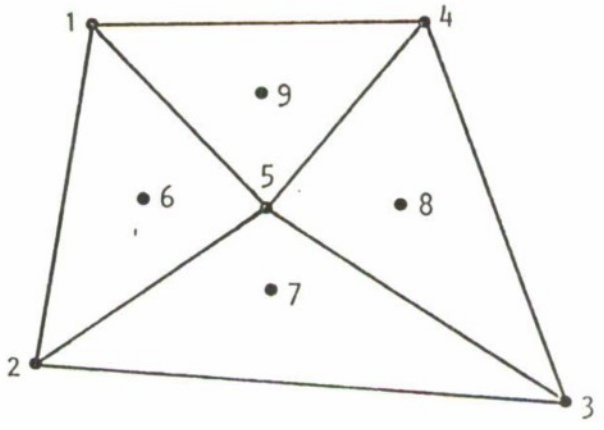

FIGURE A-6. QUADRILATERAL ELEMENT IN NONLINEAR SLAB ANALYSIS

In the slab analysis, moments are calculated at each of the nine node points in each quadrilateral element. The properties at Nodes 6 to 9 (in Figure A-6) are used to control the stiffness properties of each triangular subelement, i.e., if yielding occurs at any of these four points, the corresponding triangular subelement is considered to have yielded, and the stiffness matrix for the quadrilateral is modified accordingly. It is noted that the element stiffness matrices and the stress strain relations matrix, [CM] for each node point are formulated in different regions of the program and are not related to one another. Therefore, the [CM] matrices for the corner node points of an element are not directly effected by a change in status (i.e., yielding) of that element.

A 2.4 PROCEDURES OF ANALYSES

The procedures used in analyzing a slab with bilinear material properties are outlined in the flowchart of Figure A-7. This flowchart is self-explanatory; however, a number of features of the procedures are noteworthy and will be briefly discussed.

At the end of each load step principal moments at each node point M_1, M_2 and ϕ_1 are computed, as are M^+_{y1}, M^+_{y2}, M^-_{y1} and M^-_{y2} from Equation A-1. A comparison of the principal moments against the yielding moments M^+_{y1}, etc., indicates whether the material has yielded at that point. The possible material property characteristics of a given element in the slab are as follows:

a. Elastic (isotropic) with $E_1 = E_2 = E$; $G_{12} = \dfrac{E}{2(1 + \nu)}$.

b. One-way yielding. For example, if the material yields in the X_1 direction (i.e., $M_1 > M^+_{y1}$ and $M^-_{y2} < M_2 < M^+_{y2}$), then the material is assumed to behave orthotropically with X_1 and X_2 as principal elastic direction. For this case, $E_1 = \xi E$, $E_2 = E$, and Poisson's ratio $\nu_{12} = \nu_{21} = 0$ (no interaction).

c. Two-way yielding. The material becomes isotropic again with modulus ξE and plastic Poisson's ration ν_p.

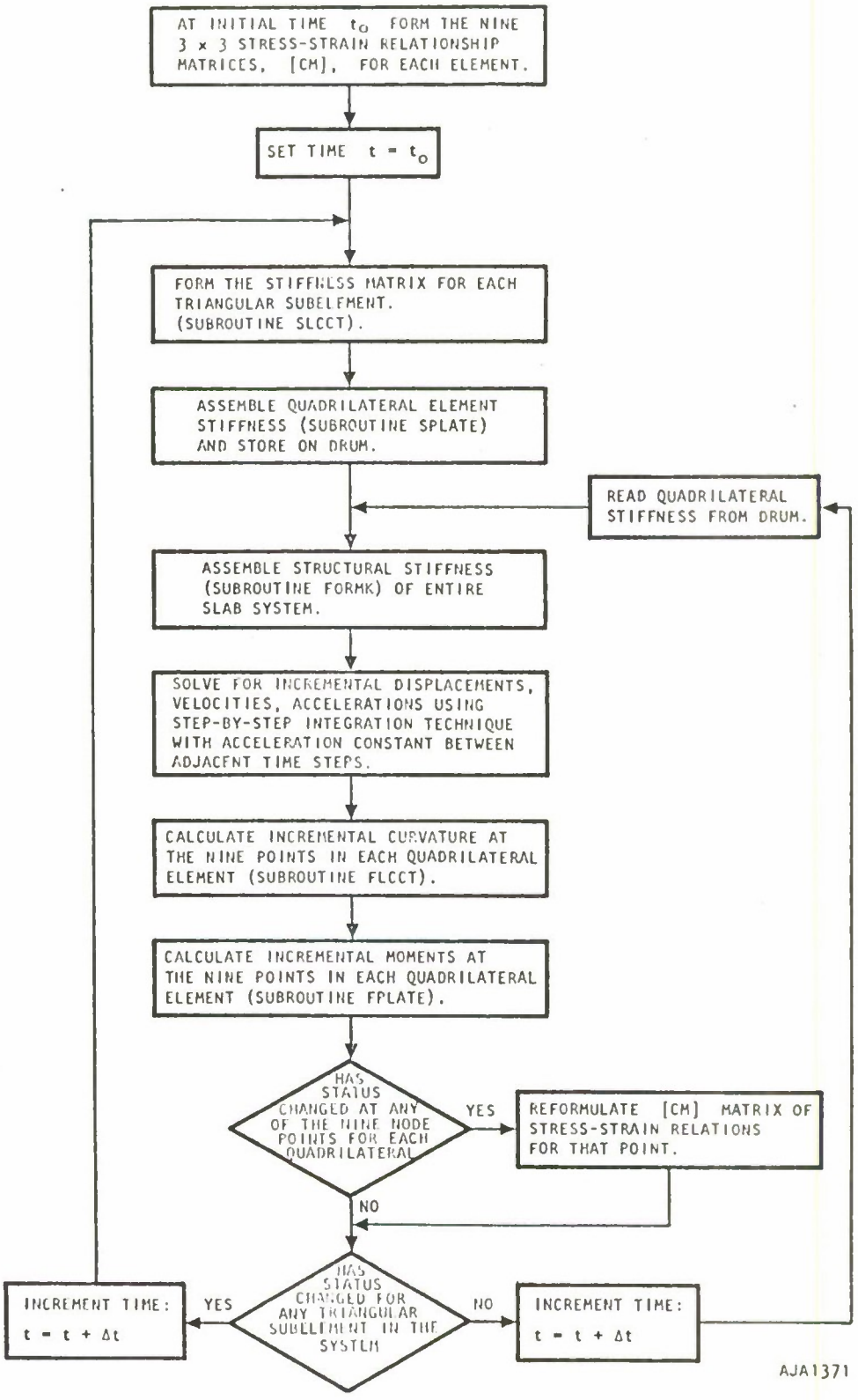

FIGURE A-7. ANALYSIS PROCEDURE FOR INSLAB CODE

d. Yielding in one direction and unloading from the yield region in the other direction. For example, when $M_1 < M^+_{max}$ Figure A-5(a) and $M_2 > M^+_{y2}$, the material is assumed to behave orthotropically with $E_1 = E$, $E_2 = \xi E$, and $\nu_{12} = \nu_{21} = 0$.

The previous principal moment-curvature histories at each point are utilized in the calculations of node point moments and element stiffnesses to account for the inelastic response of the slab and the Bauschinger effect (Figure A-5(a)).

In order to conserve computer time and programming effort, an iterative procedure has not been used in this analysis. Instead, the properties and yield conditions at time t are used to solve for the incremental displacements, velocities, and accelerations at time $t + \Delta t$; however, since the time step Δt is small, this error should not be significant. An attempt to reduce this error has involved a correction of the moments at a node point if yielding has occurred at that point during time $t + \Delta t$. This correction is illustrated in Figure A-8. Although this correction results in a moment that is not compatible with the stiffness used to calculate the incremental displacement, it is apparent that this reduced moment is a more realistic representation of the yielded condition at that point.

A.3 DYNAMIC ANALYSIS

A.3.1 MASS MATRIX

Lumped mass terms corresponding to the transverse nodal displacements are obtained by integrating the product of the distributed mass and the corresponding interpolation function over the element. An arbitrarily chosen small number is used to represent the lumped mass moments of inertia associated with rotational nodal displacements. This is equivalent to lumping the distributed mass into small but finite points, and leads to a diagonal mass matrix with all positive diagonal terms.

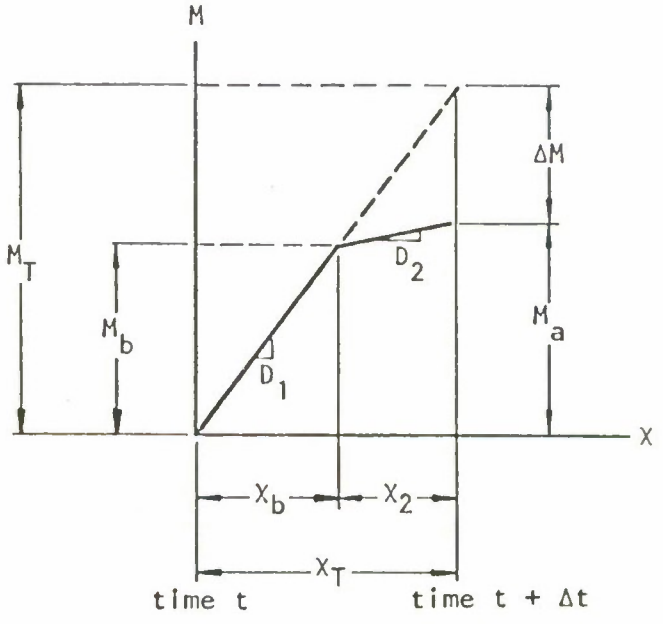

NOTE:

1. YIELDING HAS OCCURRED BETWEEN TIMES t AND $t + \Delta t$.
2. STIFFNESS D_2 HAS BEEN USED TO CALCULATE INCREMENTAL RESPONSE (AND INCREMENTAL CURVATURE χ_T) AT TIME $t + \Delta t$.
3. MOMENT CORRESPONDING TO STIFFNESS D_1 AND CURVATURE χ_T IS M_T, WHEREAS MOMENT CORRESPONDING TO YIELDED CONDITION IS CLOSER TO M_a.
4. CORRECTION APPLIED TO M_T TO ACCOUNT FOR YIELDING IS:

$$\Delta M = M_T - M_b - D_2 \chi_T \left[1 - \frac{M_b}{M_T}\right]$$

OR

$$\Delta M = \left[1 - \frac{M_b}{M_T}\right](D_1 - D_2)\chi_T$$

AJA1369

FIGURE A-8. MODIFICATION OF PRINCIPAL MOMENT TO INCLUDE YIELDING EFFECTS

A.3.2 NUMERICAL INTEGRATION OF EQUATIONS OF MOTION

A step-by-step integration procedure that assumes a constant acceleration between successive time increments has been used (Figure A-9). In addition, a viscous damping mechanism has been incorporated into the analysis. In order to conserve computer storage, the damping matrix has been assumed to be of the following form:

$$[C] = \alpha[M] + \beta[K] \qquad \text{(A-2)}$$

where

$[C]$, $[M]$, $[K]$ = Damping, mass, and stiffness matrices of the entire slab element

α, β = Constants of proportionality

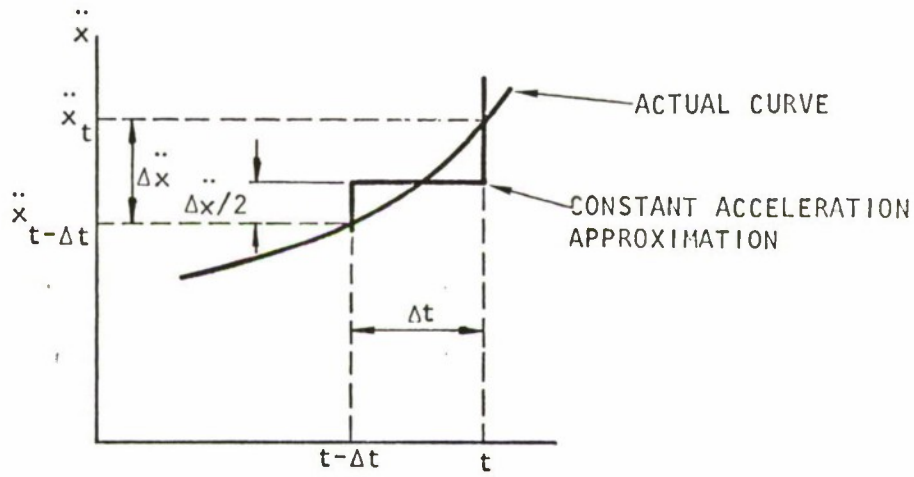

NOTE: FOR CONSTANT ACCELERATION METHOD:

$$\ddot{x}(t) = \ddot{x}_{t-\Delta t} + \Delta\ddot{x}$$

$$\dot{x}(t) = \dot{x}_{t-\Delta t} + \frac{1}{2}\left(\ddot{x}_{t-\Delta t} + \ddot{x}_{t}\right)\Delta t$$

$$x(t) = x_{t-\Delta t} + \dot{x}_{t-\Delta t}\,\Delta t + \frac{\Delta t^2}{4}\left(\ddot{x}_{t} + \ddot{x}_{t-\Delta t}\right)$$

AJA1372

FIGURE A-9. CONSTANT ACCELERATION METHOD

From this, it can be shown that the evaluation of the equations of motion

$$[M]\left\{\ddot{X}_t\right\} + [C]\left\{\dot{X}_t\right\} + [K]\left\{X_t\right\} = \left\{P_t\right\} \tag{A-3}$$

can be reduced to the solution at each time step of the following system of equivalent static equations:

$$\left\{K_e\right\}\left\{u_e\right\} = \left\{P_e\right\} \tag{A-4}$$

where $[K_e]$, $\{u_e\}$, and $\{P_e\}$ can be regarded as an equivalent stiffness matrix, displacement vector, and load vector for the slab at time t. These matrices take the form:

$$\begin{aligned}
\left[K_e\right] &= \frac{C_1}{C_2}[M] + [K] \\
\left\{u_e\right\} &= C_2\left[\left\{X_t\right\} - \left\{X_{t-\Delta t}\right\}\right] - \beta\left\{B_t\right\} \\
\left\{P_e\right\} &= \left\{P_t\right\} - \left\{P_{t-\Delta t}\right\} + [M]\left[\left\{A_t\right\} + \left(\alpha - \frac{C_1}{C_2}\beta\right)\left\{B_t\right\}\right]
\end{aligned} \tag{A-5}$$

where

$$\begin{aligned}
C_1 &= \frac{4}{\Delta t^2} + \frac{2\alpha}{\Delta t} \\
C_2 &= 1 + \frac{2\beta}{\Delta t}
\end{aligned} \tag{A-6}$$

$$\begin{aligned}
\left\{A_t\right\} &= \frac{4}{\Delta t}\left\{\dot{X}_{t-\Delta t}\right\} + 2\left\{\ddot{X}_{t-\Delta t}\right\} \\
\left\{B_t\right\} &= 2\left\{\dot{X}_{t-\Delta t}\right\}
\end{aligned} \tag{A-7}$$

and

$$\{\Delta X_t\} = \{X_t\} - \{X_{t-\Delta t}\} = \frac{1}{C_2}\left[\{u_e\} - \beta \{B\}\right]$$

$$\{\Delta \dot{X}_t\} = \{\dot{X}_t\} - \{\dot{X}_{t-\Delta t}\} = \frac{2}{\Delta t}\{\Delta X_t\} - \{B\}$$

$$\{\Delta \ddot{X}_t\} = \{\ddot{X}_t\} - \{\ddot{X}_{t-\Delta t}\} = \frac{4}{\Delta t^2}\{\Delta X_t\} - \{A\} \qquad \text{(A-8)}$$

Now, the procedure used in determining the incremental displacements, velocities, and accelerations at time t is as follows:

1. Calculate C_1 and C_2 (only at the beginning of the problem) using Equation A-6.

2. Form the effective stiffness matrix $[K_e]$ from Equation A-5. and triangularize $[K_e]$.

3. Calculate $\{A_t\}$ and $\{B_t\}$ from Equation A-7.

4. Form equivalent load matrix $\{P_e\}$ from Equation A-5.

5. Solve for equivalent displacements from

$$\{u_e\} = [K_e]^{-1}\{P_e\}$$

6. Solve for the actual displacements, velocities, and accelerations at time t from Equation A-8.

An option to vary the integration time step is provided in INSLAB to optimize the solution time.

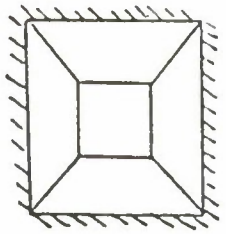

(a) STRUCTURE

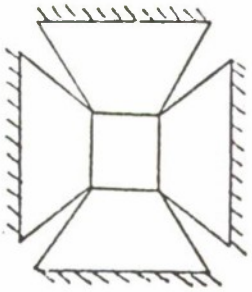

(b) DEVELOPMENT

NUMEL = 26
NUMNP = 37
NNPKS = 33
NAXPD = 6

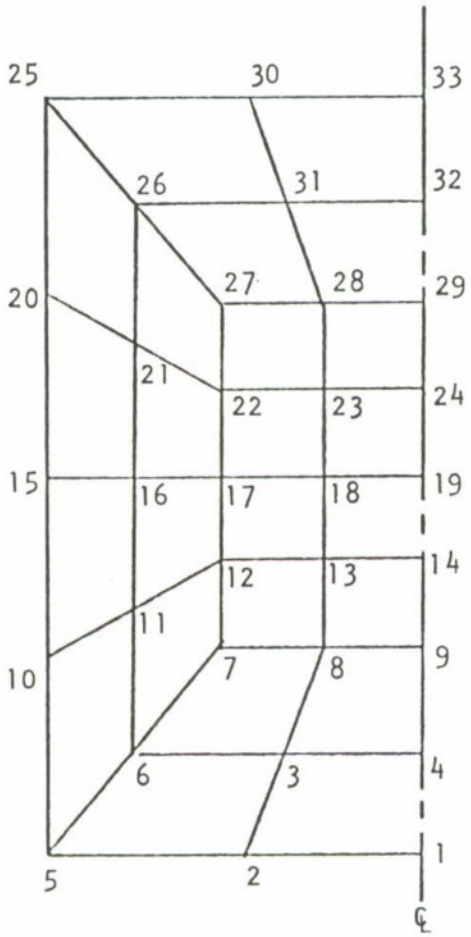

(c) SYSTEM(a)

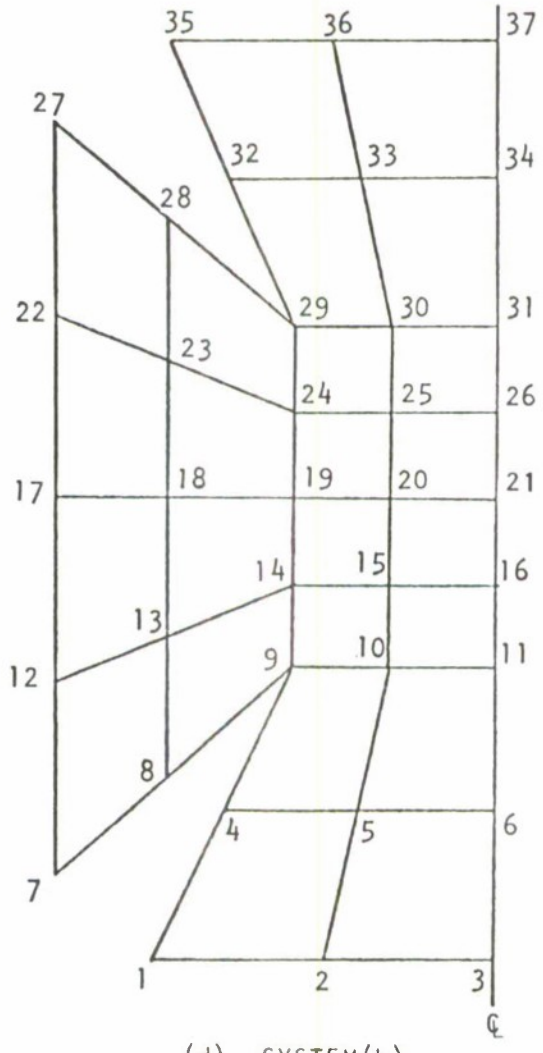

(d) SYSTEM(b)

FIGURE A-10. NODAL POINT NUMBERING FOR FOLDED PLATE STRUCTURE

A.3.3 LOAD VECTOR

Both ground accelerations and applied loads (concentrated and/or distributed) can be handled. For ground accelerations, three rigid boundary components (translation and rotation about x and y axes) relative to a specified reference point can be defined with the corresponding three different time histories. Five different patterns of external loads with five different time histories can be specified. Each loading may include both concentrated and distributed contributions. All load terms are defined at a number of discrete times and linear interpolation is assumed for intervening times.

A.4 SPECIAL STRUCTURAL ARRANGEMENTS

A.4.1 FOLDED PLATE ANALYSIS

A structure with five plates as shown in Figure A-10(a) can be analyzed approximately by assuming that there are no in-plane (membrane) deformations. On this basis, the structure may be folded out into a single plane, as shown in Figure A-10(b). On the intersection lines of the plates, hinge supports are assumed to prevent transverse motion; only rotation about the lines of intersection of the plates is permitted, and the rotation angles are matched along adjacent edges.

To solve this problem, two types of nodal point numbering systems are needed:

System (a): Numbering according to Figure A-10(c), NNPKS nodal points

System (b): Numbering according to Figure A-10(d), NUMNP nodal points

System (a) controls the number of equations and band width whereas System (b) defines the geometry of the system in accordance with specified nodal coordinates. Nodal points around each element and boundary conditions must be specified for both systems, whereas loads are specified for System (b) only. Note that for an ordinary plate NUMNP = NNPKS.

In the folded plate analysis, contour plots of transverse relative displacements, velocities, and accelerations are not available; however, other contour plots can be obtained. Also, input support motions cannot be specified for this type of structure; i.e., only external transverse forces or pressures can be applied.

A.4.2 INTERNAL COLUMNS AND EQUIPMENT WEIGHTS

Internal column supports, as well as concentrated masses, can be located at arbitrary nodal points of flat plate systems or folded plate structures. The columns are defined by input of the column axial and rotational stiffnesses about two axes. The weight of equipment mounted on the slab can be superimposed onto the slab mass at any node point. The stiffness and mass matrices of the slab grid representation are modified accordingly In the code.

A.5 MESH NUMBERING AND CAPACITY RESTRICTIONS

The nodal numbering should run in the direction with smallest number of elements in order to reduce the bandwidth of the assembled stiffness (see Figure A-11). The element numbering should follow approximately the nodal point numbering, especially for fine meshes; otherwise, an error exit may occur (this restriction is related to the way in which the complete stiffness is assembled).

If contour graphs are to be plotted, the x-axis should be selected along the longest dimension of the plate (to improve graph printout).

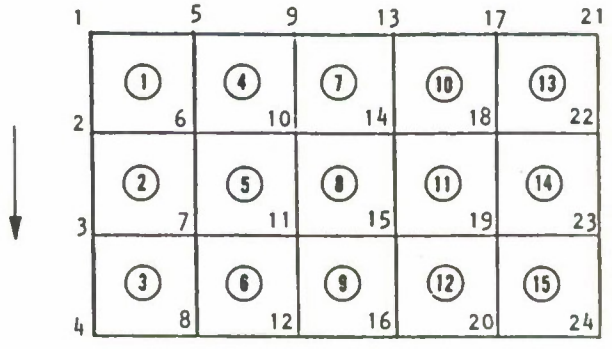

FIGURE A-11. MESH EXAMPLE

A.6 OUTPUT DESCRIPTION

The complete echo check of the input data, including generated properties if the generation option is used, is printed out by the program.

The following items will be printed out for every specified output time step:

a. Relative displacements, relative velocities, and relative accelerations at each node point. For points with skew B.C.'s ($\mu \neq 0$), the printed rotations are about the skew axes x' and y' (defined in Figure A-1(d)).

b. Nodal forces including reactions (optional). The same observation made for the nodal rotations is valid for the nodal moments.

c. Element internal forces including

   1. Bending moments M_{xx}, M_{yy}, and M_{xy}

   2. Principal moments M_1, M_2 ($M_1 \geq M_2$ in algebraic value), maximum twist moment and angle (M_1, χ). After yielding at certain points, the "principal moments" at these points in the element internal forces printout are the moments in the yield axes, whereas those in the nodal forces printout are the principal moments.

   3. Transverse shear resultants Q_x and Q_y. If transverse shear deformations are not included, zero values are printed.

The above values are given at the following points (see Figures A-2 and A-3).

- Four corners and the internal point of a quadrilateral $\begin{pmatrix}1,2,3,4,5\\I,J,K,L,C\end{pmatrix}$;
- Three corners of a single triangle $\begin{pmatrix}1,2,3\\I,J,K\end{pmatrix}$.

If the element is a beam, only the following values are printed at its two end nodes I, J:

M_{xx} = beam bending moment;

M_{xy} = torsional moment (constant along the beam element);

Q_x = transverse shear resultant.

Nodal moments and shears are averaged over plate element only. These values are significant only if there is no sharp variation of thickness or material properties between adjacent elements; otherwise, the element values are more representative for each region.

Contour line graphs of transverse displacements, velocities, accelerations, average nodal moments and shears are printed at specified intervals. Adequate graph spacings are computed automatically by the program.

Graph spacings for peak response contour line graphs of transverse displacements, velocities, accelerations, average nodal moments M_{xx} and M_{yy} are also calculated by the program.

Time history plots over the complete time interval of the transverse displacements, velocities, accelerations, M_{xx}, M_{yy}, and M_{xy} at specified nodes (maximum 10) appear at the end of the program printout. The program will pick up the maximum absolute value and print other values proportionately.

If the time step Δt is long compared to the shortest estimated natural period T considered, the step-by-step integration assuming linear acceleration may become unstable and give meaningless results. On the basis of previous experience, a time step no longer than $\Delta t < T/4$ is suggested to ensure stability of solution. In addition, it should be noted that rapidly varying loads may require even shorter time intervals for adequate representation in the analytical procedure.

A.7 BRIEF DESCRIPTION OF SLAB CODE

SLAB Code is a large digital computer program capable of solving problems involving dynamic elastic response of arbitrarily shaped thin or moderately thick plates of uniform or variable thickness. The plate may have concentrated masses, beams, columns, and cut-outs or holes at arbitrary locations along the surface of the plate. Either isotropic or orthotropic material properties can be specified, and these properties may vary arbitrarily for different regions of the plate.

Input loadings for the SLAB Code may consist of ground motion accelerations and/or force time histories. The ground motion time histories may consist of global transverse accelerations and/or angular accelerations about both the x and y axes. Input force time histories may consist of both concentrated and distributed loads normal to the plate surface. The concentrated loads at any node point may include both concentrated forces or concentrated moments about the x and y axes of the plate. The distributed loads can incorporate arbitrary intensity and time variations for various regions of the plate surface.

The boundaries of the plate may be constrained in the transverse direction or may have rotational constraint about either the x or the y axes. Boundary conditions along skewed boundaries (i.e., boundaries not parallel or perpendicular to the global x and y axes) may also be specified. Initial displacements and/or rotations are allowed. Global deformations and motions consist of rigid body translations and rotations.

Three different types of elements are available, namely, quadrilateral elements, triangular elements, and beam elements, allowing the user flexibility in designing finite element meshes. The quadrilateral and triangular elements are completely compatible, and thereby provide a significant improvement over other finite element plate codes presently available.

The code uses a modal superposition technique in which a specified number of eigenvalues and eigenvectors are calculated. An inverse iteration technique is used to solve for the eigenvalues and eigenvectors. This technique calculates the smallest eigenvalue first. This eigenvalue is then removed from the solution and the succeeding eigenvalues are calculated one by one, each time eliminating the calculated eigenvalue from the solution. The decoupled modal equations of motion are solved using a step-by-step integration procedure assuming a linear variation of acceleration between time steps. The resulting modal responses are then superimposed to obtain the total response of the system.

Additional output, such as absolute motions, time history plots, and shock spectra can be obtained using the postprocessor, SLBOUT. The post-processor is designed to produce punched output and/or digital, incremental (CalComp) plots of response and stress time histories of specified points. The SLBOUT Code also has the option of plotting shock spectra.

APPENDIX B

INCLUSION OF DISCRETE DAMPERS IN INSLAB CODE

The resistance to the magazine headwall offered by the compacted soil medium is represented by viscous damping elements in the finite element model of the headwall for INSLAB Code. Since the INSLAB Code did not contain this capability, special revisions to the program were undertaken during the course of the present investigation. This appendix documents the procedure to include discrete viscous damping elements in the INSLAB Code.

The equations of motion at time t can be written in incremental form using the usual notation of Appendix A as

$$[M]\{\Delta\ddot{X}_t\} + [C]\{\Delta\dot{X}_t\} + [K]\{\Delta X_t\} = \{\Delta P_t\} \qquad \text{(B-1)}$$

where

$$\begin{aligned} \{\Delta\ddot{X}_t\} &= \{\ddot{X}_t\} - \{\ddot{X}_{t-\Delta t}\} \\ \{\Delta\dot{X}_t\} &= \{\dot{X}_t\} - \{\dot{X}_{t-\Delta t}\} \\ \{\Delta X_t\} &= \{X_t\} - \{X_{t-\Delta t}\} \\ \text{and} \quad \{\Delta P_t\} &= \{P_t\} - \{P_{t-\Delta t}\} \end{aligned} \qquad \text{(B-2)}$$

The damping matrix $[C]$ is given by

$$[C] = \alpha[M] + \beta[K] + [D] \qquad \text{(B-3)}$$

where $[D]$ is a diagonal matrix containing damping coefficients associated with the discrete damping elements. For constant acceleration assumption it can be shown that the equations of motion (Equation B-1) can be written as

$$[K_e]\{U_e\} = \{P_e\} \qquad \text{(B-4)}$$

where

$$[K_e] = [K] + \frac{C1}{C2}[M] + \frac{C5}{C2}[D]$$

$$\{U_e\} = C2\{\Delta X_t\} - \beta\{B_t\}$$

$$\{P_e\} = \{\Delta P_t\} + [M]\left(\{A_t\} + \left(\alpha - \frac{C1}{C2}\beta\right)\{B_t\}\right) + \left(1 - \frac{C5}{C2}\beta\right)[D]\{B_t\} \quad \text{(B-5)}$$

$$\{A_t\} = C4\{\dot{X}_{t-\Delta t}\} + 2\{\ddot{X}_{t-\Delta t}\}$$

$$\{B_t\} = 2\{\dot{X}_{t-\Delta t}\}$$

and

$$C1 = \frac{4}{\Delta T^2} + \frac{2\alpha}{\Delta T}$$

$$C2 = 1 + \frac{2\beta}{\Delta T} \quad \text{(B-6)}$$

$$C4 = \frac{4}{\Delta T}$$

$$C5 = \frac{2}{\Delta T}$$

Thus, Equation B-4 replaces Equation A-4. A comparison of Equations A-5 and B-5 shows that the addition of the damping elements modifies expressions for $[K_e]$ and $\{P_e\}$ only. Following the procedure outlined in Appendix A, the displacements, velocities, and accelerations at time t can be calculated.

APPENDIX C

STATIC CONDENSATION

The element stiffness matrix of a plate finite element (Figure C-1) relates the nodal displacements to the nodal forces as follows:

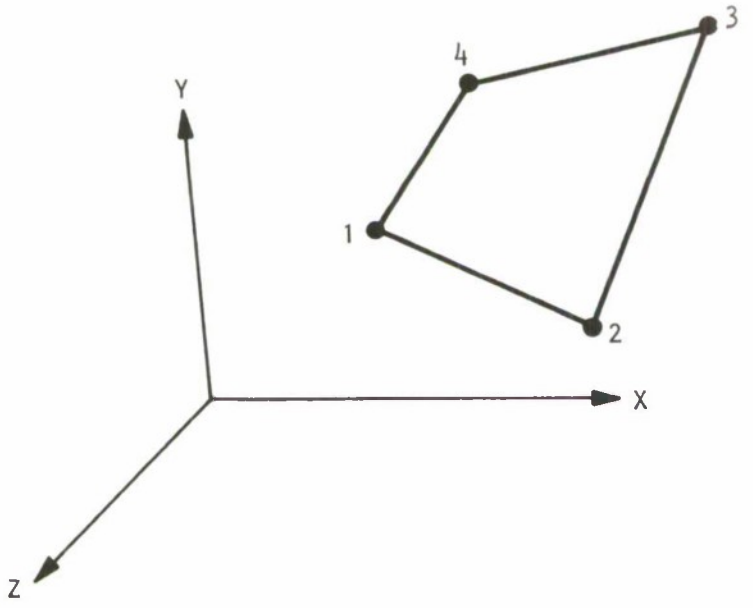

FIGURE C-1. QUADRILATERAL PLATE ELEMENT

$$\begin{bmatrix} K_{11} & K_{12} & \cdots & K_{1n} \\ K_{21} & K_{22} & \cdots & K_{2n} \\ \vdots & & & \vdots \\ K_{m1} & K_{m2} & \cdots & K_{mn} \\ \vdots & & & \vdots \\ K_{n1} & K_{n2} & \cdots & K_{nn} \end{bmatrix} \begin{Bmatrix} u_1 \\ u_2 \\ \vdots \\ u_m \\ \vdots \\ u_n \end{Bmatrix} = \begin{Bmatrix} P_1 \\ P_2 \\ \vdots \\ P_m \\ \vdots \\ P_n \end{Bmatrix} \qquad (C\text{-}1)$$

or $[K] \{u\} = \{p\}$

$[K]$ = Element stiffness matrix

$\{u\}, \{p\}$ = Generalized nodal displacement and force vectors

For a quadrilateral, the size of the stiffness matrix is 12 x 12, with three degrees of freedom (DOF) per node, one transverse displacement and two rotations. Thus, referring to Figure C-1, u_1, u_4, u_7, and u_{10} represent nodal displacements, while the remaining u_i's represent rotations. Similarly, p_1, p_4, p_7, and p_{10} represent nodal shear forces, while the remaining p_i's represent moments. If a hinge exists at a node, then the moments at that node are always zero. Assuming $p_m = 0$ the equation (C-1) is rewritten as

$$\sum_{j=1}^{n} K_{ij} u_j = p_i, \quad i \neq m \tag{C-2}$$

$$\sum_{j=1}^{n} K_{ij} u_j = p_m = 0 \tag{C-3}$$

Equation C-3 can be rewritten as

$$\sum_{j \neq m} K_{mj} u_j + K_{mm} u_m = 0$$

$$\text{or} \quad u_m = - \frac{\sum_{j \neq m} K_{mj} u_j}{K_{mm}} \tag{C-4}$$

The substitution of Equation C-4 into Equation C-2 gives

$$\sum_{j \neq m} K_{ij} u_j - K_{im} \frac{\sum_{j \neq m} K_{mj} u_j}{K_{mm}} = p_i, \quad i \neq m \tag{C-5}$$

Equation (C-5) can be rewritten as

$$\left[K'\right] \quad \{u\} = \{p\} \tag{C-6}$$

$$K'_{ij} = K_{ij} - \frac{K_{im} \; K_{mj}}{K_{mm}} \tag{C-7}$$

where $\left[K'\right]$ is the modified or condensed stiffness matrix that incorporates the condition that $p_m = 0$. This procedure can be repeated for each DOF with $p_i = 0$ to obtain the final modified or condensed element stiffness matrix. The resulting stiffness matrix then correctly exhibits the hinged conditions.

BLANK

APPENDIX D

REFERENCES

1. Weals, F. H., *ESKIMO I Magazine Separation Test*, NWC TP 5430, China Lake, California: Naval Weapons Center, April 1973.

2. Adini, A., and Clough, R. W., *Analysis of Plate Bending by the Finite Element Method*, NSF Report, Grant G-7337, 1960.

3. Melosh, R. J., "Basis for the Deviation of Matrices for the Direct Stiffness Method," *AIAA Journal*, 1 (1963): 1631.

4. Argyris, J., *Continua and Discontinua*, Conference on Matrix Methods in Structural Mechanics, AFIT, Ohio, 1965.

5. Bogner, F. K., et al., *The Generation of Interelement-Compatible Stiffness and Mass Matrices by the Use of Interpolation Formulas*, Conference on Matrix Methods in Structural Mechanics, AFIT, Ohio, 1965.

6. Tocher, J. L., "Analysis of Plate Bending Using Triangular Elements," Ph.D. dissertation, University of California at Berkeley, 1963.

7. Clough, R. W., and Tocher, J. L., *Finite Element Stiffness Matrices for Analysis of Plate Bending*, Conference on Matrix Methods in Structural Mechanics, AFIT, Ohio, 1965.

8. De Veubeke, F. B., *Bending and Stretching of Plates--Special Models for Upper and Lower Bounds*, Conference on Matrix Methods in Structural Mechanics, AFIT, Ohio, 1965.

9. Clough, R. W., and Felippa, C. A., *A Refined Quadrilateral Element for Analysis of Plate Bending*, Conference on Matrix Methods in Structural Mechanics. Ohio: Wright-Patterson AFB, 1968.

10. Wilson, E. L., et al., *Incompatible Displacement Models*, ONR Symposium on Matrix in Structural Mechanics, University of Illinois, Urbana, Illinois.

11. *Proof and Experimental Establishment*, Shoeburyness Trial Report No. SXR/662/013 Trial: ESTC 3/71 Firings 1 and 2.

12. *Proof and Experimental Establishment*, Shoeburyness Trial Report No. SXR/662/013 Trial: ESTC 3/71 Firing 3.

13. *Proof and Experimental Establishment*, Shoeburyness Trial Report No. SXR/662/013 Trial: ESTC 3/71 Firing 4.

14. *Proof and Experimental Establishment*, Shoeburyness Trial Report No. SXR/662/013 Trial: ESTC 3/71 Firing 5.

15. Brode, H. L., *A Review of Nuclear Explosion Phenomena Pertinent to Protective Construction*, R 424 PR. Los Angeles: Rand Corporation, May 1964.

16. Kingery, C. N., *Air Blast Parameters Versus Distance for Hemispherical TNT Surface Bursts*, BRL Report No. R1344, September 1966.

17. Leissa, A. W., *Vibration of Plates*, NASA SP-160, Washington, D. C., 1969.

18. *Design of Structures to Resist the Effects of Atomic Weapons*, Manual EM1110-345-414. U.S. Army, Corps of Engineers, March 1957.

19. Urquhart, L. C., et al., *Design of Concrete Structures*, New York: McGraw-Hill, 1958.

20. Timoshenko, S., and Woinowsky-Krieger, S., *Theory of Plates and Shells*, 2nd Edition. New York: McGraw-Hill, 1959.

21. *Igloo Door Test--Modulus of Soil Reaction*, Washington, D. C.: Code 7036, Naval Weapons Center (unpublished memorandum).

UNCLASSIFIED
Security Classification

DOCUMENT CONTROL DATA - R & D

(Security classification of title, body of abstract and indexing annotation must be entered when the overall report is classified)

1. ORIGINATING ACTIVITY *(Corporate author)*
AGBABIAN ASSOCIATES
250 North Nash Street
El Segundo, California 90245

2a. REPORT SECURITY CLASSIFICATION
UNCLASSIFIED

2b. GROUP

3. REPORT TITLE
Magazine Headwall Response to Explosive Blast

4. DESCRIPTIVE NOTES *(Type of report and inclusive dates)*
SCIENTIFIC. FINAL REPORT. June 1973 to January 1974. Accepted with corrections 18 July 1974.

5. AUTHOR(S) *(First name, middle initial, last name)*
Hsueh-Sheng Ts'ao
Damoder P. Reddy
Ross W. Dowdy

6. REPORT DATE	7a. TOTAL NO. OF PAGES	7b. NO. OF REFS
January 1974	168	21

8a. CONTRACT OR GRANT NO.	9a. ORIGINATOR'S REPORT NUMBER(S)
DAAB09-73-C-0019	R-7336-3284
b. PROJECT NO. RDT&E #4A765702M857	
c.	9b. OTHER REPORT NO(S) *(Any other numbers that may be assigned this report)*
d.	

10. DISTRIBUTION STATEMENT
No limitation

11. SUPPLEMENTARY NOTES	12. SPONSORING MILITARY ACTIVITY
	DDESB Washington, D. C. 20314

13. ABSTRACT

This report presents results of a study for predicting analytically the dynamic response of magazine headwalls subjected to blast pressure loadings resulting from the explosion of the contents of an adjacent magazine. Primary study objective is to simulate headwalls in the Eskimo I test by a finite element model and to compare results with test data. A nonlinear finite element computer program, INSLAB Code, is used to compute dynamic responses of the headwall. Headwall material behavior is described by a bilinear moment-curvature relationship, and supporting soil is simulated by a series of dampers. Calculations are performed for three different blast loadings, each selected on the basis of measured data and theoretical derivations. Results are compared with available measurements. Predicted responses of south igloo are found in good agreement with measured data. Some disagreements between test data and computed results are observed, especially in north and east igloos. Recommendations for improving analytical procedure for better correlation of results include (1) better evaluation of material properties; (2) refinement of finite element model; (3) alternate methods for modeling soil; and (4) sensitivity studies of response calculations to variations in input parameters. In future tests, pretest prediction analyses should be considered.

14 KEY WORDS	LINK A		LINK B		LINK C	
	ROLE	WT	ROLE	WT	ROLE	WT
Magazine Headwall Response						
Dynamic Finite Element						
Nonlinear Slabs						
Explosive Blast						
Nonlinear Finite Element						
Eskimo Test						
Igloo Storage Magazine						

DISTRIBUTION LIST

	Number of Copies
Chairman Department of Defense Explosives Safety Board Rm GB 270, Forrestal Building Washington, D. C. 20314	5
Defense Documentation Center Attn: DDC-TC Cameron Station Alexandria, VA 22314	12
Director of Defense Research and Engineering Department of Defense Washington, D. C. 20301	1
Chief of Research and Development Department of the Army Washington, D. C. 20310	1
Commander Army Materiel Command Attn: COL J. Aaron, AMCSABC 5001 Eisenhower Avenue Alexandria, Virginia 22333	1
Commander Army Materiel Command Attn: W. G. Queen, AMCSF 5001 Eisenhower Avenue Alexandria, Virginia 22333	1
Office of the Inspector General Department of the Army Attn: DAIG-SD (Mr. Abernethy) Washington, D. C. 20310	1
Chief of Engineers Department of the Army Attn: DAEN-MCZ-S Washington, D. C. 20314	1
Chief of Engineers Department of the Army Attn: Mr. G. F. Wigger, DAEN-MCE-D Washington, D. C. 20314	2

	Number of Copies
Commanding Officer Picatinny Arsenal Attn: SARPA-MTD Dover, New Jersey 07801	1
Commanding General U.S. Army Armament Command Rock Island Arsenal Rock Island, Illinois 61201	1
Director Ballistic Research Laboratories Attn: AMXBR-TB, Mr. C. N. Kingery Aberdeen Proving Ground, Maryland 21005	1
Chief of Naval Materiel Department of the Navy Attn: MAT0441B Washington, D. C. 20360	1
Commander Naval Sea Systems Command Office of the Inspector General Attn: SEA-00N2, CAPT M. B. Lechleiter Washington, D. C. 20360	1
Commander Naval Sea Systems Command Attn: SEA-09B4, Mr. H. M. Roylance Washington, D. C. 20360	1
Chief of Naval Operations Department of the Navy Attn: OP-411F, Mr. J. W. Connelly Washington, D. C. 20350	1
Commander Naval Weapons Center Attn: Code 372 China Lake, California 93555	1
Commander Naval Ordnance Laboratory, White Oak Attn: Code 241 Silver Spring, Maryland 20910	1
Commanding Officer Naval Ammunition Depot Attn: NAPEC Crane, Indiana 47522	1

	Number of Copies
Commander Naval Weapons Laboratory Attn: Code T Dahlgren, Virginia 22448	1
Director Civil Engineering Laboratory Attn: Mr. W. A. Keenan Naval Construction Battalion Center Port Hueneme, California 93043	1
Director Defense Nuclear Agency Attn: Mr. J. R. Kelso, SPTD Washington, D. C. 20305	1
Director Defense Nuclear Agency Attn: Mr. E. L. Eagles, LGLS Washington, D. C. 20305	1
Director of Aerospace Safety Headquarters, U.S. Air Force Attn: AFISC/SEV, COL J. P. Huffman Norton AFB, California 92409	1
Headquarters, U.S. Air Force Attn: IGI (LTC J. C. Allison) The Pentagon Washington, D. C. 20330	1
Air Force Systems Command Attn: SCIZG (Mr. Howell) Andrews Air Force Base Washington, D. C. 20331	1
Director, Air Force Weapons Laboratory Attn: WLDC (Mr. F. Peterson) Kirtland Air Force Base, N. M. 87117	1
Commander Air Force Armament Laboratory Attn: ATBT Eglin Air Force Base, Fla. 32542	1

	Number of Copies
U.S. Atomic Energy Commission Division of Operational Safety Attn: Mr. J. P. H. Kelley Washington, D. C. 20545	1
Albuquerque Operations Office Atomic Energy Commission Attn: ODI P. O. Box 5400 Albuquerque, N. M. 87115	1
Mason & Hanger-Silas Mason Co., Inc. Pantex Plant - AEC Attn: Director of Development P. O. Box 647 Amarillo, Texas 79105	1
Dr. Robert W. Van Dolah Research Director - Pittsburgh Mining & Safety Research Center Bureau of Mines, Department of Interior 4800 Forbes Avenue Pittsburgh, Pennsylvania 15213	1
Institute of Makers of Explosives Attn: Mr. Harry Hampton Graybar Building, Rm 2449 420 Lexington Avenue New York, N. Y. 10017	1
Assistant Secretary of Defense (I&L) Attn: ID (Mr. H. Metcalf) Washington, D. C. 20301	1
Mr. M. E. McDowall National Defence Headquarters 101 Colonel By Drive Ottawa, Ontario K1A 0K2 CANADA	1
Mr. R. R. Watson Safety 1 (PE) MOD Station Square House St. Mary Cray Orpington, Kent BR5 3RE ENGLAND	1

	Number of Copies
M. J. J. Roure Inspection Technique des Poudres et Explosifs 12 Quai Henri-IV 75004 Paris FRANCE	1
Oberstleutnant G. Werner Materialamt des Bundeswehr 5205 St. Augustin 1 Alte Heerstrasse 81 GERMANY	1
Lt. Col. G. Kyrkjebø Krutt-og Sprengstoff Laboratoriet med Arsenalet på Raufoss 2831 Raufoss NORWAY	1
Black & Veatch Consulting Engineers Attn: Mr. H. L. Callahan 1500 Meadow Lake Parkway Kansas City, Missouri 64114	2
IIT Research Institute Engineering Mechanics Division Attn: Mr. A. Longinow 10 West 35 Street Chicago, Illinois 60616	1
General American Research Division Attn: Dr. L. E. Fugelso 7449 N. Natchez Avenue Niles, Illinois 60648	1